UNIVERSITY OF HAMBURG

DEPARTMENT OF PHYSICS

3D nano-tomography using coherent X-rays

Dissertation

zur Erlangung des Doktorgrades

an der Fakultät für Mathematik, Informatik und Naturwissenschaften
Fachbereich Physik
der Universität Hamburg

vorgelegt von
MAIK KAHNT
(geb. 27.07.1988 in Lauchhammer)

Hamburg
2019

The work described in this thesis is done at the Photon Science division of
Deutsches Elektronen-Synchrotron, a Research Centre of the Helmholtz Association.

Gutachter/in der Dissertation:	Prof. Dr. Christian G. Schroer Dr. habil. Michael Hanke
Zusammensetzung der Prüfungskommission:	Prof. Dr. Daniela Pfannkuche Prof. Dr. Christian G. Schroer Dr. habil. Thomas F. Keller Prof. Dr. Markus Drescher Prof. Dr. Edgar Weckert
Vorsitzende/r der Prüfungskommission:	Prof. Dr. Daniela Pfannkuche
Datum der Disputation:	31.07.2020
Vorsitzende/r des Fach-Promotionsausschusses PHYSIK:	Prof. Dr. Michael Potthoff
Leiter/in des Fachbereichs PHYSIK:	Prof. Dr. Wolfgang Hansen
Dekan/in der Fakultät MIN:	Prof. Dr. Heinrich Graener

Abstract

X-rays allow to non-destructively investigate biological, chemical or physical processes at the nano-scale. Their high penetration depth in matter allows to investigate samples even inside sample environments, which would be difficult with complementary methods such as transmission electron microscopy (TEM). The microscopy technique ptychography has been established in X-ray imaging in recent years. Utilizing the short wavelengths of X-rays, resolutions of about $10\,\mathrm{nm}$ and below have been achieved in the reconstructed projection images.

However, projections provide no information about the spatial distribution of features along the beam axis. Knowing the structure of materials and objects in three spatial dimensions is key to understanding their properties and function. Hence, two-dimensional ptychography has been extended to three spatial dimensions based on tomographic methods known from radiographs and computed tomography (CT) resulting in a method called ptychographic X-ray computed tomography (PXCT). Using PXCT quantitative three-dimensional maps of the complex index of refraction of the sample can be reconstructed, which yield quantitative information on the local electron density. Such PXCT measurements are very time intensive to perform, very computing intensive to reconstruct and are based on several limiting approximations.

In this work, a detailed description of PXCT and its limitations is given. From that starting point, a coupled ptychographic tomography (CPT) algorithm, improving on the PXCT algorithm in terms of alignment and sampling requirements, is presented and tested on experimental data. Moreover, a resonant PXCT experiment is performed at the Ga-K absorption edge, allowing for additional elemental and chemical information inside the reconstructed volume. Afterwards, the shared limit of both the PXCT algorithm and the CPT algorithm, the thin-sample approximation, is addressed by presenting a multi-slice approach utilizing the propagation of the X-ray beam in the sample. In total three different experiments, performed at the hard X-ray nanoprobe endstation at beamline P06 at the PETRA III synchrotron radiation source, are presented in this work.

Kurzfassung

Röntgenstrahlen erlauben die zerstörungsfreie Untersuchung biologischer, chemischer oder physikalischer Prozesse im Nanobereich. Ihre hohe Eindringtiefe in Materie ermöglicht die Untersuchung von Proben auch innerhalb von Probenumgebungen, was mit komplementären Techniken wie Transmissionselektronenmikroskopie schwierig wäre. Die Mikroskopiemethode Ptychographie hat sich in den letzten Jahren in der Röntgenbildgebung etabliert. Durch das Ausnutzen der kurzen Wellenlängen von Röntgenstrahlen wurden Auflösungen von etwa $10\,\mathrm{nm}$ und besser in den rekonstruierten Projektionsbildern erreicht.

Projektionen geben jedoch keine Auskunft über die räumliche Verteilung von Merkmalen entlang der Strahlachse. Die Struktur von Materialien und Proben in den drei Raumimensionen zu kennen, ist Schlüssel zum Verständnis ihrer Eigenschaften und ihrer Funktion. Daher wurde die zweidimensionale Ptychographie auf der Grundlage von tomographischen Methoden, die aus Röntgenbildern und Computertomographie bekannt sind, auf drei Raumdimensionen erweitert, was zur ptychographische Röntgen-Computertomographie (PXCT) führte. Mit PXCT können quantitative dreidimensionale Abbildungen des komplexen Brechungsindex der Probe rekonstruiert werden, die quantitative Informationen zur lokalen Elektronendichte enthalten. Solche PXCT-Messungen sind sehr zeitintensiv in der Durchführung, sehr rechenintensiv in der Rekonstruktion und basieren auf mehreren einschränkenden Näherungen.

In dieser Arbeit beschreibe ich die PXCT und seine Eigenschaften detailliert. Davon ausgehend wird ein gekoppelter Ptychographie- und Tomographie- Algorithmus (CPT) hergeleitet und an experimentellen Daten getestet. Dieser (CPT) Algorithmus verbessert die Ausrichtung der einzelnen Projektionen und verringert die Anforderungen an die Abtastdichte im Vergleich zum PXCT Algorithmus. Darüber hinaus wird ein resonantes PXCT-Experiment an der Gallium K-Absorptionskante durchgeführt, welches zusätzliche elementare und chemische Information innerhalb des rekonstruierten Volumens ermöglicht. Sowohl der PXCT- als auch der CPT- Algorithmus sind auf optisch dünne Proben beschränkt. Im letzten Abschnitt der Arbeit wird dieses Problem gelößt, indem die probe durch mehere dünne Schichten modelliert wird und die Ausbreitung des Röntgenstrahls in der Probe berücksichtigt wird. Insgesamt werden in dieser Arbeit drei verschiedene Experimente vorgestellt, die an dem Strahlrohr P06 an der Synchrotronstrahlungsquelle PETRA III durchgeführt wurden.

Contents

Abbreviations

3PIE	three-dimensional ptychographical iterative engine . . . 106
ART	algebraic reconstruction technique . . . 36
CPT	coupled ptychographic tomography . . . 105
CL	cathodoluminescence . . . 73
CT	computed tomography . . . 33
DCM	double crystal monochromator . . . 94
DESY	Deutsches Elektronen-Synchrotron . . . 57
DOF	depth of focus . . . 97
ePIE	extended ptychographical iterative engine . . . 106
EXAFS	extended X-ray absorption fine structure . . . 85
FBP	filtered back-projection . . . 35
FIB	focused ion-beam . . . 73
FOV	field of view . . . 95
FRC	Fourier ring correlation . . . 98
FSC	Fourier shell correlation . . . 103
FWHM	full width at half maximum . . . 76
FZP	Fresnel zone plate . . . 94
GPU	graphics processing unit . . . 96
GPUs	graphics processing units . . . 57
MSPs	mesoporous, spherical silica particles . . . 54
NFL	nano focusing lens . . . 78
OSA	order sorting apperture
PtyNAMi	Ptychographic nano-analytical microscope at PETRA III . . . 75
PXCT	ptychographic X-ray computed tomography . . . 105
QB	quantum barrier . . . 74
QW	quantum well . . . 74
SART	simultaneous algebraic reconstruction technique . . . 106
SIRT	simultaneous iterative reconstruction technique . . . 45
SEM	scanning electron microscopy . . . 94
SNR	signal-to-noise ratio . . . 106
SSNR	spectral signal to noise ratio . . . 70
STXM	scanning transmission X-ray microscopy . . . 105
TEM	transmission electron microscopy . . . 73
XANES	X-ray absorption near edge structure . . . 18
XRF	X-ray fluorescence . . . 105
XBIC	X-ray beam induced current . . . 107
XBIV	X-ray beam induced voltage . . . 107

Chapter 1

Introduction

Curiosity is one of the main the driving forces of progress and innovation. Mankind always wanted, and still wants, to know how the world around us works and why things are as they are. The primary tool for most of us to first examine something in detail is vision. Looking at something and perceiving it with our eyes allows for the first categorization and classification inside our mind. Because humans are so visual in their approach to study and explore, we build tools, devices and machines such as glasses, microscopes and telescopes to help us with seeing even more.

This thesis is all about microscopy: making small things visible. Because we perceive the world around us in three spatial dimensions, this thesis also focuses on three dimensional imaging of the studied specimen. Resolving smallest structures in three dimensions is of great importance for understanding the functionality of materials, because micro structures and nano structures influence the properties of matter. Many examples can be found in nature itself. The micro structuring and nano structuring of almost the same hydrocarbons can create the brightest white [1–3], the darkest black [4,5], vibrant colors [6,7] and even transparent and anti-reflective materials [8]. Knowing about these structures allowed to recreate these effects on purpose in other materials [9–11]. Not only photonic properties of materials change with their structure. Physical properties such as hardness [12] or functional properties like heat-resistance [13] can be changed by structuring of materials. Chemical properties like the catalytic activity of nano-materials also differ from their macroscopic bulk materials as the ratio of surface atoms to bulk atoms changes. Even structuring the catalytic inert support material of a catalyst systems can change the overall catalytic activity [14], as the permeability for the reacting molecules might change. The charge capacity and lifetime of batteries and the efficiency of solar cells depend on the structuring of their electrodes [15–18].

In this thesis, a catalyst zeolite particle, an opto-electronic InN/GaN micro-rod and the formation of copper (I) oxide nano cubes are investigated using X-rays. The high penetration depth of X-rays allows to image samples too thick for electron microscopy and is essential for three-dimensional imaging. The small wavelengths between $10\,\mathrm{nm}$ and $100\,\mathrm{pm}$ theoretically allow for highest resolutions according to the Abbe diffraction limit [19]. The method used in

this thesis for imaging samples using X-rays is called ptychography [20]. It is a coherent scanning microscopy technique, which has several unique advantages compared to other microscopy techniques. Because it is a scanning technique, the field of view is only limited by the range of the scanning stages. Ptychography allows to reconstruct and separate probe and sample, making the reconstruction independent from aberrations of the probing beam. Moreover, ptychography allows for the quantitative evaluation of the reconstructed images, as the phase shift obtained by the probing beam while passing through the sample is proportional to the electron density inside the sample. The detector acts as imaging lens, limiting the achievable resolution to the highest scattering vector recorded with sufficiently high signal-to-noise ratio (SNR) on the detector. Hence, everything needed for achieving higher resolutions is, in theory, a larger detector, longer exposure times and sufficient stability in the experimental setup [21, 22].

Ptychographic X-ray computed tomography, as extension from two-dimensional ptychography, has been implemented at multiple synchrotron radiation sources to investigate the structures of mircometer sized samples [23–29], achieving resolutions down to $14\,\mathrm{nm}$. Key to reconstructing the three-dimensional structure of the sample is the recording of multiple unique two-dimensional angular views of the sample, which are all reconstructed separately before being aligned to each other and finally being reconstructed using any tomographic algorithm. The main drawbacks of ptychographic tomography are the long duration of the measurement, the requirement for each projection to reconstruct on its own, the vast computational effort and the limitations to X-ray optically thin samples.

The goal of this thesis is to alleviate some of these drawbacks. The original contribution of this thesis is addressing three topics building on top of each other and each one presented using an experiment performed at the P06 nano-probe endstation of beamline P06 at the PETRA III synchrotron light source:

First, a coupled ptychographic tomography algorithm will be deduced. The algorithm is then applied to recorded experimental data of a hierarchical structured zeolite catalyst particle in chapter 6. The coupling of previously separated steps of two-dimensional ptychography and tomography increases the redundancy in the data set and allows for sharing of information between projections allowing better reconstructions. Moreover the sharing of information should reduce the sampling requirements in each projection, theoretically allowing for faster scanning and therefore reduced measurement durations. Those aspects will be investigated and compared to the state of the art sequential algorithm. This is the first time such a coupled ptychographic tomography algorithm is used on experimental data and not just simulations. Hence, deviations from the ptychographic model due to experimental limitations and their influence on the reconstructed volume will be discussed in detail.

Second, ptychographic tomography will be extended to a resonant and multi-modal measurements in chapter 7. As ptychography requires lateral scanning of the sample with a finite beam profile, other contrasts relying on the same scanning method can be recorded simultaneously.

Here, X-ray fluorescence of the layered InN/GaN micro rod sample excited by the probing X-ray beam will be measured, allowing to distinguish distributions of different elements inside the sample. The additional resonant measurement on and above the Ga-K edge, also allows for elemental Ga contrast using the ptychographic tomography reconstructions. The evaluation of the experiment will focus on generating a single multi-dimensional mutli-contrast volume from these different measurements which can be analyzed in its entirety. The basics for the extension to chemical contrast via the resonant aspect of the measurement and incorporation of other scanning transmission X-ray microscopy (STXM) based contrasts will be discussed.

Third, the limitation of ptychographic tomography to thin samples will be approached by modeling the sample as multiple thin slices in chapter 8. Modeling and reconstructing the sample this way allows for thicker samples to be accurately imaged and also reduces the number of unique angular samples required. A measurement performed on a Kapton foil covered in Cu_2O cubes on both sides will be used to discuss the method, its limitations and how the propagation of the probing beam inside the sample allows to separate robustly which particles are on which side of the sample.

Before those three experiments are presented, each designed to demonstrate one aspect of ptychographic tomography, I will discuss the essential models used throughout this thesis. In chapter 2, the modeling of X-rays, their propagation and interaction with matter will be discussed. The two-dimensional ptychographic model, its limitations and its approximations as well as ptychographic reconstruction algorithms are presented in chapter 3. The essentials of tomography and tomographic reconstruction algorithms are described in chapter 4. Finally, all of the previous considerations are combined in chapter 5, where I describe three-dimensional ptychography methods.

After presenting the experimental results in chapters 6, 7 and 8, the conclusion of the thesis and an outlook of further applications and developments of ptychographic tomography will be given in chapter 9.

Chapter 2

X-rays

Coherent diffractive imaging using X-rays is just one of many specialized fields of modern X-ray methods carried out at current synchrotron light sources and free-electron lasers. To understand the experiments presented in this work and to correctly interpret the measured data, a certain knowledge about underlying theoretical models is necessary. I will focus on only those concepts essential for understanding the original contribution of this work:

- How are X-rays modeled?
- How do they propagate in space?
- What is coherence?
- What happens to X-rays when they pass through matter?
- How are phase shift and absorption connected?

The description are based on common handbooks in the field by Hecht [30], Attwood [31], Als-Nielsen and McMorrow [32], Willmott [33] and Jaeschke et al. [34]. All presented experiments are based on the elastic scattering of coherent X-rays on bound-electrons inside of atoms making up non-periodic structures. Each deviation from this model would open up another chapter of modern X-ray methods and unnecessarily lengths this work. Hence, a description of in-elastic scattering effects is waived. Descriptions of the creation of X-rays at synchrotron light sources or free-electron lasers are omitted as well, as they are presented in details in the mentioned handbooks and do not constitute an original contribution of this work.

2.1 wave function

X-rays are light. Light is electromagnetic radiation. As such it has to fulfill all four of Maxwell's equations [35] coupling the electric and magnetic field. The simplest way to describe the two components ($\mathbf{E}$ and $\mathbf{B}$) is by writing them as a single complex scalar wave field $\Psi\left(\vec{\rho},t\right)$ depending on the position $\vec{\rho}$ and time t. By expressing the time-dependency of $\Psi\left(\vec{\rho},t\right)$ using multiple spectral components $\Psi_\omega\left(\vec{\rho}\right)$:

$$\Psi\left(\vec{\rho},t\right)=\frac{1}{\sqrt{2\pi}}\int_0^\infty \Psi_\omega\left(\vec{\rho}\right)\exp\left(-\mathrm{i}\omega t\right)\,\mathrm{d}\omega, \tag{2.1}$$

the wave field becomes a superposition of monochromatic wave fields $Psi_\omega(\vec{\rho})$ with different angular frequencies ω [36]. These monochromatic wave fields components $Psi_\omega(\vec{\rho})$ are a solution to the Helmholtz equation:

$$\left(\nabla^2 + k^2\right)\Psi_\omega(\vec{\rho}) = 0 \qquad \text{, where } k = \frac{\omega}{c} = \frac{2\pi}{\lambda}. \tag{2.2}$$

Here k is the wave number to the corresponding angular frequency ω, c is the speed of light in vacuum, and λ is the wave length of the radiation. This representation of the monochromatic wave fields $Psi_\omega(\vec{\rho})$ demands, that they only vary slowly with $\left|\vec{\rho}\right|$ compared to the wave length λ. The wave lengths of X-rays range between $0.01\,\mathrm{nm}$ and $10\,\mathrm{nm}$. The experiments presented in this work were all performed with X-rays of $\approx 0.1\,\mathrm{nm}$ wave length. The length scales of X-ray beams and structures inside the X-ray beam were in the tens of nano meters. Hence, the above presented combined description of the electric field $\vec{E}$ and magnetic field $\vec{B}$ as a function of waves is used throughout this work.

2.2 propagation in space

The Huygens-Fresnel principle [37] can be used to describe the propagation of a wave front in free space. It states that every point of a wavefront $\Psi_{\rho_u}(\rho_x, \rho_y)$ at the upstream position $\rho_z = \rho_u$ is itself a source of a spherical wavelet. The sum over all of these spherical wavelets at the downstream position $\rho_z = \rho_d$ constitute the wavefront $\Psi_{\rho_d}(\hat{\rho}_x, \hat{\rho}_x)$.

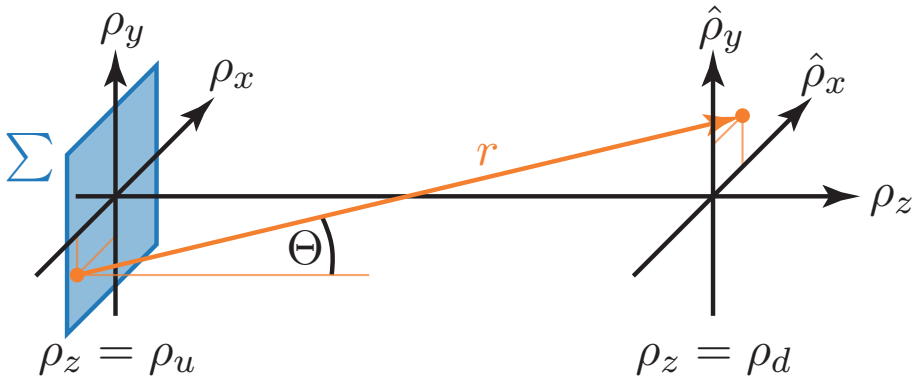

Figure 2.1: Schematic representation of the diffraction geometry (as in [38]): The upstream plane (ρ_x, ρ_y) is located at $\rho_z = \rho_u$, while the downstream plane $(\hat{\rho}_x, \hat{\rho}_y)$ is located at $\rho_z = \rho_d$. Σ is the convex hull of all non-zero components of the upstream wave front $\Psi_{\rho_u}(\rho_x, \rho_y)$.

In the continuous representation the propagation of a wavefront $\Psi_{\rho_d}(\rho_x, \rho_y)$ from $\rho_z = \rho_u$ to $\rho_z = \rho_d$ can be written as (see Fig. 2.1):

$$\Psi_{\rho_d}(\hat{\rho}_x, \hat{\rho}_y) = -\frac{\mathrm{i}k}{4\pi}\int\int_\Sigma \Psi_{\rho_u}(\rho_x, \rho_y)\cdot\frac{\exp(\mathrm{i}kr)}{r}\cos\Theta\,\mathrm{d}\rho_y\,\mathrm{d}\rho_x, \tag{2.3}$$

where:

$$r = \sqrt{(\rho_x - \hat{\rho}_x)^2 + (\rho_y - \hat{\rho}_y)^2 + (\rho_u - \rho_d)^2} \tag{2.4}$$

and $k = 2\pi/\lambda$ is the wave number of the radiation.

When propagating a long distance $\Delta\rho_z = \rho_d - \rho_u$ in comparison to size of the aperture Σ (see Fig.2.1), the angle Θ between the outward normal of the (ρ_x, ρ_y) and the scattering vector $\vec{r}$ becomes very small. Hence, the cosine of Θ becomes approximately 1. This can be used when equation 2.4 is rewritten [39] as :

$$r = \Delta\rho_z\sqrt{1+b}, \quad \text{where} \quad b = \left(\left[\frac{\rho_x - \hat{\rho}_x}{\Delta\rho_z}\right]^2 + \left[\frac{\rho_y - \hat{\rho}_y}{\Delta\rho_z}\right]^2\right) < 1 \tag{2.5}$$

The root can be estimated by its binomial expansion:

$$r = \Delta\rho_z \cdot \left(1 + \frac{1}{2}b - \frac{1}{8}b^2 + \ldots\right) \tag{2.6}$$

As $\Delta\rho_z$ is supposed to be large compared to the aperture Σ, b can be regarded as very small. Only regarding the first two terms, allows to rewrite equation 2.3 as:

$$\Psi_{\rho_d}(\hat{\rho}_x, \hat{\rho}_y) = -\frac{\mathrm{i}k}{4\pi}\frac{\exp(\mathrm{i}k\Delta\rho_z)}{\Delta\rho_z}\int\int_{\Sigma}\Psi_{\rho_u}(\rho_x, \rho_y)\cdot\exp\left(\mathrm{i}k\cdot\Delta\rho_z\cdot\frac{1}{2}\cdot b\right)\mathrm{d}\rho_y\,\mathrm{d}\rho_x, \tag{2.7}$$

As the aperture Σ is supposed to be finite, equation 2.7 can be expressed as a convolution:

$$\Psi_{\rho_d}(\hat{\rho}_x, \hat{\rho}_y) = \int\int\Psi_{\rho_u}(\rho_x, \rho_y)\cdot\mathcal{P}_{\Delta\rho_z}(\hat{\rho}_x - \rho_x, \hat{\rho}_y - \rho_y)\,\mathrm{d}\rho_y\,\mathrm{d}\rho_x \tag{2.8}$$

$$\Psi_{\rho_d}(\hat{\rho}_x, \hat{\rho}_y) = \Psi_{\rho_u}(\hat{\rho}_x, \hat{\rho}_y) * \mathcal{P}_{\Delta\rho_z}(\hat{\rho}_x, \hat{\rho}_y), \tag{2.9}$$

where $\mathcal{P}_{\Delta\rho_z}$ is the convolution kernel for the propagation over the distance $\Delta\rho_z$:

$$\mathcal{P}_{\Delta\rho_z}(\hat{\rho}_x, \hat{\rho}_y) = -\frac{\mathrm{i}k}{4\pi}\frac{\exp(\mathrm{i}k\Delta\rho_z)}{\Delta\rho_z}\exp\left(\frac{\mathrm{i}k}{2\Delta\rho_z}\cdot\left[\hat{\rho}_x^2 + \hat{\rho}_y^2\right]\right) \tag{2.10}$$

Thinking back to the Huygens-Fresnel principle, the expression of the propagation from the downstream position ρ_d to the upstream position ρ_u as a convolution with the impact of every single wavelet on the original wave front $\Psi_{\rho_d}(\rho_x, \rho_y)$ makes sense.

This representation of the propagation is called Fresnel propagation. It is applicable for propagating small distances $\Delta\rho_z < k \cdot D^2$ with $k = 2\pi/\lambda$ being the wave number of the radiation and D being the diameter of the aperture Σ.

When propagating very large distances $\Delta\rho_z \gg k \cdot D^2$ something even more elegant can be done. By factoring out $\exp\left[\mathrm{i}k/(2\Delta\rho_z)\left(\hat{\rho}_x^2 + \hat{\rho}_y^2\right)\right]$ from equation 2.7 one gets:

$$\Psi_{\rho_d}(\hat{\rho}_x, \hat{\rho}_y) = -\frac{\mathrm{i}k}{4\pi}\frac{\exp(\mathrm{i}k\Delta\rho_z)}{\Delta\rho_z}\exp\left(\frac{\mathrm{i}k}{2\Delta\rho_z}\left[\hat{\rho}_x^2 + \hat{\rho}_y^2\right]\right)\cdot$$

$$\int\int_{\Sigma}\left[\Psi_{\rho_u}\left(\rho_x,\rho_y\right)\cdot\exp\left(\frac{\mathrm{i}k}{2\Delta\rho_z}\cdot\left[\rho_x^2+\rho_y^2\right]\right)\right]\underbrace{\exp\left(\frac{\mathrm{i}k}{\Delta\rho_z}\left[\hat{\rho}_x\rho_x+\hat{\rho}_y\rho_y\right]\right)}_{\text{phase term}}\mathrm{d}\rho_y\,\mathrm{d}\rho_x. \tag{2.11}$$

For $\Delta\rho_z \gg k\cdot D^2$ the phase term in the integral becomes a constant for all $(\hat{\rho}_x,\hat{\rho}_y)$ inside the aperture Σ. Hence, equation 2.11 represents a simple Fourier transform of $\Psi_{\rho_d}\left(\rho_x,\rho_y\right)$ with an additional phase factor.

This representation of the free-space propagation is called Fraunhofer propagation and is used for propagating to the far-field. For hard X-rays with a wave length of approximately $1\,\text{Å}$ and a micron sized X-ray beam, $k\cdot D^2$ would become:

$$k\cdot D^2=\frac{2\pi}{1\,\text{Å}}1\,\mu\text{m}^2\approx 63\,\text{mm} \tag{2.12}$$

In this example propagation distances $\Delta\rho_z \gg 63\,\text{mm}$ would justify the representation of the propagation as a simple Fourier transform. For even smaller beams, this criterion becomes even more relaxed.

2.3 Coherence

Coherence is a measure of the correlation between the phases of waves [30, 40]. Coherent scattering experiments, as presented in this work, rely on constant phase relations between waves. Two types of coherence are important for the modeling of the presented experiments:

Longitudinal Coherence

The longitudinal coherence describes the phase relation of waves as they propagate. Assuming two waves with wavelengths λ and $\lambda-\Delta\lambda$ starting with identical phases at the same point propagating in the same direction, those two waves would differ in phase by π after having propagated the distance ξ_l. This distance ξ_l is defined as the longitudial coherence length:

$$\xi_l=\frac{1}{2}\cdot\lambda\cdot\frac{\lambda}{\Delta\lambda} \tag{2.13}$$

If the path length between scattering vectors is larger than ξ_l the interference pattern of the two wave fields is not visible any more.

In an experiment at a synchrotron, the longitudinal coherence length arises from the limited spectral bandwidth of the monochromator. For a Si-111 double crystal monochromator (DCM) the energy resolution is about 10^{-4}. For X-rays with a wavelength of $1\,\text{Å}$, once calculates a longitudinal coherence length ξ_l of:

$$\xi_l=\frac{1}{2}\frac{1\,\text{Å}}{10^{-4}}=500\,\text{nm} \tag{2.14}$$

Transverse Coherence

The transverse coherence results from the lateral extent of the source. Where the diffraction patterns of point, sources always have perfect contrast, the superposition of multiple point sources may destroy the visibility of the interference fringes in diffraction pattern. The transverse coherence length ξ_t can be calculated as:

$$\xi_t = \frac{1}{2}\frac{\lambda L_{SO}}{D_S}, \tag{2.15}$$

where λ is the wavelength of the radiation, L_{SO} is the distance between source and imaged object and D_S is the size of the source. Having an object with a diameter $D_O \geq \xi_t$ would result in the interference fringes in the diffraction pattern being not visible anymore.

At the P06 nano-probe beamline at PETRA III [41], transverse coherence lengths of $87\,\mu\mathrm{m}$ (horizontal) to $567\,\mu\mathrm{m}$ (vertical) are achieved at $L_{SO} = 100\,\mathrm{m}$ and $E_{photon} = 12\,\mathrm{keV}$, which is enough to illuminate the whole aperture of the focusing optics and therefor the sample coherently.

2.4 Interaction with matter

The interaction of an electromagnetic wave with a material of thickness d can simply be written as:

$$\vec{E}_{out}(d) = \vec{E}_{in} \cdot \exp\left(\mathrm{i}k \int_0^d n\,\mathrm{d}z\right), \tag{2.16}$$

where n describes the complex refractive index of the material the X-rays are interacting with. This refractive index is often written as:

$$n(\omega) = 1 - \delta(\omega) + \mathrm{i}\beta(\omega), \tag{2.17}$$

where δ is the decrement of the real part of refractive index[1] and β is the imaginary part of the refractive index. Substituting n with equation 2.17 in equation 2.16 yields:

$$\vec{E}_{out}(d) = \underbrace{\vec{E}_{in} \cdot \exp\left(\mathrm{i}k \int_0^d 1\,\mathrm{d}z\right)}_{\text{wave in vaccum}} \cdot \underbrace{\exp\left(-\mathrm{i}k \int_0^d \delta\,\mathrm{d}z\right)}_{\text{phase shift}} \cdot \underbrace{\exp\left(-k \int_0^d \beta\,\mathrm{d}z\right)}_{\text{absorption}} \tag{2.18}$$

It can be seen that the incoming electromagnetic wave travels through the material like through vacuum, but receives two additional factors. The first additional factor only depends on δ and describes an additional negative phase shift. The second additional factor only depends on β and describes a reduction of the amplitude of the electromagnetic wave. In detail δ and β can

[1] compared to vacuum

be written as [40]:

$$\delta(\omega) = \frac{N_{EZ}}{2\pi} r_e \lambda^2 \left(Z + f'(\omega)\right) \tag{2.19}$$

$$\beta(\omega) = \frac{N_{EZ}}{2\pi} r_e \lambda^2 \left(f"(\omega)\right), \tag{2.20}$$

where N_{EZ} is the atomic number density, r_e is the classical electron radius, λ is the wavelength of the probing beam, Z is the atomic number of the material, $f'(\omega)$ and $f"(\omega)$ are the dispersion corrections of the atomic (forward) scattering factors. The atomic number density N_{EZ} is the product of Avogadro's number N_A and the mass density ρ of the material, divided by the atomic mass A of the material:

$$N_{EZ} = N_A \frac{\rho}{M} \tag{2.21}$$

The imaginary part β of the refractive index can be used to describe the Lambert-Beer law of attenuation of X-ray in matter. The intensity of an X-ray beam passing through the thickness d of a material along the z-axis is decreased according to:

$$I_{out} = I_{in} \cdot \exp\left(-\int_0^d \mu \, \mathrm{d}z\right), \qquad \text{where } \mu = \frac{4\pi}{\lambda}\beta = 2k\beta \tag{2.22}$$

The absorption coefficient $\mu(E_{ph})$ depends on the photon energy E_{ph} of the probing X-ray beam. This energy dependence is used to distinguish different elements or even different chemical states of the same element in techniques such as extended X-ray absorption fine structure (EXAFS) and X-ray absorption near edge structure (XANES).

The decrement δ of the real part refractive index describes the influence on the phase of the electromagnetic wave passing through the material. As the phase is always a relative measure, this influence is expressed relative to an identical incoming wave traveling through vacuum (see equation 2.18). When passing through a material of thickness d, an electromagnetic wave is shifted by ϕ compared to traveling the same distance in vacuum:

$$\phi = -\frac{2\pi}{\lambda}\int_0^d \delta \, \mathrm{d}z = -k\int_0^d \delta \, \mathrm{d}z \tag{2.23}$$

2.5 Kramers Kronig relation

The Kramers-Kronig relation [42,43] connects the real part and the imaginary part of a complex index of refraction. This allows to retrieve the real part, the dispersion if only the imaginary part, the absorption is measured or vice versa. Assuming the complex refractive index to be a frequency-dependent linear response function $X(\omega)$:

$$X(\omega) = X_R(\omega) + \mathrm{i}X_I(\omega) \tag{2.24}$$

This function is analytic in the closed upper half-plane of ω, as no physical system $X(t)$ can respond to a force before the force was applied. Therefore the real part $X_R(\omega)$ and the imaginary

part $X_I(\omega)$ are connected by:

$$X_R(\omega) = +\frac{1}{\pi}\mathcal{C}\int_{-\infty}^{\infty}\frac{X_I(\omega')}{\omega'-\omega}\,\mathrm{d}\omega'. = +\frac{2}{\pi}\mathcal{C}\int_{0}^{\infty}\frac{\omega' X_I(\omega')}{\omega'^2-\omega^2}\,\mathrm{d}\omega' \tag{2.25}$$

$$X_I(\omega) = -\frac{1}{\pi}\mathcal{C}\int_{-\infty}^{\infty}\frac{X_R(\omega')}{\omega'-\omega}\,\mathrm{d}\omega'. = -\frac{2}{\pi}\mathcal{C}\int_{0}^{\infty}\frac{\omega X_R(\omega')}{\omega'^2-\omega^2}\,\mathrm{d}\omega', \tag{2.26}$$

where $\mathcal{C}$ is the Cauchy principle value [44] at the poles $\omega = \omega'$. In mathematics those two relations are known as Sokhotski-Plemelj theorem and as Hilbert transform [45–47] In this work I will use the Kramers-Kronig relation to calculate the real part of the index of refraction from an EXAFS measurement of the imaginary part of the index of refraction. In other words, I will calculate the phase shift of a material from a measurement of the absorption of the material [48].

Chapter 3

Ptychography

Ptychography is the name for a coherent diffractive imaging method. The name was derived from by the greek words for "to fold" and "write/image" and was choosen by its inventors R. Hegerl and W. Hoppe [49]. This choice and how the "imaging via folding" can be understood will become clear as I explain the ptychographic model.

3.1 Ptychographic model

The basic ptychographic model, detached from any experimental background, revolves around two complex-valued functions: one is called „the object “ O, and the other one is called „the probe“ P. Lets assume that both O and P are defined in two spatial dimensions $\vec{\rho} = (\rho_x, \rho_y)$ (while in general one and more dimensions are also possible). The function $P(\vec{\rho})$ has a limited support and can therefore be considered as a mathematical window. During a ptychographical reconstruction, the initially unknown probe function $P(\vec{\rho})$ and object function $O(\vec{\rho})$ shall be retrieved from j discrete measurements. In the modeling of a single measurement the object function $O(\vec{\rho})$ is multiplied with the probe function $P(\vec{\rho})$, creating the so called „exit wave-front“ $\Psi(\vec{\rho})$:

$$\Psi(\vec{\rho}) = O(\vec{\rho})\, P(\vec{\rho}) \tag{3.1}$$

The actual measurement is not in ρ-space, but in the reciprocal k-space.

$$\psi\left(\vec{k}\right) = \mathcal{FT}\left[\Psi(\vec{\rho})\right] = \mathcal{FT}\left[O(\vec{\rho})\right] * \mathcal{FT}\left[P(\vec{\rho})\right] \tag{3.2}$$

The Fourier transform of a product is the convolution of the Fourier transforms of each factor. Hence, this equation is the origin of the word „folding “ in the name ptychography, as the word for convolution is "folding" in German. As a detector cannot measure the complex-valued function, it is the modulus square of the intensity that is measured:

$$I\left(\vec{k}\right) = \left|\psi\left(\vec{k}\right)\right|^2 \tag{3.3}$$

Consequently all phase information is lost during the measurement and only the amplitudes are known. The difference between the j measurements are the varying relative shifts $\Delta\vec{\rho}_j$ between the object $O(\vec{\rho})$ and probe $P(\vec{\rho} - \Delta\vec{\rho}_j)$:

$$I_j\left(\vec{k}\right) = \left|\mathcal{FT}\left[O(\vec{\rho})\, P(\vec{\rho} - \Delta\vec{\rho}_j)\right]\right|^2 \tag{3.4}$$

The so-called ptychographic problem is the extraction of the unknown object $O(\vec{\rho})$ and unknown probe $P(\vec{\rho})$ from the j measurements $I_j\left(\vec{k}\right)$ and the corresponding shift positions $\Delta\vec{\rho}_j$.

In X-ray microscopy the complex-valued probe function $P(\vec{\rho})$ descibes the wavefront of the probing beam at the sample position in the two lateral spatial dimensions $\vec{\rho}$. The size of the probing beam is restricted in order to guarantee the limited support of $P(\vec{\rho})$. The complex-valued object function $O(\vec{\rho})$ describes the influence on the probing beam when passing through the sample. The multiplication of P and O corresponds to the probing beam interacting with the sample and the Fourier transform to k-space is the Fraunhofer propagation to the far-field regime. The final absolute square represents the fact, that the phase of an electro-magnetic wave with wavelengths in the X-ray regime cannot be measured with the current detector technique, but only intensities. In the setup used for the measurements of this work the relative shifts $\Delta\vec{\rho}_j$ are actual spatial shifts of the sample lateral to the probing beam. A schematic overview of the ptychographic measurement is shown in Fig. 3.1.

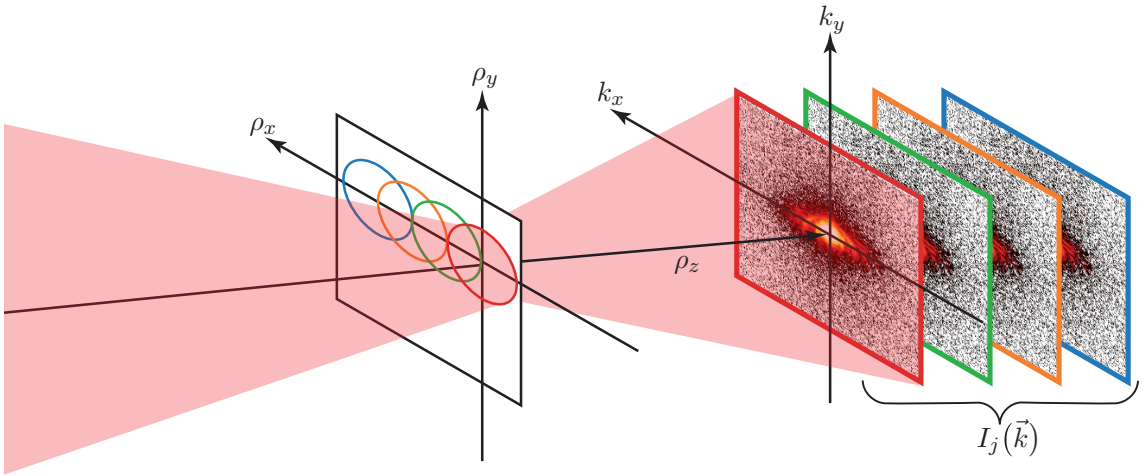

Figure 3.1: Schematic representation of the ptychographic measurement. The X-ray beam (red transparent) is probing the sample at multiple positions in the (ρ_x, ρ_y)–plane, propagates along the ρ_z–axis and is finally detected as a diffraction pattern in Fourier space.

3.2 Limits and approximations

Before I explain how the ptychographic problem is solved, I will discuss the approximations made by this model and the limits it imposes on the measurement.

3.2.1 Thin sample

In equation 3.1 the interaction between the probing beam P and the sample O is modeled as a simple multiplication. All thickness effects of the sample are neglected, as it is modeled as a thin slice which reduces the probing beam's amplitude and shifts the phase. The best approximation of this thin sample slice is the samples projection along the beam axis ρ_z:

$$O\left(\rho_x, \rho_y\right) = \exp\left(\mathrm{i}k \cdot \left[\int_{-\infty}^{+\infty} 1 - n\left(\vec{\rho}\right)\, \mathrm{d}\rho_z\right]\right), \tag{3.5}$$

where $n\left(\vec{\rho}\right)$ is the three dimensional distribution of the refractive index of the sample and k is the wavenumber of the probing beam. Substituting with equation 2.19 results in:

$$O\left(\rho_x, \rho_y\right) = \exp\left(\mathrm{i}k \cdot \int \delta\left(\vec{\rho}\right)\, \mathrm{d}\rho_z\right) \exp\left(-k \cdot \int \beta\left(\vec{\rho}\right)\, \mathrm{d}\rho_z\right), \tag{3.6}$$

shows that the integral over β only influences the amplitude of the probing beam, while the integral over δ determines the phase shift.

The integrals in equation 3.6 go from negative infinty to positive infinity. To fulfill the approximation of a thin sample, the sample should not extend beyond a length scale on which the beam profile changes drastically. For focusing optics the depth of focus (DOF) defines that length scale. Consequently, the sample has to be smaller than the DOF of the probing X-ray beam to justify the thin sample approximation.

Moreover, only single scattering is modeled within this simple multiplication of the probing wave field as a thin object slice. All multiple scattering effects which might occur in a real sample are not modeled. Therefore imaging strongly scattering materials might be outside the model and require extensions of the basic ptychographic model.

3.2.2 Far field

To model the propagation of the exit wavefront to the detector as a Fourier transform, two assumptions / approximations are made:

- the detector is placed far away from the sample and
- the diameter of the detector is small compared to this distance.

As described in chapter 2.2 those two assumptions allow the modeling of the propagation in the Fraunhofer regime as a simple Fourier transform.

Placing the detector too close or using a too large detector would require using Fresnel propagation instead of Fourier transforms (see equation 2.9) in the ptychographic model. In that case the method would be refereed to as near-field ptychography. All experiments presented in this work, were performed in the far field regime and thus the usage of the Fourier transform as far field propagation is applicable.

3.2.3 Coherence

As described in 2.3, the probing beam has to be coherent enough to be modeled as a single wave front $P(\rho_x, \rho_y)$. Hence, two requirements become clear:

First, the X-ray beam requires a minimal monochromaticity to have sufficient longitudinal coherence. This is the case, when all path length differences between all scattering vectors r from the probing beams $P(\rho_x, \rho_y)$ aperture to all points on the detector are smaller than the longitudinal coherence ξ_l.

Second, the (secondary) X-ray source is required to be small enough to have sufficient transversal coherence ξ_t over the whole aperture of the probing beam on the sample.

3.2.4 Photon noise

The intensities $I\left(\vec{k}\right)$ measured on the detector are probabilities of measuring a single photon at that scattering vector $\vec{k}$. As only discrete events (photons) can be measured, discrete statics limit the information measured in each diffraction pattern. More precise, the number of photons counted in each detector pixel follows Poisson statistics. In Poisson statistics the possibility $P_W(n)$ to observe n events, where W events are the expected (average) number of events, is:

$$P_W(n) = \frac{W^n}{n!} \exp(-W). \tag{3.7}$$

The standard deviation is simply the square root of the expected number of events W [50]. The highest achievable resolution in a ptychographical data set is limited by the largest scattering vector $\left|\vec{k}\right|$ at which sufficient signal-to-noise ratio (SNR) has been achieved in the recorded $I\left(\vec{k}\right)$. The SNR in a single measured diffraction pattern $I\left(\vec{k}\right)$ can be estimated as:

$$SNR\left(\vec{k}\right) = \frac{I\left(\vec{k}\right)}{\sqrt{I\left(\vec{k}\right)}} = \frac{\text{mean}}{\text{standard deviation}} \tag{3.8}$$

Using $SNR > 1$ as criterion, the largest scattering vector $\left|\vec{k}\right|$ at which in average more than 1 photon where recorded per pixel[1] sets the limit for the highest achievable resolution. Using all j measured diffraction patterns, the SNR can be estimated as:

$$SNR\left(\vec{k}\right) = \frac{I_\mu\left(\vec{k}\right)}{\sqrt{\frac{1}{J}\left(I_j\left(\vec{k}\right) - I_\mu\left(\vec{k}\right)\right)^2}} = \frac{\text{mean}}{\text{standard deviation}},$$

$$\text{where} \quad I_\mu\left(\vec{k}\right) = \frac{1}{J} I_j\left(\vec{k}\right) \quad \text{and} \quad J = \sum_j 1 \tag{3.9}$$

[1] radially averaged over the whole detector

To possibly improve the achievable resolution beyond the limit set by the photon statistics ($SNR > 1$) more photons need to be recorded. In a measurement this corresponds to exposing longer and thus prolonging the measurement or using a source with an increased flux of coherent photons. For an non-periodic object, the measured intensities decay strongly ($\propto \left|\vec{k}\right|^4$) with increasing scattering vector $\left|\vec{k}\right|$. Hence, ≈ 16 times more photons would be needed to double an achieved resolution.

3.2.5 Sampling

To reliably reconstruct the exit wavefront faithfully the discrete measurements $I_j\left(\vec{k}\right)$ need to be sampled properly to resolve the speckles in the diffraction patterns. The size of these speckles is defined by the size of the window function, the probing beam. The larger the probing beam $P\left(\vec{\rho}\right)$, the smaller the speckles in the diffraction pattern and consequently smaller detector pixels are required for sufficient sampling of the speckles. Or in other words, the probing beam needs to be small enough so that the detector pixels are sufficiently small to sample the diffraction patterns correctly: Calculating backwards from the known minimal sampling size in Fourier space, the size of the detector pixels Δs_{DET}, the corresponding maximal sampling in real space s_{max} at the sample position can be calculated to:

$$s_{max} = \frac{\lambda \cdot \Delta\rho_z}{\Delta s_{\text{DET}}}, \tag{3.10}$$

where λ is the wavelength of the probing beam and $\Delta\rho_z$ is the distance between sample and detector. To obtain an upper limit s_P for the maximum beam size, one utilizes the the Nyquist-Shannon sampling theorem [51] and the equal sign becomes a less than and a factor of one half is added:

$$s_P < \frac{\lambda \cdot \Delta\rho_z}{2 \cdot \Delta s_{\text{DET}}}. \tag{3.11}$$

If this relation is not fulfilled, then the minima and maxima of the interference patterns are not sufficiently resolved and the measured data cannot be reconstructed properly.

3.2.6 Step size

As half the information (the phase) is not measured, there has to be another way of redundancy in the measured data to make it possible to retrieve the missing phase information. In ptychography this redundancy comes from the overlap of the illuminated regions of adjacent scan points. How much relative overlap between adjacent scan points is needed for a faithful reconstruction depends on the shape and structure of the probing beam, the scan pattern utilized as it defines the directions in which the overlaps occur. As a rule of thumb, at least $50\,\%$ overlap between adjacent scan points should be achieved, while more is preferable [52].

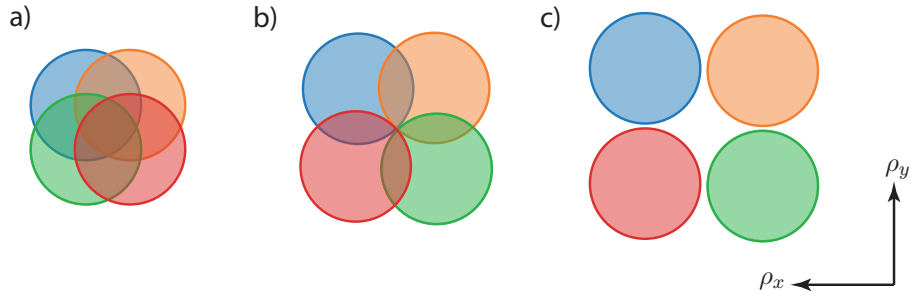

Figure 3.2: Schematic representation of the overlap requirements in 2D ptychography: a) sufficient overlap between adjacent scan positions, as the beam profiles overlap with all their neighbors and even overlap their next neighbors. A ptychographic reconstruction should not fail. b) critical overlap conditions, as beam profiles overlap only with their direct neighbors. A ptychographic reconstruction might fail. c) non-sufficient overlap, as the beam profiles do not overlap at all. A ptychographic reconstruction would fail.

3.2.7 Stability

In 3.1 the functions $P(\vec{\rho})$ are $O(\vec{\rho})$ are constant, meaning unchanged for all j measurements. Hence, this has to be reflected in the experiment. For the probe function $P(\vec{\rho})$ to be stable over the duration of the experiment, all X-ray optical components of the beamline as well as the electron orbit inside the storage ring of the synchrotron need to be kept stable. To this end, all components need to be build to withstand or even counteract external vibrations. The same is true for the mounting of the sample. Moreover, for the object function $P(\vec{\rho})$ to be stable over the duration of the experiment, the sample does not have to change during the measurement. The act of exposing the sample to the X-ray should not deform, melt or disintegrate the sample. This poses a challenge for biological sample, but most inorganic samples are able to deal with coherent X-ray fluxes achieved at current synchrotron light sources. Nonetheless, the stability of the sample in the probing beam has to be considered.

3.2.8 Summary

Multiple conditions have to be met to justify the usage of the ptychographic model as described above. Other experimental parameters have to be chosen correctly to even allow for a faithful reconstruction of the data. The made assumptions and necessary conditions mentioned above are summarized here:

- the sample is thin
- no multiple scattering occurs
- the detector is placed far away from the sample
- all scattered intensity is close to the optical axis[2]
- the probing beam is coherent
- sufficient statistics need to be measured in each diffraction pattern
- probing beam and sample have to stay unchanged during the measurement

[2] in this case where the Fourier transform should be used

- the detector pixels are small enough for the size of the probing beam
- the j shifts are small enough for sufficient overlap between neighboring scan positions.

3.3 ePIE algorithm

The inversion of the ptychographic problem boils down to one question: *Which $O(\vec{\rho})$ and $P(\vec{\rho})$ explain the measured diffraction patterns $I_j\left(\vec{k}\right)$ at the relative shifts $\Delta\rho_j$ best?* Multiple algorithms were developed to answer exactly this question. In the work at hand, the extended ptychographical iterative engine (ePIE) algorithm [53] is used for all reconstructions of ptychographic data. It is an iterative algorithm, which cycles between real space at the sample plane and reciprocal (Fourier) space at the detector position.

Initial estimates of the probe $P(\vec{\rho})$ and object $O(\vec{\rho})$ are created first. Then it is cycled over all measurement positions j in random order: The current estimate of the probe $P(\vec{\rho})$ is multiplied with the current object estimate $O(\vec{\rho})$ at the position $\Delta\vec{\rho}_j$ to create the estimated exit wave front $\Psi_j(\vec{\rho})$:

$$\Psi_j(\vec{\rho}) = P(\vec{\rho}) \cdot O(\vec{\rho} - \Delta\vec{\rho}_j) \tag{3.12}$$

The exit wave front is then propagated to the far field:

$$\psi_j\left(\vec{k}\right) = \mathcal{FT}\left[\Psi_j(\vec{\rho})\right] \tag{3.13}$$

There the amplitudes are replaced by the square root of the measured intensity $I_j\left(\vec{k}\right)$:

$$\hat{\psi}_j\left(\vec{k}\right) = \sqrt{I_j\left(\vec{k}\right)} \cdot \frac{\psi_j\left(\vec{k}\right)}{\left|\psi_j\left(\vec{k}\right)\right|} \tag{3.14}$$

The updated wave field $\hat{\psi}_j\left(\vec{k}\right)$ is then back-propagated to the sample plane:

$$\hat{\Psi}_j(\vec{\rho}) = \mathcal{FT}^{-1}\left[\hat{\psi}_j\left(\vec{k}\right)\right] \tag{3.15}$$

The difference between the previously estimated exit wave front $\Psi_j(\vec{\rho})$ and the updated exit wave front $\hat{\Psi}_j(\vec{\rho})$ has now to be separated into an update for the probe and the object function. This is done by multiplying with the complex conjugate of the other function:

$$O(\vec{\rho} - \Delta\vec{\rho}_j) \leftarrow O(\vec{\rho} - \Delta\vec{\rho}_j) + \alpha \frac{P_j^*(\vec{\rho})}{|P_j(\vec{\rho})|^2_{\max}} \left(\hat{\Psi}_j(\vec{\rho}) - \Psi_j(\vec{\rho})\right) \tag{3.16}$$

$$P(\vec{\rho}) \leftarrow P(\vec{\rho}) + \beta \frac{O_j^*(\vec{\rho} - \Delta\vec{\rho}_j)}{|O_j(\vec{\rho} - \Delta\vec{\rho}_j)|^2_{\max}} \left(\hat{\Psi}_j(\vec{\rho}) - \Psi_j(\vec{\rho})\right) \tag{3.17}$$

The updated probe $P(\vec{\rho})$ and object $O(\vec{\rho})$ are then used for the next measurement position j. Once all j were used one iteration of the ePIE algorithm has been performed. Complet-

ing N iterations concludes the ePIE algorithm. The complete ePIE algorithm is described in algorithm 1.

Algorithm 1 extended ptychographical iterative engine (ePIE)

procedure ePIE($I_j\left(\vec{k}\right), \Delta\vec{\rho}_j$)
  initalization of a estimated object $O\left(\vec{\rho}\right)$ and estimated $P\left(\vec{\rho}\right)$
  $O\left(\vec{\rho}\right) \leftarrow 1 + \mathrm{i}0$
  $P\left(\vec{\rho}\right) \leftarrow \text{gaussian}\left(\vec{\rho}\right) + \mathrm{i}0$ ▷ or known O or P
  loop N times
    for all measured diffraction pattens $I_j\left(\vec{k}\right)$ **do** ▷ in random order
      cropping of the object shifted by $\left(\vec{\rho}_j\right)$
      $O_j\left(\vec{\rho}\right) \leftarrow O\left(\vec{\rho} - \Delta\vec{\rho}_j\right)$
      multiplying with the probe $P\left(\vec{\rho}\right)$
      $\Psi_j\left(\vec{\rho}\right) \leftarrow O_j\left(\vec{\rho}\right) \cdot P\left(\vec{\rho}\right)$
      two-dimensional Fourier transform of the exit wave front $\Psi_j\left(\vec{\rho}\right)$
      $\psi_j\left(\vec{k}\right) \leftarrow \int\int \Psi_j\left(\vec{\rho}\right) \exp\left[\mathrm{i}\left(\vec{k}\vec{\rho}\right)\right] \mathrm{d}\vec{k}$
      replace the amplitudes of $\psi_j\left(\vec{k}\right)$ with the measured ones
      $\hat{\psi}_j\left(\vec{k}\right) \leftarrow \sqrt{I_j\left(\vec{k}\right)} \cdot \frac{\psi_j\left(\vec{k}\right)}{\left|\psi_j\left(\vec{k}\right)\right|}$
      inverse two-dimensional Fourier transform of $\hat{\psi}_j\left(\vec{k}\right)$
      $\hat{\Psi}_j\left(\vec{\rho}\right) \leftarrow \int\int \hat{\psi}_j\left(\vec{k}\right) \exp\left(\mathrm{i}\vec{\rho}\vec{k}\right) \mathrm{d}\vec{\rho}$
      update $O\left(\vec{\rho}\right)$ and $P\left(\vec{\rho}\right)$
      $O\left(\vec{\rho} - \Delta\vec{\rho}_j\right) \leftarrow O\left(\vec{\rho} - \Delta\vec{\rho}_j\right) + \alpha \frac{P_j^*\left(\vec{\rho}\right)}{\left|P_j\left(\vec{\rho}\right)\right|^2_{\max}} \left(\hat{\Psi}_j\left(\vec{\rho}\right) - \Psi_j\left(\vec{\rho}\right)\right)$
      $P\left(\vec{\rho}\right) \leftarrow P\left(\vec{\rho}\right) + \beta \frac{O_j^*\left(\vec{\rho} - \Delta\vec{\rho}_j\right)}{\left|O_j\left(\vec{\rho} - \Delta\vec{\rho}_j\right)\right|^2_{\max}} \left(\hat{\Psi}_j\left(\vec{\rho}\right) - \Psi_j\left(\vec{\rho}\right)\right)$
  return $O\left(\vec{\rho}\right)$ and $P\left(\vec{\rho}\right)$

3.4 Further algorithms

There are a few adjustment to the ePIE algorithm, each dealing with one or multiple approximations or conditions listed in 3.2.8. For samples that are too thick, there is the three-dimensional ptychographical iterative engine (3PIE) algorithm [54, 55], which will be presented later in detail. A variant of ePIE working with multiple probes was developed to deal with incoherent modes making up the probing beam [56–58]. An upscaling extension [59] of the ePIE algorithm allows to deal with slight too large probing beams. There is even a variant that can deal with a small incoherent background on all diffraction patterns [60]. Others even modify the measurement scheme to resolve smallest weakly scattering objects [22].

Apart from this group of ePIE-like algorithms, there is the difference-map algorithm, which is also widely used to reconstruct ptychographic data [61, 62]. But as it is never used in this work and therefore not presented here.

3.5 Spatial resolution estimation

The spatial resolution of an image is often estimated in order to quantitatively compare results of different imaging techniques or reconstruction algorithms. As a general approach, the spatial resolution could be defined as the capability to resolve features of a certain size at a given contrast. However, numerous ways to determine the spatial resolution have been established in the past and the results for one and the same image vary from method to method. Therefore, estimating the resolution goes hand in hand with exactly describing how the estimation was performed.

In ptychography the theoretically highest achievable spatial resolution is given by the highest scattering angle, where the signal of the sample is detected over noise. But even knowing this angle and the corresponding spatial resolution does not mean that this is also the resolution achieved in the reconstructed object. The implementation of the reconstruction algorithm, positioning errors and other deviations from the ptychographic model might decrease the actual spatial resolution in the reconstructed image. In this section, I will focus on methods only utilizing the reconstructed images.

Resolving known features

The most simple case of estimating the spatial resolution is knowing the size of certain features that were resolved in the reconstructed images. Their size is then an upper limit for the achieved spatial resolution, as the actual spatial resolution could be even better. But this approach can only truly claim the estimated resolution for those features at their respective positions in the image. Features of a similar size but weaker contrast in another part of the image might not have been resolved.

Fitting sharp edges

If sharp edges are present in the object, they can be used to estimate the spatial resolution. Extracting a profile across the sharp feature, such as an edge, one can measure the distance between the $10\,\%$ and $90\,\%$ level of contrast [63]. Fitting an error function to the profile and using the full width at half maximum (FWHM) of the underlying Gaussian as the resolution estimate is also often done. Nonetheless, this method can also just measure the resolution of one specific feature at one position inside the reconstructed image. Moreover the result is impaired by the assumption that the feature in question is in fact a perfectly sharp edge. Every inherent softness of the features is measured as additional worsening of the estimated spatial resolution.

Fourier ring correlation

The Fourier ring correlation (FRC) is a method to estimate the average spatial resolution in the reconstructed image in all directions and at all positions in the image. The FRC has been adopted from electron microscopy [64–66]. The resolution cannot be estimated with one reconstructed image alone, as the FRC compared the similarity of two images in Fourier space:

$$FRC_{12}(k) = \frac{\sum_k F_1\left(\vec{k}\right) \cdot F_1^*\left(\vec{k}\right)}{\sqrt{\sum_k \left|F_1\left(\vec{k}\right)\right|^2 \cdot \sum_k \left|F_2\left(\vec{k}\right)\right|^2}}, \tag{3.18}$$

where $F_1\left(\vec{k}\right)$ and $F_2\left(\vec{k}\right)$ are the two-dimensional Fourier space representations of the two images being compared.

To extract a spatial resolution from the calculated FRC curve, one has to find the point where it falls below a certain threshold criteria. Today the most utilized criteria are the half-bit criterion and the one-bit criterion [64]. The one-bit criterion is used when the two images, which are being compared, are both reconstructed from a full data set. On the other hand, the half-bit criterion is used when the two images are both reconstructed from a half data set.

Because the FRC only compares the similarity of the two images, and artifacts in the reconstructed images are not identified as such, one has to be careful with the resulting estimated spatial resolutions. Assuming the used image reconstruction algorithm, creates the same high-frequency artifacts in all reconstructions, comparing these reconstructions results in very good estimated spatial resolution. Or even worse: imagine the image reconstruction algorithm returning perfectly empty images. Calculating the FRC of two perfectly empty images would result in the spatial resolution estimate match the pixel size of the images.

Spatial signal to noise ratio

The calculated FRC can be used to calculate the spectral signal to noise ratio (SSNR) [65] of the two compared images:

$$SSNR_{12}(k) = 2\frac{FRC_{12}(k)}{1 - FRC_{12}(k)} \tag{3.19}$$

The resolution is then estimated by comparing the SSNR against a threshold of $SSNR_{12} \leq 1$.

$$2\frac{FRC_{12}(k)}{1 - FRC_{12}(k)} \leq 1 \Rightarrow FRC_{12}(k) \leq \frac{1}{3} \tag{3.20}$$

It can easily be seen that this is equal to comparing the FRC against a threshold of $FRC_{12} \leq 1/3$, which is a more rigorous criterion than the limit of the half-bit threshold. But plotting $SSNR_{12}$ logarithmic over k, allows for a linear fit of the whole curve, which is not that strong influenced by variations around the threshold criterion. Any deviations from the more or less

straight curve would also indicate that something is wrong and the used reconstructed images need to be double-checked.

3.6 Conclusion

Ptychography as a mathematical model was introduced and connect to scanning coherent X-ray imaging. Limitations and approximations of the X-ray ptychographic model were discussed. The iterative ePIE algorithm was presented as one robust algorithm able to solve the ptychographic problem. Finally multiple methods of estimating the spatial resolution of the reconstructed images were discussed.

Chapter 4

Tomography

Tomography is a term used for multiple methods, imaging cuts / planes through an otherwise opaque sample and revealing its inner structure without actually physically cutting the object. The most widely known technique, computed tomography (CT) is based on reconstructing the sample from measured sets of line integrals through the sample. In the next section I will explain the mathematical concept behind CT for the two-dimensional case, before I explain the extension to three dimensions.

4.1 Model of computed tomography

In the pure mathematical expression, the sample shall be represented by the function $f(r_x, r_z)$. The sample function $f(r_x, r_z)$ is non-zero only inside a circle with radius r_{max} around the origin. As mentioned above the measurements are sets of line integrals through the sample $f(r_x, r_z)$, the so called projections. In the most simple case all line integrals of one set are parallel to each other and the sets are distinguished by the angle between these parallel lines and the r_z axis (see Fig. 4.1a):

$$p_\Theta(\rho_x) = \int_{-\infty}^{+\infty} f(R_\Theta \cdot \vec{r}) \, \mathrm{d}\rho_z, \tag{4.1}$$

where R_Θ is the rotation matrix:

$$\vec{\rho} = \begin{pmatrix} \rho_x \\ \rho_z \end{pmatrix} = \begin{pmatrix} \cos\Theta & \sin\Theta \\ -\sin\Theta & \cos\Theta \end{pmatrix} \begin{pmatrix} r_x \\ r_z \end{pmatrix} = R_\Theta \cdot \vec{r}, \tag{4.2}$$

and ρ_x, ρ_z is the rotated cartesian coordinate system, sharing the origin with r_x, r_z. The totality of all projections p_Θ is called a sinogram as each position in the (r_x, r_z) plane lies on a sinusoidal path in the sinogram (see Fig. 4.1b). Expressing $f(r_x, r_z)$ in polar coordinates would make this even more obvious. The tomographic problem is the inversion of this measurement: to reconstruct $f(r_x, r_z)$ from the measured projections $p_\Theta(\rho_x)$. The Fourier slice theorem explains, why this inversion is even possible. It states that the one-dimensional Fourier transform

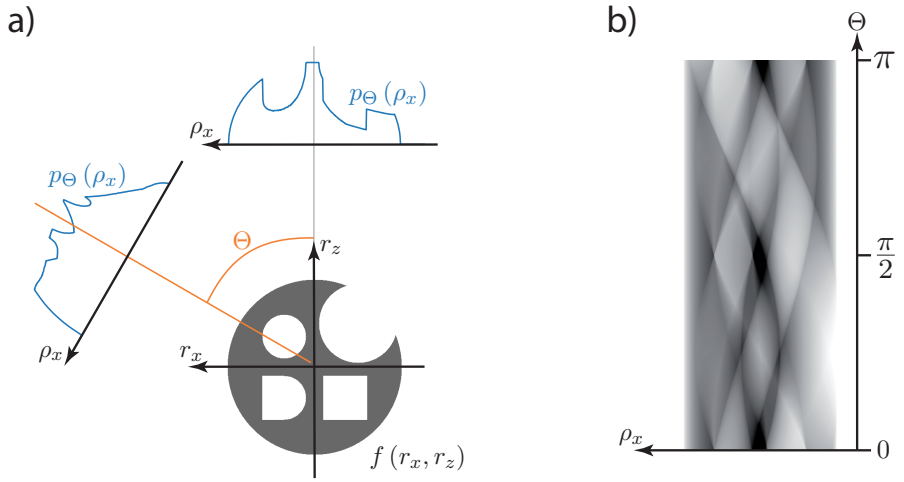

Figure 4.1: a) Schematic representation of the tomographic measurement of the sample $f(r_x, r_z)$ resulting in the projections $p_\Theta(\rho_x)$. b) Sinogram $p_\Theta(\rho_x)$ of the sample $f(r_x, r_z)$ shown in a).

of each projection $p_\Theta(\rho_x)$ equals a slice of the 2D Fourier transform of $f(r_x, r_z)$ through the origin under the angle Θ (see Fig. 4.2):

$$\int p_\Theta(\rho_x) \exp(\mathrm{i}q\rho_x)\, \mathrm{d}\rho_x = \int\int f(r_x, r_z) \exp(\mathrm{i}[q_x r_x + q_z r_z])\Big|_{q_x = q\cos\Theta, q_z = q\sin\Theta} \mathrm{d}r_z\, \mathrm{d}r_x \tag{4.3}$$

By measuring at multiple rotation angles Θ, the two-dimensional Fourier space representation of $f(r_x, r_z)$ is completely covered. Hence, a reconstruction of $f(r_x, r_z)$ must be possible as all information is there.

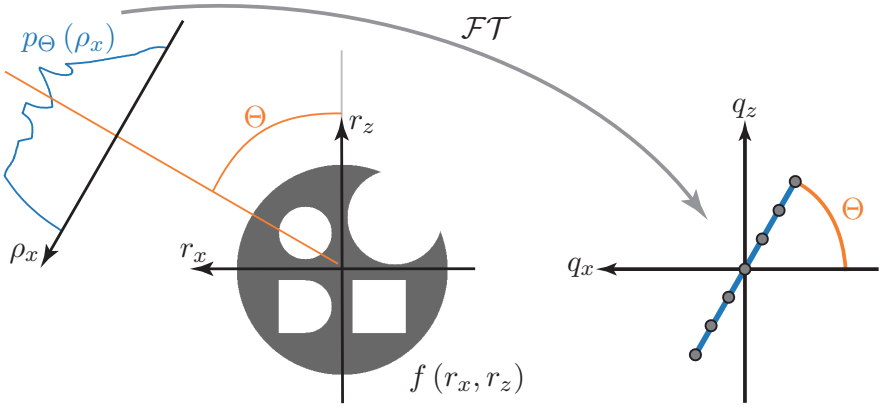

Figure 4.2: Schematic representation of the Fourier Slice Theorem showing how the one-dimensional Fourier transform of a projection $p_\Theta(\rho_x)$ represents a cut through the two-dimensional Fourier representation of $f(r_x, r_z)$ under the angle Θ.

4.2 Reconstruction algorithms

Most algorithms used for solving the tomographic problem can be divided into two groups. Firstly, those algorithms which follow the direct mathematical inversion of the projection mea-

surement. Secondly, iterative algorithms which start from an estimate for $f(r_x, r_z)$ and refine it every iteration by simulating the measurement, comparing against the actually measured data and using the difference to update the current estimate for $f(r_x, r_z)$. Algorithms from the first group are less demanding when it comes to computing resources and therefore faster, while algorithms from the second group usually produce fewer artifacts.

4.2.1 FBP algorithm

The most well known algorithm of the first group is called filtered back-projection (FBP) [67]. It is based on back-projecting the measured projections $p_\Theta(\rho_x)$ onto the two-dimension (r_x, r_z)–plane. The back-projection $b(r_x, r_z)$ of the projections $p_\Theta(\rho_x)$ is defined as:

$$b(r_x, r_z) == \int b_\Theta(r_x, r_z)\, \mathrm{d}\Theta = \int p_\Theta(\rho_x)\Big|_{\rho_x = r_x \cos\Theta + r_z \sin\Theta} \mathrm{d}\Theta \tag{4.4}$$

The two-dimensional Fourier transform of each single component $b_\Theta(r_x, r_z)$ has only non-zero Fourier components on the line through the origin under the angle Θ to the q_x–axis. These components are the same as the one-dimensional Fourier transform of $p_\Theta(\rho_x)$:. Because of the linearity of the Fourier transform, the integral over all $b_\Theta(r_x, r_z)$ has all measured Fourier components. Due to the sampling of Fourier space in polar-coordinates, the two-dimensional Fourier transform of $b_\Theta(r_x, r_z)$ is much denser sampled around the origin than further away from the origin. Not addressing this denser sampling, when switching between polar and cartesian coordinates results in the center components of the two-dimensional Fourier transform around the origin being pronounced too much, resulting in a blurring in real (r_x, r_z)–space.

This can be countered by weighting the one-dimensional Fourier components of the $p_\Theta(\rho_x)$ according to the Jacobi-determinant[1] before back-projecting them. Multiplying the Fourier components of $p_\Theta(\rho_x)$ with $|q|$ does exactly that:

$$\tilde{p}_\Theta(\rho_x) = \mathcal{FT}^{-1}\left(\mathcal{FT}\left[p_\Theta(\rho_x)\right]|q|\right) \tag{4.5}$$

Back-projecting these filtered projections $\tilde{p}_\Theta(\rho_x)$ results in the original function $f(r_x, r_z)$:

$$f(r_x, r_z) == \int \tilde{p}_\Theta(\rho_x)\Big|_{\rho_x = r_x \cos\Theta + r_z \sin\Theta} \mathrm{d}\Theta \tag{4.6}$$

The FBP algorithm is therefor the direct mathematical inversion of the projection measurement. Each projection is filtered by multiplying with $|q|$ in 1D Fourier space. The filtered projections $\tilde{p}_\Theta(\rho_x)$ are then back-projected on the (r_x, r_z)–plane to obtain $f(r_x, r_z)$. All steps are summarized in algorithm 2.

Instead of filtering with a wedge filter in 1D Fourier space, the filtering step could also be performed after the back-projection with a cone filter in 2D Fourier space. To be consistent with

[1] for the transformation between polar and cartesian coordinates

the naming convention, this algorithm should then be called back-projected filtering. Mathematically they are the same. Sometimes filter functions that drop to zero beyond a certain q_{max} are used instead of the $|q|$ wedge to suppress high-frequency noise in the reconstruction [68]. Those deviations from the exact mathematical inversion are sometimes necessary because they are more robust. Their usage depends on the noise level in the measured projections.

Algorithm 2 filtered back-projection (FBP)

1: **procedure** FBP($p(\rho_x, \Theta)$)
2: **one-dimensional Fourier transform** of the sinogram
$P(q_x, \Theta) \leftarrow \int p(\rho_x, \Theta) \exp(\mathrm{i} q_x \rho_x) \, \mathrm{d}\rho_x$
3: **filtering** by multiplying with the filter function
$\tilde{P}(q_x, \Theta) \leftarrow P(q_x, \Theta) \cdot H(q_x)$ ▷ $H(q_x) = |q_x|$
4: **inverse one-dimensional Fourier transform** of the filtered sinogram
$\tilde{p}(\rho_x, \Theta) \leftarrow \int \tilde{P}(q_x, \Theta) \exp(-\mathrm{i} \rho_x q_x) \, \mathrm{d}q_x$
5: **back-projection** of the whole filtered Sinogram
$\tilde{f}(r_x, r_z) \leftarrow \int \tilde{p}(r_x \cos\Theta + r_z \sin\Theta, \Theta) \, \mathrm{d}\Theta$
6: **return** $\tilde{f}(r_x, r_z)$

4.2.2 SART algorithm

As example for the iterative algorithms, I am presenting here the simultaneous algebraic reconstruction technique (SART) algorithm [69–71]. It starts with an estimation $\tilde{f}(r_x, r_z)$ of the sample. Then it iterates over all recorded projection angles Θ, one by one. For each angle the projection $\tilde{p}_\Theta(\rho_x)$ is calculated:

$$\tilde{p}_\Theta(\rho_x) = \int_{-\infty}^{+\infty} \tilde{f}(R_\Theta \cdot \vec{r}) \, \mathrm{d}\rho_z, \tag{4.7}$$

The simulated projection $\tilde{p}_\Theta(\rho_x)$ is then compared against the actually measured projection $p_\Theta(\rho_x)$:

$$\Delta p_\Theta(\rho_x) = p_\Theta(\rho_x) - \tilde{p}_\Theta(\rho_x) \tag{4.8}$$

The difference $\Delta p_\Theta(\rho_x)$ is then back-projected on the (r_x, r_z)–plane under the angle Θ and then added to estimate $\tilde{f}(r_x, r_z)$. This updates the estimate $\tilde{f}(r_x, r_z)$ to a state, where it's projection under the angle Θ matches the measured projection $p_\Theta(\rho_x)$. Repeating this update step of projecting, comparing and back-projecting the difference for all recorded projection angles Θ concludes one iteration of the SART algorithm. Performing N such iterations finalizes the whole algorithm. All steps are summarized in algorithm 3.

The *simultaneous* in the name of the algorithm comes from the update of the estimate $\tilde{f}(r_x, r_z)$ using all rays / line integrals from a single recorded projection $p_\Theta(\rho_x)$ simultaneous. Updating the estimate $\tilde{f}(r_x, r_z)$ ray by ray would make the algorithm the algebraic reconstruction technique (ART) algorithm [72, 73]. Updating the estimate $\tilde{f}(r_x, r_z)$ simultaneously using

all rays from all recorded projections, would make the algorithm the simultaneous iterative reconstruction technique (SIRT) algorithm [74].

Algorithm 3 simultaneous algebraic reconstruction technique (SART)

procedure SART($p(\rho_x, \Theta_j)$)
  initialize the object by guessing or using an empty one
  $\tilde{f}(r_x, r_z) \leftarrow 0$
  loop N times
    for all recorded Θ_j **do**
      projection of $\tilde{f}(r_x, r_y)$ under the angle Θ_j
      $\tilde{p}(\rho_x, \Theta_j) \leftarrow \int \tilde{f}(r_x = \rho_x \cos\Theta_k - \rho_z \sin\Theta_k, r_z = \rho_x \sin\Theta_k + \rho_z \cos\Theta_j)\ \mathrm{d}\rho_z$
      substraction of Δp from the measured projection $p(\rho_x, \Theta_j)$
      $\Delta p \leftarrow p(\rho_x, \Theta_j) - \tilde{p}(\rho_x, \Theta_j)$
      back-projection of $\Delta p(\rho_x, \Theta_j)$ on $\tilde{f}(r_x, r_z)$ under the angle Θ_j
      $\tilde{f}(r_x, r_z) \leftarrow \tilde{f}(r_x, r_z) + \Delta p(\rho_x = r_x \cos\Theta_j + r_z \sin\Theta_j, \Theta_j)$
  return $\tilde{f}(r_x, r_y)$

4.2.3 Other algorithms

As already mentioned there are multiple algorithms, which are similar to the FBP algorithm. In fact there are even more ways to perform the mathematically correct filtering, for example by taking the derivative of the projections $p_\Theta(\rho_x)$ along ρ_x and applying the Hilbert transform[2] [75]. As these algorithms are mathematically equivalent, they share the same strengths and weaknesses and knowing only the FBP algorithm as presented above does suffice.

The SART algorithm and other similar iterative algorithms [74, 76–79] are known to deal better with noisy projections, but most often require multiple iterations to converge properly. The SIRT algorithm is known to converge slower than the SART algorithm, while the ART algorithm is more prone to salt and pepper noise artifacts than the SART algorithm. As the basic principle of estimating the result, simulating the measurement, comparing to the actual measurement and using the difference to improve the estimated result is similar to the extended ptychographical iterative engine (ePIE) algorithm, the SART algorithm will be used later on instead of other tomography algorithms.

Besides these two groups of algorithms, other algorithms to solve the tomographic problem exist as well. Some are based on Maximum-likelihood methods [80–82], while others are based on reconstructing $f(r_x r_z)$ in two-dimensional Fourier space in cartesian coordiantes [83, 84].

[2] filtering with $-\mathrm{i}sgn(q)$

4.3 Limits

Angular sampling

To faithfully reconstruct $f(\vec{r})$ from the measured projections $p_\Theta(\rho_x)$ a sufficient number of unique projection angles needs to be recorded. The minimal needed number can be extracted from the Fourier slice theorem: Knowing that recording projections $p_\Theta(\rho_x)$ is sampling $F(q_x, q_z)$ radially, one should aim for an equal sampling of the outermost Fourier components in radial as in angular direction (see Fig. 4.1). Having achieved an resolution of $\Delta\rho$ in real space and a sample of diameter D results in having measured $N_{Res} = D/\Delta\rho$ resolution elements across the width of the sample. In Fourier space at least N_{Res} are needed to represent the N_{Res} resolution elements of each projection $p_\Theta(\rho_x)$. Hence, at least N_{Res} points are sampled on each radial axis in Fig.4.3. The angular sampling is simply the length of the arc divided by the number of unique projections N_Θ recorded over that arc.

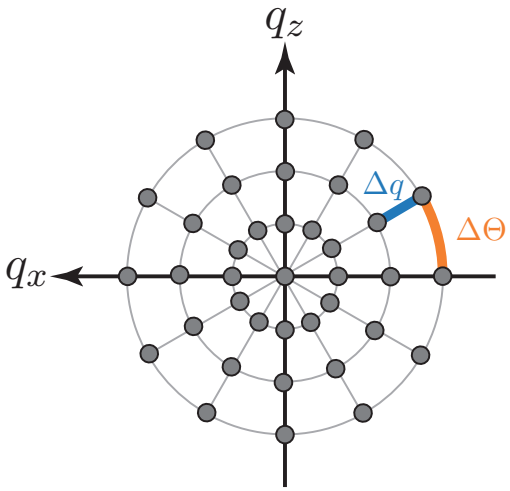

Figure 4.3: Tomographic sampling of $F(q_x, q_z)$ in Fourier space. The radial sampling Δq (blue) depends on the resolution elements across the width if the projections. The sampling along the arc $\Delta\Theta$ depends on the number of angular steps recorded.

$$\Delta\Theta = \frac{\pi}{N_\Theta} \approx \frac{2}{N_{Res}} = \Delta q \tag{4.9}$$

Solving for the necessary number of projections N_Θ yields:

$$N_\Theta \approx \frac{\pi}{2} N_{Res} \tag{4.10}$$

An additional factor of two is used, because of the Nyquist-Shannon sampling theorem [51] stating that $\geq 2 \cdot N_{Res}$ sampling points in Fourier space are needed to sufficiently sample the N_{Res} resolution elements in real space. With this factor equation 4.10 becomes:

$$N_\Theta \geq \pi N_{Res}. \tag{4.11}$$

This is also known as the Crowther criterion [85] for the number of needed projections to reconstruct $f(\vec{r})$ with a given resolution from these projections. It can also seen as a limit for the achievable resolution in the tomographic (r_x, r_z)–plane for a given number of projections.

Truncated sinograms

If the sample extends further than the field of view (FOV) of the projections the measured sinogram is truncated, because some features of the sample leave and re-enter the FOV of the projections while rotating the sample. The missing information can not be recovered without additional assumptions or knowledge about the sample. Some algorithms have been developed [86, 87] to mitigate the negative effects of truncated sinograms on the reconstructed $f(r_x, r_z)$. The best option is still to avoid this from happening, by having a small enough sample or a large enough field FOV in all projections to image the full width of the sample.

Sometimes the sample is just too large for recording sufficiently enough projections. In that case some projections can be recorded with a smaller FOV, but not all of them, allowing for the proper reconstruction of a small region of $f(r_x, r_z)$ [88]. During all tomography experiments presented in this work I have been careful to always image the full width of the sample.

Deviations from the model

Of course all deviations from the model result in artifacts, as the algorithms can not deal with something that does not fit the model. For example the tomographic model predicts, that the integral of each recorded projection $p_\Theta(\rho_x)$ equals the integral of $f(r_x, r_z)$ over the whole (r_x, r_z)–plane and is therefor independent of the rotation angle Θ.

$$\int p_\Theta(\rho_x)\, \mathrm{d}\rho_x = \int\int f(r_x, r_z)\, \mathrm{d}r_z\, \mathrm{d}r_x = const \tag{4.12}$$

Mathematically this is always true, but should the measurement not reflect this, the reconstruction algorithms will create artifacts in the reconstructed $f(r_x, r_z)$. The SART algorithm, for example, tries to counter this by placing artifacts at the outer edge of the reconstructed FOV. Therefor projections might have to be freed from arbitrary offsets to guarantee the integral of each projection to be the same. In the FBP algorithm, random offsets do not matter, because the $q = 0$ component of the Fourier representation is always multiplied by 0 and hence all absolute offset information is lost.

4.4 From 2D to 3D

The most simple way to extend the presented tomographic model to three spatial dimensions, is to model a three dimensional sample $f(r_x, r_y, r_z)$ only rotating around the r_y–axis. This way the projections become two-dimensional:

$$p_\Theta(\rho_x, \rho_y) = \int_{-\infty}^{+\infty} f\left(R_{\Theta,y} \cdot \begin{pmatrix} r_x \\ r_y \\ r_z \end{pmatrix}\right) \mathrm{d}\rho_z, \tag{4.13}$$

where $R_{\Theta,y}$ is the rotation matrix for the rotation around the r_y–axis:

$$\vec{\rho} = \begin{pmatrix} \rho_x \\ \rho_y \\ \rho_z \end{pmatrix} = \begin{pmatrix} \cos\Theta & 0 & \sin\Theta \\ 0 & 1 & 0 \\ -\sin\Theta & 0 & \cos\Theta \end{pmatrix} \begin{pmatrix} r_x \\ r_y \\ r_z \end{pmatrix} = R_{\Theta,y} \cdot \vec{r} \tag{4.14}$$

It can be seen that the r_y and ρ_y axis always coincide. For this reason, the three-dimensional problem can be separated into multiple independent two-dimensional problems as presented in 4.1 by fixing the height r_y (or coequal ρ_y).

In general the three-dimensional case allows for more arbitrary rotations [89], but in this work, the rotation axis is always the r_y-axis, hence these other cases are not relevant for the understanding of the presented experiments. In the next chapter I will discuss how this, purely mathematical discussion of tomography can be applied to three-dimensional ptychography.

Chapter 5

Ptychography in three dimensions

Extending the ptychographic model to the third spatial dimension along the beam axis has great benefits [23]. Most important is the possibility to overcome uncertainties of projection based imaging. It can clearly be resolved if something is before, inside or behind another structure. The complete internal structure of an object can be reconstructed. Quantitative values which rely on the exact thickness of the permeated sample are instantaneously possible.

5.1 Ptychographic X-ray computed tomography

The most widely used technique is based on the tomographic model presented in 4.1 and is therefor fittingly named ptychographic X-ray computed tomography (PXCT).

5.1.1 Model

In 2D ptychography (see chapter 3) the two dimensional transmission object $O(\rho_x, \rho_y)$ was modeled as:

$$\begin{aligned} O(\rho_x, \rho_y) &= \exp\left(\mathrm{i}k \cdot \left[\int_{-\infty}^{+\infty} 1 - n(\vec{\rho})\ \mathrm{d}\rho_z\right]\right) \\ &= \exp\left(\mathrm{i} \cdot \underbrace{\left[k \cdot \int \delta(\vec{\rho})\ \mathrm{d}\rho_z\right]}_{=\phi(\rho_x,\rho_y)}\right) \exp\left(\underbrace{\left[-k \cdot \int \beta(\vec{\rho})\ \mathrm{d}\rho_z\right]}_{=a(\rho_x,\rho_y)}\right) \end{aligned} \tag{5.1}$$

, where $a(\rho_x, \rho_y)$ the logarithm of the amplitude reducing factor and $\phi(\rho_x, \rho_y)$ is the phase-shift on a probing beam with wave number k. The parallel line integrals along ρ_z through the three dimensional $\beta(\vec{\rho})$ and $\delta(\vec{\rho})$ describe the tomographic projections of these two volumes. Rotating the sample relative to the lab-system allows to record multiple projections $O_\Theta(\rho_x, \rho_y)$ of these two volumes under various projection angles Θ:

$$O_\Theta(\rho_x, \rho_y) = \exp\left(\mathrm{i} \cdot \underbrace{\left[k \cdot \int \delta(R_\Theta \vec{r})\ \mathrm{d}\rho_z\right]}_{=\phi_\Theta(\rho_x,\rho_y)}\right) \exp\left(\underbrace{\left[-k \cdot \int \beta(R_\Theta \vec{r})\ \mathrm{d}\rho_z\right]}_{=a_\Theta(\rho_x,\rho_y)}\right), \tag{5.2}$$

where R_Θ describes the transformation of the sample coordinates $\vec{r}$ to the lab coordinates $\vec{\rho}$ by rotating around the r_y–axis by the angle Θ. The PXCT measurement scheme is straight forward: Perform multiple 2D ptychographic measurements as described in chapter 3, while rotating the sample in between the single measurements.

5.1.2 Algorithm

Naively, the reconstruction of the measured volumes $\beta(\vec{r})$ and $\phi(\vec{r})$ should then be performed by: Firstly reconstructing all recorded projections $O_\Theta(\rho_x, \rho_y)$ on their own using any two-dimensional ptychography algorithm.

$$O_\Theta(\rho_x, \rho_y) \text{ and } P_\Theta(\rho_x, \rho_y) = \text{ptycho}\left(I_{\Theta,j}\left(\vec{k}\right), \Delta\vec{\rho}_{\Theta,j}\right) \tag{5.3}$$

Secondly extracting the integrals of $\beta(\vec{r})$ and $\phi(\vec{r})$ from the complex valued object functions $O_\Theta(\rho_x, \rho_y)$:

$$\text{projection}\left(\beta(\vec{r}), \Theta\right) = \int \beta\left(R_\Theta \vec{r}\right) \, \mathrm{d}\rho_z = \frac{\log\left|O_\Theta(\rho_x, \rho_y)\right|}{-k} \tag{5.4}$$

$$\text{projection}\left(\delta(\vec{r}), \Theta\right) = \int \delta\left(R_\Theta \vec{r}\right) \, \mathrm{d}\rho_z = \frac{\arg O_\Theta(\rho_x, \rho_y)}{k} \tag{5.5}$$

and finally reconstructing the volumes $\beta(\vec{r})$ and $\phi(\vec{r})$ from their projections using any tomography algorithm.

But before the final tomographic reconstruction of the two volumes can be performed, the projections have to be reconstructed using any ptychography algorithm. The separation of probe P and object O in 2D ptychography is ambiguous to the relative brightness / amplitude of the two functions. Making the sample twice as absorbing and the probe twice as bright would explain the very same diffraction patterns. Hence each $a_\Theta(\rho_x, \rho_y)$ can have an arbitrary offset, which can differ between projection angles Θ. The same is true for arbitrary phase offsets of all $\phi_\Theta(\vec{r})$. Those random offsets which differ between projections have to be removed, as they would result in artifacts in the tomographic reconstructions.

Besides the arbitrary phase offsets of P and O, there is also the possibility for P and O to both have an additional arbitrary phase wedge. If those phase-wedges in P and O have the same pitch but in inverse directions, those phase wedges cancel out in the multiplication and result in the exact same exit wave front. Hence, these possible arbitrary phase wedges of the projections $O_\Theta(\rho_x, \rho_y)$ (or $\phi_\Theta(\rho_x, \rho_y)$) need to be removed before the tomographic reconstruction.

The last preparation step is the alignment of all projections to each other with respect to a shared rotation axis [90]. As only relative shifts $\Delta\vec{\rho}_{\Theta,j}$ between exposures are known in the ptychographic reconstruction of the projections, the absolute positions are unknown. Often the sphere of confusion of the rotation stages used to rotate the sample is larger than the resolution achievable via X-ray ptychography. Not aligning the projections to another would result in artifacts in the tomographic reconstructions.

All steps together are summarized in algorithm 4.

Algorithm 4 PXCT algorithm in its most basic description.

procedure PXCT($I_{\Theta,j}\left(\vec{k}\right), \Delta\vec{\rho}_{\Theta,j}, P_\Theta\left(\vec{\rho}\right)$)
  create a complex valued 2D transmission object $O_\Theta\left(\vec{\rho}\right)$ for each projection angle Θ.
    ▷ initial entries $1 + \mathrm{i} \cdot 0$
  if no $P_\Theta\left(\vec{\rho}\right)$ are given **then**
    initialize appropriate $P_\Theta\left(\vec{\rho}\right)$ for each recorded projection angle Θ
  for every Θ **do**
    perfom the **ptychographic reconstruction** of that projection $O_\Theta\left(\vec{\rho}\right)$
    using $I_{\Theta,j}\left(\vec{k}\right)$, $\Delta\rho_{\Theta,j}$ and P_Θ ▷ e. g., by using the ePIE algorithm
  remove artifacts like phase wedges and phase wraps from $\phi_\Theta\left(\vec{\rho}\right)$
  if possible, **remove** arbitrary offsets in both volumes
    ▷ e. g., by setting a reference inside the volume to zero
  align the reconstructed projections $O_\Theta\left(\vec{\rho}\right)$ to each other
  separate the aligned projections $O_\Theta\left(\vec{\rho}\right)$ into:
    phase shift: $\phi_\Theta\left(\vec{\rho}\right) = \arg O_\Theta\left(\vec{\rho}\right)$
    and optical density: $a_\Theta\left(\vec{\rho}\right) = \log\left|O_\Theta\left(\vec{\rho}\right)\right|$
  use any **tomography** algorithm to reconstruct the volumes:
    $\Phi\left(\vec{r}\right) \leftarrow tomo\left(\phi_\Theta\left(\vec{\rho}\right), \Theta\right)$
    $A\left(\vec{r}\right) \leftarrow tomo\left(a_\Theta\left(\vec{\rho}\right), \Theta\right)$ ▷ e. g., by using the SART algorithm
  return $A\left(\vec{r}\right)$ and $\Phi\left(\vec{r}\right)$

5.1.3 Approximations and limits

As the PXCT model is directly based on the ptychographic model (see 3.1) and the tomographic model, it inherits the necessary approximations and limits from both methods.

By describing the interaction of the three-dimensional sample with the probing beam as a simple multiplication of the probing wave field with a thin slice, the thin sample approximations of the ptychographic model also have to apply here. Same goes for the exclusion of multiple scattering, measuring in the far-field, having a coherent beam, sufficient photons on the sample, sufficiently small detector pixels and enough overlap between adjacent exposure positions (see 3.2).

Are one or multiple of these points not fulfilled, then the projections $O_\Theta\left(\rho_x, \rho_y\right)$ cannot be reconstructed without artifacts or even reconstructed at all. Artifacts would hinder the alignment of the projections and subsequently worsen the tomographic reconstructions. As for those, the same requirements as in 4.3 apply. Depending on the diameter of the sample and the achieved resolution, enough projections need to be recorded to fulfill the Crowther criterion and to allow the same resolution in the tomographic plane.

5.2 Coupled ptychographic tomography

Recently a coupled ptychographic tomography algorithm [91] was proposed. Instead of first performing all ptychographic reconstructions of all recorded projections, followed by the to-

mographic reconstruction of those projections, the two steps of ptychography and tomography would be interlinked.

5.2.1 Model

The physical model is exactly the same as for the PXCT algorithm (see 5.1.1). The projections $a_\theta(\vec{\rho})$ and $a_\theta(\vec{\rho})$ of the two volumes $A(\vec{r})$ and $\Phi(\vec{r})$

$$a_\theta(\vec{\rho}) = \int R_\Theta A(\vec{r})\ \mathrm{d}\rho_z = -k \cdot \int R_\Theta \beta(\vec{r})\ \mathrm{d}\rho_z \tag{5.6}$$

$$\phi_\theta(\vec{\rho}) = \int R_\Theta \Phi(\vec{r})\ \mathrm{d}\rho_z = -k \cdot \int R_\Theta \delta(\vec{r})\ \mathrm{d}\rho_z \tag{5.7}$$

define the two dimensional transmission object O_Θ measured under each rotation angle Θ. But instead of reconstructing each projection by itself, the information about the reconstructed volumes $A(\vec{r})$ and $\Phi(\vec{r})$ is constantly shared.

It was shown that this sharing of information between projections, allowed to properly reconstruct the sample even when the horizontal overlap was not sufficient for the ptychographic reconstruction of each projection on its own. Even though the overlap inside the projection might not be sufficient to solve the ptychographic problem, there is overlap in the tomographic plane between different projections (see Fig. 5.1).

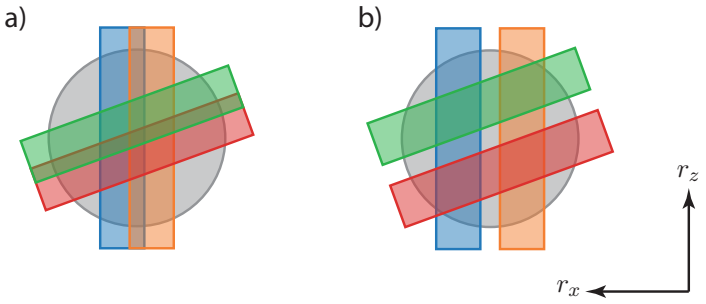

Figure 5.1: Schematic representation of the overlap requirements with the coupled ptychographic tomography (CPT) algorithm: a) the overlap is given between adjacent scan positions of same projections and between projections. b) adjacent scan positions of the same projection do not overlap anymore, but still overlap in the tomographic plane with the beam profiles from other projection angles.

5.2.2 Algorithm

The CPT algorithm used later in this work is based on the framework presented in [91], with the extended ptychographical iterative engine (ePIE) algorithm solving the ptychographic problem and the simultaneous algebraic reconstruction technique (SART) algorithm solving the tomographic problem.

At first the two volumes $A(\vec{r})$ and $\Phi(\vec{r})$ are both initialized with zeros, while suitable estimates for the probing wave fronts $P_\Theta(\vec{\rho})$ are made. Iterating sequentially over all recorded

projection angles Θ in a random order, the following steps are performed: First the projections $a_\theta(\vec{\rho})$ and $\phi_\theta(\vec{\rho})$ are obtained via projection according to equation 5.6 and equation 5.7. The complex-valued two-dimensional transmission object $O_\Theta(\vec{\rho})$ is then calculated according to equation 5.2. M iterations of the ePIE algorithm are performed using $O_\Theta(\vec{\rho})$ as initial object estimate and $P_\Theta(\vec{\rho})$ as probe estimate. The updated estimate for the probe is kept as $P_\Theta(\vec{\rho})$, while the difference between the initial object $O_\Theta(\vec{\rho})$ and the updated object $\hat{O}_\Theta(\vec{\rho})$ is calculated in both components:

$$\Delta a_\Theta(\rho_x, \rho_y) = \log\left|\hat{O}_\Theta(\rho_x, \rho_y)\right| - \log\left|O_\Theta(\rho_x, \rho_y)\right| \tag{5.8}$$

$$\Delta\phi_\Theta(\rho_x, \rho_y) = \arg\hat{O}_\Theta(\rho_x, \rho_y) - \arg O_\Theta(\rho_x, \rho_y) \tag{5.9}$$

Those two differences $\Delta a_\Theta(\vec{\rho})$ and $\Delta\phi_\Theta(\vec{\rho})$ are then back-projected on the two volumes $A(\vec{r})$ and $\Phi(\vec{r})$ under the projection angle Θ:

$$A(\vec{r}) \leftarrow A(\vec{r}) + \int R_{-\Theta}\,\Delta a_\Theta(\vec{\rho})\;\mathrm{d}r_z \tag{5.10}$$

$$\Phi(\vec{r}) \leftarrow A(\vec{r}) + \int R_{-\Theta}\,\Delta\phi_\Theta(\vec{\rho})\;\mathrm{d}r_z \tag{5.11}$$

This whole procedure of projecting, running the ePIE algorithm and back-projectiong the differences on the original volumes is repeated for the next projection angle (but with the updated $A(\vec{r})$ and $\Phi(\vec{r})$). Once all projection angles have been used, the first iteration of the CPT algorithm concludes. Running in total N iterations concludes the whole CPT algorithm. All steps are describes in detail in algorithm 5.

In general any other algorithm that solves the ptychographic problem could be used instead of the ePIE algorithm. If the back-projection would happen simultaneously over all recorded angles, one would refer to the tomography algorithm used as SIRT [92]. This would allow to run the calculations on all projections in parallel, which would speed up the iteration immensely. As the simultaneous iterative reconstruction technique (SIRT) algorithm is known to converge slower than the SART algorithm [69], I only used the CPT algorithm based on the SART algorithm as described above.

5.2.3 Approximations and limits

The CPT algorithm is based on the same model as the PXCT algorithm. Hence the same approximations and limits apply: The sample has to be thin along all projection direction and no multi-scattering occurs. The probing beam has to be coherent and small enough for the used detector pixels. The measurement is still performed in the far field and a sufficient number of photons is recorded during each exposure.

One alleviation is the relaxation of the overlapping constraint between adjacent exposure points. On the other hand it is assumed that all the measurement positions are already aligned

Algorithm 5 CPT algorithm according to the framework of [91] with M iterations of the ePIE algorithm [53] used as data constraint and the SART algorithm [69] for the object constraint.

procedure CPT($I_{\Theta,j}\left(\vec{k}\right), \Delta\vec{\rho}_{\Theta,j}, P_\Theta\left(\vec{\rho}\right)$)
  create a 3D array $A\left(\boldsymbol{r}\right)$ for the optical density and a 3D array $\Phi\left(\boldsymbol{r}\right)$ for the phase shift.
    ▷ initial entries 0
  if no $P_\Theta\left(\vec{\rho}\right)$ are given **then**
    initialize appropriate $P_\Theta\left(\vec{\rho}\right)$ for each recorded projection angle Θ
  loop N times
    for every Θ **do**
      calculate the projections $a_\Theta\left(\rho_x, \rho_y\right)$ and $\phi_\Theta\left(\rho_x, \rho_y\right)$ under the angle Θ
      calculate the complex projection:
        $O_\Theta\left(\rho_x, \rho_y\right) = \exp a_\Theta\left(\rho_x, \rho_y\right) \cdot \exp\left(\mathrm{i}\phi_\Theta\left(\rho_x, \rho_y\right)\right)$
      do M ptychography iterations on $O_\Theta\left(\rho_x, \rho_y\right)$ using $I_{\Theta,j}\left(\vec{k}\right)$, $\Delta\rho_{\Theta,j}$ and P_Θ to obtain an updated guess $\hat{O}_\Theta\left(\rho_x, \rho_y\right)$ for that projection
        ▷ e. g., using the ePIE algorithm
      calculate the phase shift update:
        $\Delta\phi_\Theta\left(\rho_x, \rho_y\right) = \arg\hat{O}_\Theta\left(\rho_x, \rho_y\right) - \arg O_\Theta\left(\rho_x, \rho_y\right)$
      and optical density update:
        $\Delta a_\Theta\left(\rho_x, \rho_y\right) = \log\left|\hat{O}_\Theta\left(\rho_x, \rho_y\right)\right| - \log\left|O_\Theta\left(\rho_x, \rho_y\right)\right|$
      calculate the 3D phase shift and optical density updates $\Delta\Phi_\Theta\left(\boldsymbol{r}\right)$ and $\Delta A_\Theta\left(\boldsymbol{r}\right)$ by back-projecting $\Delta\phi_\Theta\left(\rho_x, \rho_y\right)$ and $\Delta a_\Theta\left(\rho_x, \rho_y\right)$ under the angle Θ
      update the object volumes:
        $A\left(\boldsymbol{r}\right) \leftarrow A\left(\boldsymbol{r}\right) + \gamma \cdot \Delta A_\Theta\left(\boldsymbol{r}\right)$ and
        $\Phi\left(\boldsymbol{r}\right) \leftarrow \Phi\left(\boldsymbol{r}\right) + \gamma \cdot \Delta\Phi_\Theta\left(\boldsymbol{r}\right)$
        ▷ update strength $\gamma \in (0, 1]$
  return $A\left(\vec{r}\right)$ and $\Phi\left(\vec{r}\right)$

to each other and a shared rotation axis. To my knowledge the CPT algorithm has only been published with simulated data sets, which had perfectly known positions $\Delta\rho_{\Theta,j}$ [91, 93].

5.3 Multi-slice ptychography

Besides the tomography based methods there is another way of extracting information about the third spatial dimension from ptychographic data, once the thin-sample approximation does not apply any more.

5.3.1 Multi-slice model

To model a thick sample, it can be estimated by multiple thin slices $O_i\left(\vec{\rho}\right)$ placed certain distances $d_{i,i+1}$ apart from the next downstream slice. Each of the slices $O_i\left(\vec{\rho}\right)$ does not violate the thin-sample approximation. The probing X-ray beam $P\left(\vec{\rho}\right)$ propagates through the thick sample

by first scattering at the most upstream slice $O_{i=1}(\vec{\rho})$, creating the exit wavefront $\Psi_{i=1}(\vec{\rho})$:

$$\Psi_{i=1}(\vec{\rho}) = P(\vec{\rho})\, O_{i=1}(\vec{\rho})\,. \tag{5.12}$$

Afterwards the exit wavefront $\Psi_{i=1}(\vec{\rho})$ freely propagates the distance $d_{1,2}$ to the next slice in the downstream direction:

$$P_2(\vec{\rho}) = \Psi_{i=1}(\vec{\rho}) * \mathcal{P}_{1,2}(\vec{\rho})\,, \tag{5.13}$$

where $\mathcal{P}_{1,2}(\vec{\rho})$ is the free propagation kernel over the distance $d_{1,2}$ (see section 2.2). This procedure of interacting with each slice and propagating to the next one is repeated until the beam passed through the furthest downstream slice $O_{i=n}(\vec{\rho})$ to create the last exit wavefront $\Psi_{i=n}(\vec{\rho})$:

$$\Psi_{i=n}(\vec{\rho}) = (\left[\ldots([P(\vec{\rho})\, O_{i=1}(\vec{\rho})] * \mathcal{P}_{1,2}(\vec{\rho}))\ldots\right] * \mathcal{P}_{n-1,n}(\vec{\rho}))\, O_{i=n}(\vec{\rho}) \tag{5.14}$$

This last exit wavefront is then propagated to the far-field where the diffraction pattern is measured by the detector, exactly like in the two-dimensional ptychographic model (see 3.1).

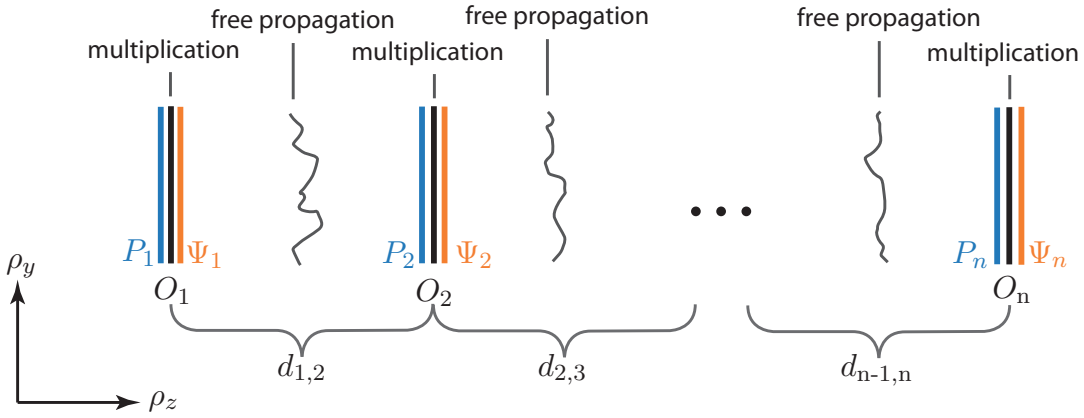

Figure 5.2: Schematic representation of the propagation of the probing beam through the thick sample modeled by n thin slices $O_i(\vec{\rho})$. At each object slice $O_i(\vec{\rho})$ the incoming probing wave field $P_i(\vec{\rho})$ is multiplied with the object slice to create the exit wave front $\Psi_i(\vec{\rho})$. Free propagation of this exit wavefront over the distance $d_{i,i+1}$ creates the next initial probing beam P_{i+1}.

5.3.2 Algorithm

The three-dimensional ptychographical iterative engine (3PIE) algorithm was developed on the model described above to deal with thicker samples [54, 94, 95].

For all recorded measurement positions $\Delta\vec{\rho}_j$ in random order the object slices $O_i(\vec{\rho})$ and probe $P(\vec{\rho})$ are updated as followed: Using n discrete object slices $O_i(\vec{\rho})$ the propagation through the sample is described by consecutive multiplications and propagations through empty space. The final propagation from the most downstream slice to detector is still implemented as a Fourier transform, as in the ePIE algorithm. The amplitudes are replaced by the square-root of

the measured intensities and the resulting wave field is back-propagated to the most downstream object slice resulting in $\hat{\Psi}(\vec{\rho})$. There the object slice and the n-th probe is updated exactly as in the ePIE algorithm:

$$O_{i=n}(\vec{\rho}-\Delta\vec{\rho}) \leftarrow O_{i=n}(\vec{\rho}-\Delta\vec{\rho}_j) + \alpha \frac{P^*_{i=n,j}(\vec{\rho})}{|P_{i=n,j}(\vec{\rho})|^2_{\max}} \left(\hat{\Psi}_{i=n,j}(\vec{\rho}) - \Psi_{i=n,j}(\vec{\rho})\right) \tag{5.15}$$

$$P_{i=n}(\vec{\rho}) \leftarrow P_{i=n}(\vec{\rho})\, \beta \frac{O^*_{i=n,j}(\vec{\rho}-\Delta\vec{\rho}_j)}{|O_{i=n,j}(\vec{\rho}-\Delta\vec{\rho}_j)|^2_{\max}} \left(\hat{\Psi}_{i=n,j}(\vec{\rho}) - \Psi_{i=n,j}(\vec{\rho})\right) \tag{5.16}$$

The probe function $P_{i=n}(\vec{\rho})$ is then back-propagated to the next object slice in the upstream direction:

$$\hat{\Psi}_{i=n-1}(\vec{\rho}) = P_{i=n}(\vec{\rho}) * \mathcal{P}_{n,n-1}, \tag{5.17}$$

where $\mathcal{P}_{n,n-1}$ is the free back-propagation kernel for the distance $d_{n-1,n}$. This $\hat{\Psi}_{i=n-1}$ is then used as input for the update of object slice $O_{i=n-1}(\vec{\rho}-\Delta\vec{\rho})$ and the probe $P_{i=n-1}(\vec{\rho})$. The procession of updating a single slice and the probe function at the slice's position and propagation to the next upstream slice is repeated until the most upstream slice was reached and the initial $P(\vec{\rho}) = P_{i=1}(\vec{\rho})$ was updated.

Then the procedure of propagating through all slices, comparing with the measured diffraction pattern and back-propagating and updating through all slices is repeated for all other j measurement positions. Performing N iterations over all j measurements concludes the algorithm. A detailed description of the 3PIE algorithm is given in algorithm 6.

5.3.3 Approximations and limits

The approximations for the 3PIE algorithm are very similar to those of the basic ePIE algorithm (see 3.2). Each of the object slices needs to be thin and no multi-scattering occurs inside a single object slice. This translates to: There need to be enough thin slices, spaced closed enough such that the thick sample can be modeled like that. The detector has to be placed in the far-field regime from the most downstream slice. The probing beam still has to be coherent, to interfere with itself on the detector. As the beam propagates through the sample it changes its size when interacting with the next slices. The detector pixels have to be small enough to sample the probing beam correctly at all object slice positions. Hence, a very divergent beam might be unsuited to measure thicker samples, as the beam diameter changes too much when propagating through the sample.

The criterion for the amount of overlap between adjacent measurement positions is more difficult to evaluate. As the beam diameter is different at the multiple object slices and yet everything reconstructs together, a slightly reduced overlap at some of the slices might be tolerable. Not tolerable would be non-overlapping probes at one or more of the slices positions (see Fig. 5.3). The redundancy from the overlap is needed for ptychographic reconstruction and separation of probe and object. Not having this redundancy in this slice causes the ptychographic

Algorithm 6 three-dimensional ptychographical iterative engine (3PIE) algorithm based on a multi-slice model as presented in [54, 94].

procedure 3PIE($I_j\left(\vec{k}\right), \Delta\vec{\rho}_j$)
  initialization of the n estimated object slices $O_i\left(\vec{\rho}\right)$ and estimated probe function $P\left(\vec{\rho}\right)$ (at the most upstream slice $j = 1$)
    $O_i\left(\vec{\rho}\right) \leftarrow 1 + \mathrm{i}0$
    $P_{j=1}\left(\vec{\rho}\right) \leftarrow \text{gaussian}\left(\vec{\rho}\right) + \mathrm{i}0$ ▷ or known O or P
  loop N times
    for all measured diffraction pattens $I_j\left(\vec{k}\right)$ **do** ▷ in random order
      cropping of all object slices shifted by $\left(\Delta\vec{\rho}_j\right)$
      $O_{i,j}\left(\vec{\rho}\right) \leftarrow O_i\left(\vec{\rho} - \Delta\vec{\rho}_j\right)$
      for all i object slices from furthest upstream to furthest downstream **do**
        multiply with the probe estimate $P_i\left(\vec{\rho}\right)$
        $\Psi_i\left(\vec{\rho}\right) \leftarrow O_{i,j}\left(\vec{\rho}\right) \cdot P_i\left(\vec{\rho}\right)$
        if not arrived at furthest downstream slice $O_{i=n,j}\left(\vec{\rho}\right)$ **then**
          propagate the exit wavefront $\Psi_{i,j}\left(\vec{\rho}\right)$ the distance $d_{i,i+1}$ to the next downstream slice to get the next P_{i+1}
          $P_{i+1}\left(\vec{\rho}\right) \leftarrow \Psi_i\left(\vec{\rho}\right) * \mathcal{P}_{i,i+1}\left(\vec{\rho}\right)$
      two-dimensional Fourier transform of the furthest downstream exit wave front $\Psi_{i=n,j}\left(\vec{\rho}\right)$
      $\psi_j\left(\vec{k}\right) \leftarrow \int\int \Psi_{i=n,j}\left(\vec{\rho}\right) \exp\left[\mathrm{i}\left(\vec{k}\vec{\rho}\right)\right] \mathrm{d}\vec{k}$
      replace the amplitudes of $\psi_j\left(\vec{k}\right)$ with the measured ones
      $\hat{\psi}_j\left(\vec{k}\right) \leftarrow \sqrt{I_j\left(\vec{k}\right)} \cdot \frac{\psi_j\left(\vec{k}\right)}{\left|\psi_j\left(\vec{k}\right)\right|}$
      inverse two-dimensional Fourier transform of $\hat{\psi}_j\left(\vec{k}\right)$
      $\hat{\Psi}_{i=n,j}\left(\vec{\rho}\right) \leftarrow \int\int \hat{\psi}_j\left(\vec{k}\right) \exp\left(\mathrm{i}\vec{\rho}\vec{k}\right) \mathrm{d}\vec{\rho}$
      for all i object slices from furthest downstream to furthest upstream **do**
        update $O_i\left(\vec{\rho}\right)$ and $P_i\left(\vec{\rho}\right)$
        $O_i\left(\vec{\rho} - \Delta\vec{\rho}_j\right) \leftarrow O_i\left(\vec{\rho} - \Delta\vec{\rho}_j\right) + \beta \frac{P^*_{i,j}\left(\vec{\rho}\right)}{\left|P_{i,j}\left(\vec{\rho}\right)\right|^2_{\max}} \left(\hat{\Psi}_{i,j}\left(\vec{\rho}\right) - \Psi_{i,j}\left(\vec{\rho}\right)\right)$
        $P_i\left(\vec{\rho}\right) \leftarrow P_i\left(\vec{\rho}\right) + \beta \frac{O^*_{i,j}\left(\vec{\rho} - \Delta\vec{\rho}_j\right)}{\left|O_{i,j}\left(\vec{\rho} - \Delta\vec{\rho}_j\right)\right|^2_{\max}} \left(\hat{\Psi}_{i,j}\left(\vec{\rho}\right) - \Psi_{i,j}\left(\vec{\rho}\right)\right)$
        if not arrived at furthest upstream slice $O_{i=1}\left(\vec{\rho}\right)$ **then**
          propagate the probe $P_i\left(\vec{\rho}\right)$ the distance $d_{i,i-1}$ to the next upstream slice to get the next $\hat{\Psi}_{i-1,j}$
          $\hat{\Psi}_{i-1,j}\left(\vec{\rho}\right) \leftarrow P_i\left(\vec{\rho}\right) * \mathcal{P}_{i+1,i}\left(\vec{\rho}\right)$
  return all object slices $O_i\left(\vec{\rho}\right)$ and the most upstream probe function $P_{i=1}\left(\vec{\rho}\right)$

problem in that slice to be unsolvable. From an information density point of view, reconstructing n object slices instead of just one would also mean about n-times more redundancy in the data set is needed to reconstruct those n object slices.

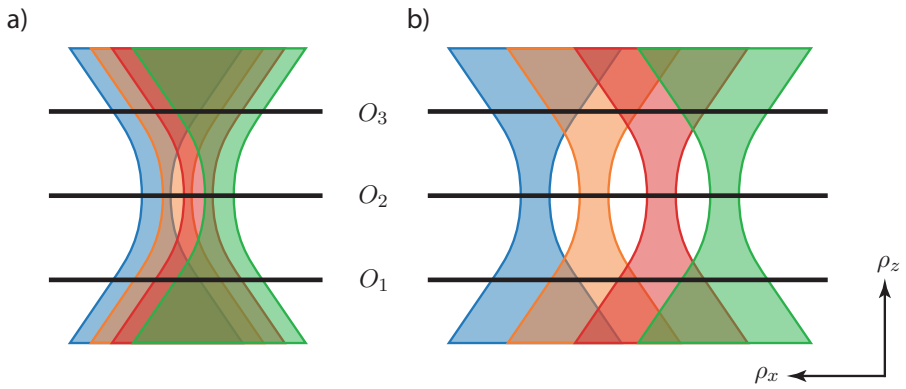

Figure 5.3: Schematic representation of the overlap requirements with the 3PIE algorithm and the converging beams: a) all four probing positions beams (blue,orange,red and green) overlap in all three modeled object slices O_1, O_2 and O_3. b) the four probing positions beams overlap at the slice positions of O_1 and O_3, but at the focus position of the probing beam there is no overlap between adjacent measurement positions.

The difficult experimenters decision is how many slices are needed to model the thick sample and how far apart / how close together do they need to be placed. This partly depends on the nature of the sample, partly on the length scale on which the probing X-ray beam changes by propagating and also on the lateral resolution achieved in all sample slices [55]. Just placing more slices along the beam axis, will not automatically result in an improved longitudinal resolution.

5.4 Quantitative evaluation

In 5.1.1 I already explained how $\Phi(\vec{r})$ can be understood as $k \cdot \delta(\vec{r})\ \mathrm{d}\rho_z$ and $A(\vec{r})$ equally as $-k \cdot \beta(\vec{r})\ \mathrm{d}\rho_z$. Hence phase shift on the probing beam by a single voxel $\Phi(\vec{r})$ can be converted to the average $\delta(\vec{r})$ by dividing by the wave number $k = 2\pi/\lambda$ and the edge length of the voxel l_{vox}:

$$\delta(\vec{r}) = \frac{\Phi(\vec{r}) \cdot \lambda}{2\pi \cdot l_{vox}} \tag{5.18}$$

This is supposed to be equal to equation 2.19. The term $(Z + f'(\omega))$ can be described as effective number of electrons per atom. Therefore the product with the atomic number density $n_a(\vec{r})$ equals the effective electron density $n_e(\vec{r})$:

$$\delta(\vec{r}) = \frac{\Phi(\vec{r}) \cdot \lambda}{2\pi \cdot l_{vox}} = \frac{r_e \lambda^2}{2\pi} \cdot n_e(\vec{r}) \tag{5.19}$$

Solving for the average effective electron density $n_e(\vec{r})$ inside the voxel's volume yields:

$$n_e(\vec{r}) = \frac{1}{r_e \cdot \lambda \cdot l_{vox}} \cdot \Phi(\vec{r}) \tag{5.20}$$

To calculate the effective electron density $n_e(\vec{r})$ seen by the X-ray beam along its path one has to divide the reconstructed phase shift per voxel $\Phi(\vec{r})$ by the classical electron radius r_e, the wavelength of the X-ray beam λ and the length of the voxel l_{vox} along the beam direction.

This is again an average over the voxel volume. Depending on the corrections terms $f'(\omega)$ of the included elements, the effective electron density $n_e(\vec{r})$ might differ more or less from the actual electron density present in the volume.

5.5 Resolution estimation

As in the two-dimensional ptychography case (see 3.5) one would like to estimate the achieved resolution of the reconstructed volumes. Fitting error functions across edges in the reconstructed volumes is an option, but would only result in local estimates. Moreover it is not always known how sharp the edge in question is to begin with.

The Fourier ring correlation (FRC) presented in 3.5 can be extended to three dimensions and is then fittingly named Fourier shell correlation (FSC). As in the 2D case the volumes $V_1(\vec{r})$ and $V_2(\vec{r})$ are compared in Fourier space:

$$FSC_{12}(k) = \frac{\sum_k F_1\left(\vec{k}\right) \cdot F_1^*\left(\vec{k}\right)}{\sqrt{\sum_k \left|F_1\left(\vec{k}\right)\right|^2 \cdot \sum_k \left|F_2\left(\vec{k}\right)\right|^2}}, \tag{5.21}$$

where $F_1\left(\vec{k}\right)$ and $F_1\left(\vec{k}\right)$ are the three-dimensional Fourier representations of $V_1(\vec{r})$ and $V_2(\vec{r})$. The same threshold criteria as for the FRC apply [64]. The one-bit threshold criterion is used to compare to volumes reconstructed from two complete data sets, while the half-bit threshold is used to compare volumes reconstructed from half data sets. The Fourier shell correlation estimates the average resolution along all spatial directions. As with the FRC, the FSC can be used to calculate a spectral signal to noise ratio (SSNR) [65]:

$$SSNR_{12}(k) = 2\frac{FSC_{12}(k)}{1 - FSC_{12}(k)} \tag{5.22}$$

These resolution estimations can also be performed on the multi-slice object reconstructed by the 3PIE algorithm. But the longitudinal resolution (between the slices) is always expected to be worse than the lateral resolution (in the $(\rho_x, \rho_y) - -plane$). Hence, averaging over all directions would overestimate the longitudinal resolution and underestimate the lateral resolution. Separating those two estimates is therefore advisable.

5.6 Outlook

The three presented algorithms for solving the ptychographic problem in three spatial dimensions are the core of this work. Three experiments will be presented, with having the focus on one of the algorithms each. The CPT algorithm will be used in chapter 6 The PXCT algorithm will be used in chapter 7 and in chapter 6. The 3PIE algorithm will be used in chapter 8.

Chapter 6

Macro-porous zeolite particle

The most important thing about an ptychographic X-ray computed tomography (PXCT) experiment is having a sample worth looking at. This means having a scientific questions that can be answered by reconstructing the three-dimensional structure of the sample using X-rays. The answer to this scientific question should not be obtainable by faster, cheaper or more accessible methods like for example transmission electron microscopy (TEM) tomography or X-ray tube based micro-tomography, to justify the usage of the limited time at a large research facility like a synchrotron.

In the first experiments I will discuss a hierarchically structured zeolite catalyst particle imaged using PXCT. But first I will motivate the experiment and justify the usage of this method.

6.1 Motivation of the experiment

Titanium inside nano-porous zeolites acts as a catalysts for the oxidation of various organic molecules. For the catalytic reaction to happen it is necessary for the organic molecule to reach the titanium site inside the nano-porous (pore sizes typically $< 1\,\mathrm{nm}$) zeolite material. The zeolite material itself is just a permeable crystalline frame to hold the catalytically active titanium and is in itself inert. Larger bulky organic molecules are too big to enter the tiny nano-pores, which limits the active catalytic regions to the surface of the bulk material. Grinding up the bulk material to nanometer sized particles largely increases the active surface, but complicates handling of the material and the fine dust also poses a health risk. Larger particles are easier to handle and poses a lower health risk. Therefore titanium zeolite catalyst particles with a size of a few micrometers with a hierarchical pore-structure have been synthezised [96]. The combination of larger and smaller pores allows for an increased mass transport of organic molecules through the material and an increased diffusion towards the active surfaces of the catalyst. The catalytic activity of a material can be measured in laboratories using model reactors. However, the actual physical properties of the zeolites, the pore size and inter-connectivity, are not easily accessible using lab measurements.

With sizes between $1\,\mu m$ and $2\,\mu m$ the zeolite particles are on the edge of what is possible to penetrate with electrons, which rules out high quality TEM reconstructions of whole particles. X-ray ptychography is not able to resolve the nano-porous structure of the zeolite, but the larger macro-pores. PXCT allows to image whole particles and might even allow for in-situ measurements, were the titanium zeolite particle is imaged while it is functioning as a catalyst.

6.2 Sample preparation

The sample was synthezised by Tobias Weissenberger [97] at the University of Erlangen. Calcinated mesoporous, spherical silica particles (MSPs) with a diameter of $600\,nm$ were impregnated with aqueous tetrapropylam-monium hydroxide solution, which made them stick together. The dried compound was then heated to $\approx 150\,°C$ to perform the steam-assisted crystallisation of the actual zeolite material. Interestingly, the zeolite material forms in between the initial MSPs while using up the Si of those spheres. After 48 hours the silica from MSPs material was mostly transfered into the zeolite matrix, leaving a zeolite crystal with spherical pores of $\approx 600\,nm$ diameter (see Fig. 6.1).

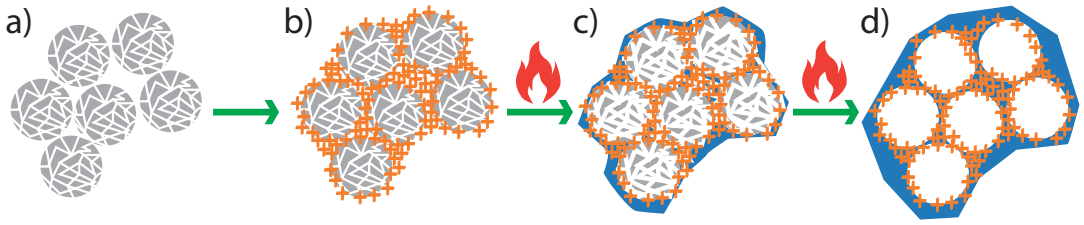

Figure 6.1: Scheme of the synthetization of the macro-porous zeolite particle: a) mesoporous, spherical silica particles (MSPs) (grey); b) MSPs with tetrapropylam-monium hydroxide (orange); c) sacrifice of the Si inside the MSPs for the growth of the zeolite crystal (blue); d) final partile.

A powder of zeolite particles was send to the DESY NanoLab. There, a focused ion-beam (FIB) microscope was used to select one of the particles and to glue it to a tungsten needle using beam induced deposition of platinum. An aluminum pin's tip was milled flat using FIB milling and a platinum cone was deposited on top of the tip to act as a podium for the sample particle. The particle was glued to this platinum podium using platinum allowing for an unobstructed view through the sample from $360°$. Afterwards the sample was milled free from the tungsten tip. A scanning electron microscopy (SEM) image of the final sample preparation is shown in Fig6.2.

The following elements can be expected around the sample:

- Al - in the sample holder pin
- Pt - below and on top the sample in the glueing points and podium
- Ga - residue from the focused ion beam
- Si, Al and Ti - in the sample itself
- W - maybe some left over from the transfer needle

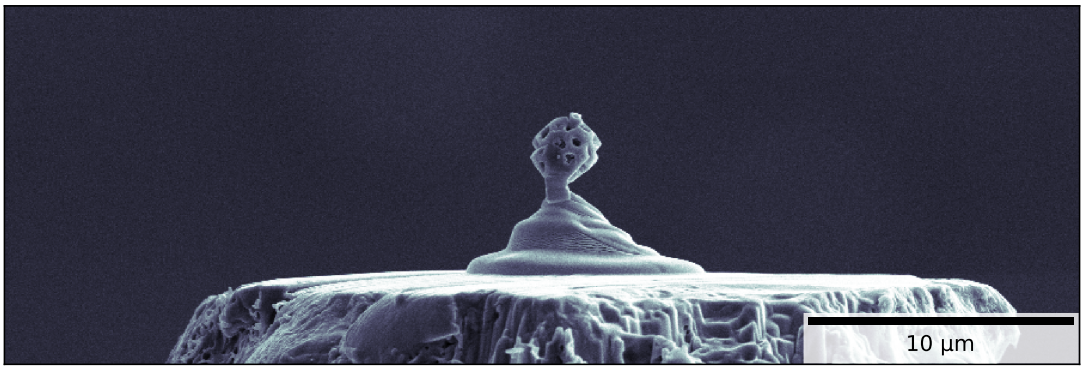

Figure 6.2: SEM image of the prepared zeolite particle on top of a Pt podium on top of the Al sample pin. The choosen particle has a width of $\approx 2.6\,\mu\mathrm{m}$.

6.3 Measurement

The experiment was performed at the hard X-ray nanoprobe endstation at beamline P06 at the PETRA III synchrotron radiation source (Hamburg, Germany) [41]. At this beamline, an undulator in the electron beam path is the source of X-rays. A double crystal monochromator (DCM) (Si 111) was used to select photons of an energy of $9\,\mathrm{keV}$. Furthermore a pair of mirrors downstream of the DCM was used to suppress the higher harmonic energies, which also pass through the DCM. Inside the last hutch of the beamline, the coherent fraction of X-ray beam was selected using slits and were afterwards focused using a Fresnel zone plate (FZP) to achieve a $70\,\mathrm{nm}$ sized focal spot at full width at half maximum (FWHM). The sample was placed $1\,\mathrm{mm}$ downstream of the focus using an optical microscope. This optical microscope was also used to align the particle to the center of rotation of the rotation stage below, so that it would not leave the beam when rotated.

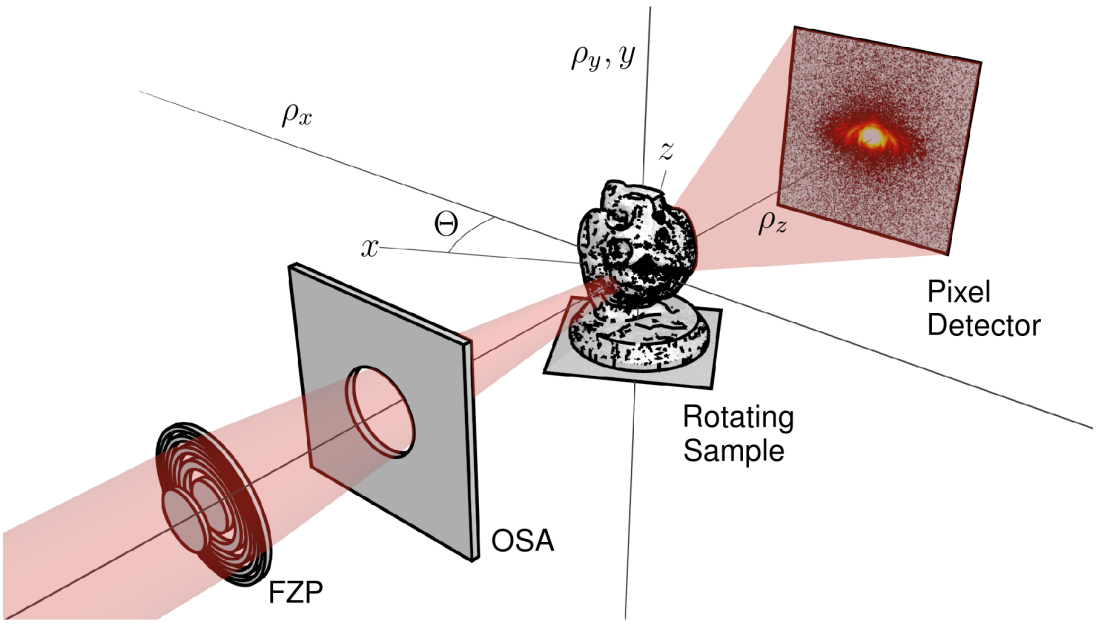

Figure 6.3: Ptychographic tomography measurement scheme: A probing beam (red) is focussed by the FZP though the OSA on a sample, which is scanned perpendicular to the incident beam along ρ_x and ρ_y. Rotating the sample around ρ_y by multiple angles Θ allows to record multiple projections of the sample.

The sample placement downstream of the focus increased the beam profile on the sample to $\approx 1800\,\mathrm{nm}$. This allows to take fewer steps / exposures within the same field of view and was done with the purpose of keeping the computational demands for the reconstruction as low as possible. The scanned field of view was $4\,\mu\mathrm{m} \times 4\,\mu\mathrm{m}$ in size, including the whole sample and a bit of air the left, right and top. The relative sample positions were recorded using an interferometer based sample tracking system. The step size in each direction was chosen to be $400\,\mathrm{nm}$, which is 4.5 times smaller than the beam size, allowing for sufficient overlap for ptychographic reconstructions. The diffraction patterns were recorded using an EIGER X 4M detector (DECTRIS, Switzerland), placed $2.13\,\mathrm{m}$. downstream of the sample.

Fourier ring correlation (FRC) of two reconstructions at opposite angles estimates a resolution of about $45\,\mathrm{nm}$, which is slightly smaller than size of the beam at the focus position. Using the Crowther critereon, I calculated that 90 are required over an arc of $180°$ to allow for $45\,\mathrm{nm}$ in the tomographic place. Therefor 91 projections were recorded in $2°$ steps. The whole tomographic measurement took about $7\,\mathrm{h}$ and resulted in $11 \times 11 \times 91 = 11\,011$ recorded diffraction patterns. All measurement parameters are summarized in table 6.1.

Table 6.1: Experimental parameters of the PXCT measurement done on the hierarchically structured zeolite particle on the 16th of June in 2018.

Parameter	
scan area ($h \times v$)	$4\,\mu\mathrm{m} \times 4\,\mu\mathrm{m}$
dwell time per scan point	$1\,\mathrm{s}$
number of points ($h \times v$)	$11 \times 11 = 121$
step size	$400\,\mathrm{nm}$
angular step size	$2°$
angular steps	91
angular range	$180°$
beam size on the sample (FWHM)	$1700\,\mathrm{nm}$
photon energy	$9\,\mathrm{keV}$
photon flux	$2.6 \cdot 10^8$ photons/s
sample-detector distance	$2.13\,\mathrm{m}$
detector pixel size	$75\,\mu\mathrm{m}$
overall measurement duration	$6.8\,\mathrm{h}$

6.4 Ptychographic X-ray computed tomography reconstruction

In following subsections, the conventional PXCT reconstruction of the data will be described. Afterwards, the coupled ptychographic tomography (CPT) reconstruction of the same data set will be presented in section 6.5. Finally both results will be compared in section 6.6.

6.4.1 Ptychographic reconstructions

To start off the PXCT reconstruction of the recorded data set, all diffraction patterns were cropped to a size of 512×512 pixel, resulting in a pixel size of $\approx 8.3\,\mathrm{nm}$ in the reconstructed images. Each projection was reconstructed by itself using the group-internal software called *ptycho* [98]. It is based on the extended ptychographical iterative engine (ePIE) algorithm [53, 62], is optimized to run on graphics processing units (GPUs) and has multiple extra-features on top of the basic ePIE algorithm. The following extension of the basic ePIE algorithm were applied for reconstruction.:

- A (brute force) position correction, refining the scan positions $\Delta\vec{\rho}_j$.
- An upscaling of the diffraction data by a factor of two, effectively simulating smaller detector pixels and allowing for a larger probe.
- The estimation and subtraction of an incoherent fraction of each diffraction pattern. [60]
- A parallel update over all exposure positions and not sequentially, starting from iteration 500, to more consistently update the whole Object $P\left(\vec{\rho}\right)$.

Each reconstruction of a projection was run for 5000 iterations on a dedicated node of the *MAXWELL* cluster located on the Deutsches Elektronen-Synchrotron (DESY) campus. As all reconstructions could be run in parallel on multiple machines, all reconstructions were completed within $6\,\mathrm{h}$.

Each reconstruction of a projection resulted in a complex-valued object $O_\Theta\left(\vec{\rho}\right)$, a complex-valued probing wave field $P_\Theta\left(\vec{\rho}\right)$ and a set of refined positions which will be used later on. The results of the reconstruction of the first recorded angle are shown in Fig 6.4.

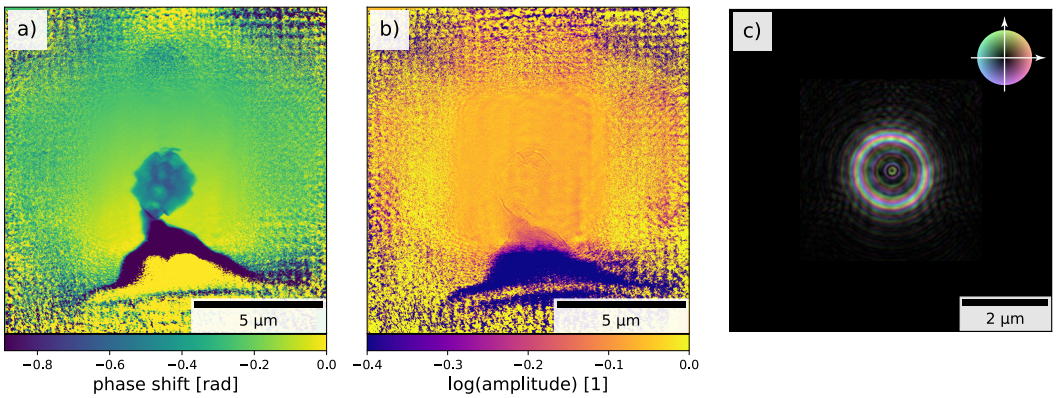

Figure 6.4: Ptychographic reconstruction of the first recorded projection; a) the reconstructed phase shift of the object; b) the logarithm of the reconstructed object amplitude and c) the reconstrucred probing beam, where the brightnes encodes the amplitude and the color encoded the phase

It can be seen that the whole particle on top of its platinum podium has been reconstructed. The sample itself is only phase-shifting and close to non-absorbing. Only the platinum podest and the Pt/Ga contamination on top of the particle show some detectable absorption. The edges of the reconstructed field of view (FOV) show the expected strong artifacts (see chapter 3), but the center is smooth and only shows a slight phase-wedge.

6.4.2 Projection alignment and artifact removal

To prepare all reconstructed projections for the tomographic reconstruction, artifacts were removed and afterwards the ptychographic reconstructions were aligned to each other.

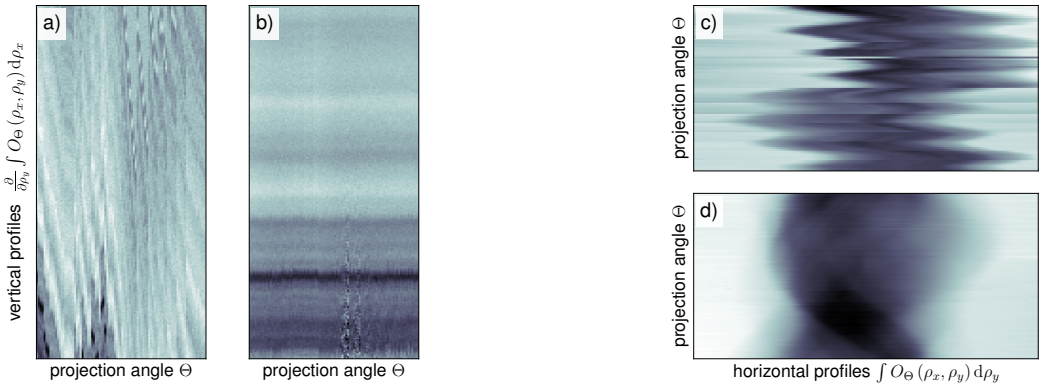

Figure 6.5: Left: (a) un-aligned and (b) aligned vertical profiles of all recorded projections; Right: (c) un-aligned and (d) aligned horizontal profiles of all recorded projections

Therefore all reconstructed objects $O_\Theta(\vec{\rho})$ were cropped to remove the strong artifacts at the edge of the FOV. Afterwards the phase-wedges in the background and the arbitary offset were removed by assuming all parts to the left, right and top of the sample to show air and were set to zero offset. With the worst artifacts removed the alignment was done using the horizontal and vertical line-integrals of the cleaned phases $\angle O_\Theta(\vec{\rho})$. The vertical alignment was done by correlating the derivative of the vertical profiles. The horizontal alignment was done by shifting the center of mass of the horizontal profiles to the horizontal center of the cropped field of view. After each of these alignment steps, the cropping and the calculation of the profiles was repeated as new features could have entered the FOV and some features might have left the FOV. These steps of vertical alignment and horizontal alignment were repeated alternatingly until a stable solution was found, meaning no further shifts had to be applied in each alignment step (see Fig. 6.5). Moreover the position of the rotation axis in the FOV was fixed. Here the horizontal center of the cropped FOV was chosen.

6.4.3 Tomographic reconstruction

The projections $O_\Theta(\vec{\rho})$ aligned and freed from artifacts and the knowledge about the position of the rotation axis the tomographic reconstruction could be done. First, the projections were separated in phase and amplitude images, and the natural logarithm of the amplitudes was calculated. Afterwards, each horizontal pixel line over projection angles was taken to create the sinograms (phase and log(amplitude)) for that height (see Fig. 6.5 d). These sinograms were reconstructed independently using the *gridrec* algorithm [83] implemented in the *tomopy*-package [99]. Stacking these reconstructed slices at all heights together created the two reconstructed volumes. The first volume represents the phase-shift of the probing beam by passing

through each and every voxel. The second volume represents the logarithm of the factor by which the amplitude of the probing beam is reduced by passing through each and every voxel. Both volumes are therefor just the products of the real- and the imaginary part of the refractive index and the wave number k. Two slices through both reconstructed volumes are shown in Fig. 6.6.

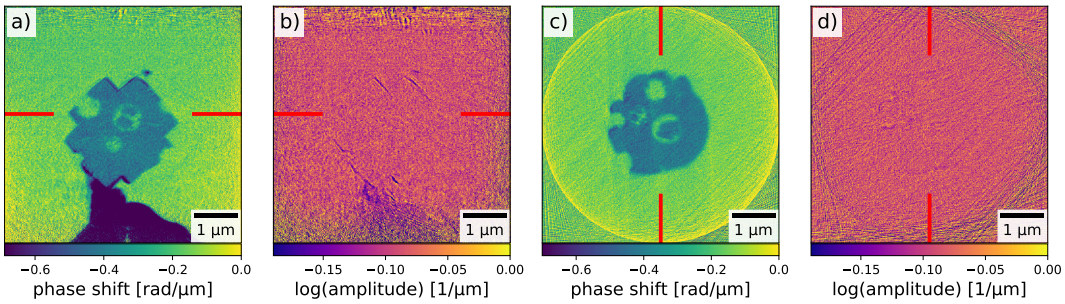

Figure 6.6: Slices through the PXCT reconstructed volume $k \cdot n\,(x, y, z)$: a) and b) show the same vertical slices; c) and d) show the same horizontal slice. The red lines in a) and b) indicate the positions of the horizontal slices shown in c) and d), while the red lines in c) and d) indicate the positions of the vertical slices shown in a) and b).

6.4.4 Quantitative evaluation

Using Eq. 5.20 the reconstructed phase-shift volume can be converted to effective electron-density. This reveals that the sample consists of a material with an electron density of $\approx 0.66\,\mathrm{e}/\mathrm{\AA}^3$ (see Fig.6.7). This is slightly below the values of $0.7\,\mathrm{e}/\mathrm{\AA}^3$ for pure bulk Si (molar volume of $12.06 \cdot 10^{-6}\,\mathrm{m}^3/\mathrm{mol}$) and $0.77\,\mathrm{e}/\mathrm{\AA}^3$ for pure bulk Al (molar volume of $10.10 \cdot 10^{-6}\,\mathrm{m}^3/\mathrm{mol}$) and can be explained by the hierarchical structure of the zeolite particle. Some pores are too small to be resolved, therefore slightly reducing the measured average electron density of each voxel. The voxel values for the podium are spread around $\approx 2.2\,\mathrm{e}/\mathrm{\AA}^3$ and cannot be explained bei neither pure Ga (electron density of $1.68\,\mathrm{e}/\mathrm{\AA}^3$; molar volume of $11.08 \cdot 10^{-6}\,\mathrm{m}^3/\mathrm{mol}$) nor pure Pt (electron density of $5.18\,\mathrm{e}/\mathrm{\AA}^3$; molar volume of $9.06 \cdot 10^{-6}\,\mathrm{m}^3/\mathrm{mol}$). Therefor it can be said that the podium does not consist of pure Pt. The deposition of Pt using beam induced deposition inside the FIB microscope is a rather chaotic process. It has to be assumed, that the deposited podium is a mixture of Pt, some organic carbon-hydrate as residue from the gas the Pt atoms were initially bound to and some Ga from the ion beam itself. This would explain the position of the podium peak between pure Ga and pure Pt (see Fig. 6.7c).

The successful reconstruction of the tomographic dataset facilitated further analysis steps to investigate the sample: For example the relative volume fraction of the macro-pores of the whole particle could be measured ($\approx 27\,\%$). The shape of each marco-pore could be compared. The inter-connectivity could be evaluated (three internal macro-pores are not connected to the surfaces via other macro-prores) [100]. However, these analysis procedures are beyond the scope of this thesis but can be found in [100] Instead the innovative way of reconstructing the

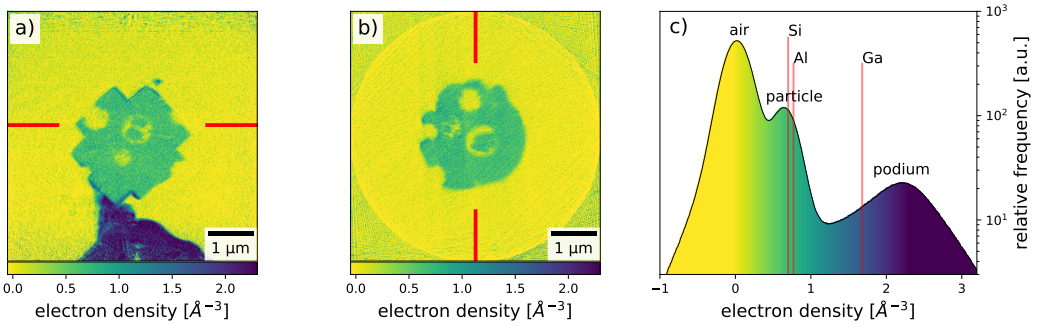

Figure 6.7: Vertical (a) and horizontal (b) slice through the reconstructed three-dimensional effective electron density distribution. c) shows the histogram over the whole volume with lines indicating the values expected for pure bulk materials.

same data set in a single step using the CPT algorithm will be presented in the next section.

6.5 Coupled ptychographic tomography reconstruction

The goal of the CPT reconstruction is to unify all the steps above and to reconstruct all recorded data in one step to increase the overall redundancy in the data set which should help to enforce a self-imposed consistency in the reconstruction.

6.5.1 First implementation

As the CPT reconstruction involves projecting from and back-projecting onto a complex-valued volume with every iteration and for every projection angle, the computational effort is considerably higher than for the PXCT reconstruction. Therefore step one is all about the reduction of the total amount of data. The diffraction patterns were cropped to a size of 256×256 pixel, resulting in a pixel size of $16.6\,\mathrm{nm}$. Moreover this reduces the computational expenditure for each ePIE-iteration by a factor of 4 and for each step involving a three-dimensional volume by a factor of 8, which will turn out to be very crucial for a reconstruction in a reasonable time. The refined position $\Delta\vec{\rho}_j$ obtained from the PXCT reconstruction were used for all following processing, eliminating the need to refine them during the ePIE step. Furthermore the knowledge about the relative shifts between projections and the absolute position of the rotation axis were also used. As the computational effort needed to be reduced even more, the additional refinements of the ePIE algorithm (upscaling, background subtraction and parallel update) were not used. Just the very basic ePIE algorithm (see algorithm 1) was used.

To properly compare the result of the CPT against the result of the PXCT reconstruction, both should be reconstructed from the same reduced data set and the same the basic implementation of the ePIE algorithm. Therefor the PXCT reconstruction was repeated using the reduced dataset. The CPT reconstruction was performed as described in algorithm 5. Both algorithms were initialized with a non phase-shifting and non-absorbing object and the same

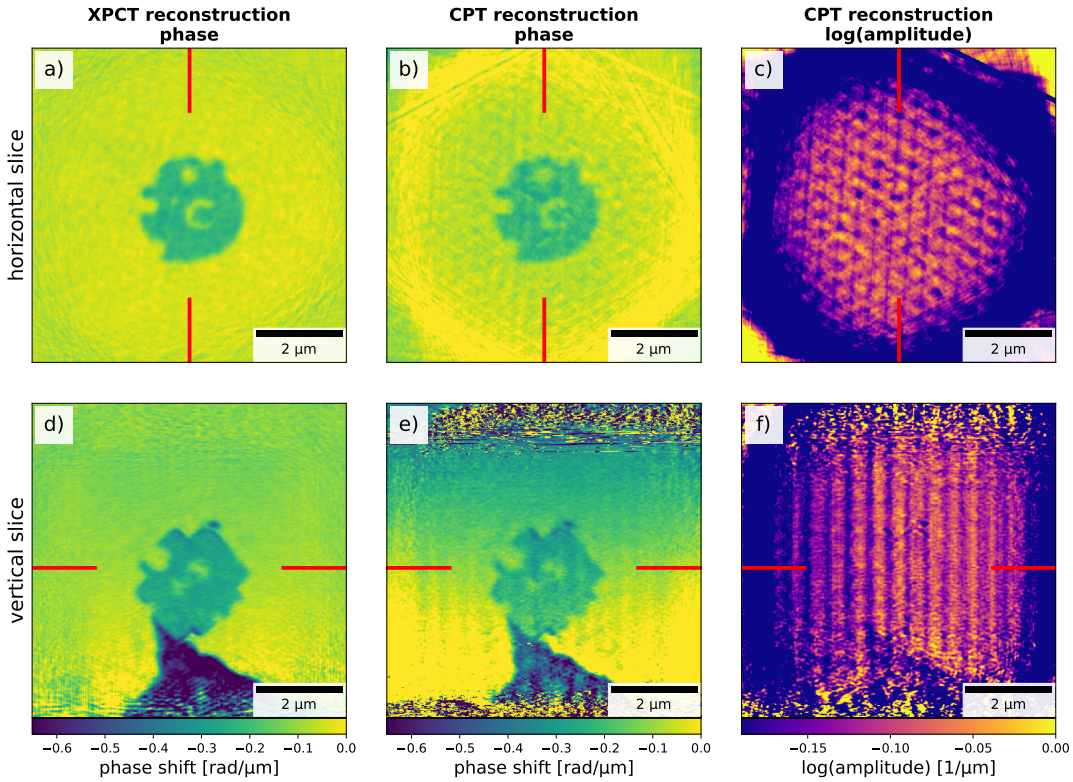

Figure 6.8: Slices though the PXCT reconstructed phase of the reduced data set (a and d) in comparison to the phase (b and e) and optical density (c and f) of the CPT reconstruction of the same data set.

starting guesses for the 91 probing wave fields. As the computational effort is enormous, 50 iterations of the CPT algorithm took about one week to finish. In contrast, performing 50 ePIE iterations for all projections during the PXCT reconstruction took only a few minutes, followed by 12 h needed to perform 50 iterations of SART (see algorithm 3).

The results of both reconstructions are shown in Fig.6.8. Unexpectedly the CPT reconstruction looks worse than the PXCT reconstruction. The slices are more grainy. The vertical slices show a stronger phase wedge. The podium is not reconstructed as far down as in the PXCT reconstruction. The absorption volume shows artifacts in form of strong vertical stripes.

As the conventional PXCT does not show these artifacts, there must be something in the data that the CPT algorithm can not tolerate, but the standard ePIE algorithm in two dimensions does.

6.5.2 Simulation of error sources

To investigate error sources occurring during the measurement and their influence on the result of the CPT algorithm I created a simulated data set. I started with the volume and the probes reconstructed by the conventional PXCT method (see Fig. 6.8). Everything outside a certain radius around the sample was set to zero. The resulting model volume was then used to simulate PXCT measurements with the following sources of errors:

- errors in the measured scanning position

- angular shifts of the beam axis
- incoherent background in the measured diffraction patterns
- fluctuating beam intensity

Wrong positions

The first possible error source is wrong positions. The sample-tracking laser interferometers could have been disturbed by fluctuations in the air path between sensor head and reflector, resulting in a disturbed measured scanning pattern. To simulate this, the simulated exposure positions were randomly shifted in both directions (see algorithm 7). The shifts followed a normal distibution. At these faulty positions otherwise perfect diffraction patterns were simulated using the volume and the probes from the simulated data set. The photon noise was chosen to match the experiment. Using the simulated diffraction patterns, but also the non-matching initial positions, CPT reconstructions were carried out, performing 50 iterations. Fig. 6.9 shows the result for 5 different width of normal distributed position errors, with the standard deviation σ varying between 1 and 5 times the pixel size.

Algorithm 7 Simulation of a PXCT dataset with wrong measured positions

procedure simulation wrong positions $(V(\vec{\rho}), P(\vec{\rho}), \Delta\vec{\rho}_j)$
  choose the strength σ of the position error
  $\sigma \leftarrow n \times 16.6\,\mathrm{nm}; n \in [1, \ldots, 5]$
  for all rotation angles Θ **do**
    calculate the projection $O_\theta(\vec{\rho})$
    for all measurement positions j under that angle Θ **do**
      add a random (normal distibuited) shift to $\Delta\vec{\rho}_j$
      $\Delta\vec{\varrho}_j \leftarrow \Delta\vec{\rho}_j + \mathcal{N}(\mu = \vec{0},\, \sigma^2)$
      simulate the diffraction pattern at the wrong position $\Delta\vec{\varrho}_j$
      $I_j(k) \leftarrow \left|\mathbf{FT}\left(O_\theta\left(\vec{\rho} - \Delta\vec{\varrho}_j\right) P(\vec{\rho})\right)\right|^2$
  return $I_j\left(\vec{k}\right)$ and $\Delta\vec{\rho}_j$

It can be seen that with increasing position errors, the reconstruction quality reduces. The air around the sample starts to show some of the graininess seen in Fig. 6.9 f, but not without reducing the quality of center part with the sample immensely. As refined positions were used in the initial CPT reconstructions and position errors of $\geq 50\,\mathrm{nm}$ were necessary to create similar levels of graininess in the simulation, position errors can be excluded as the main reason for the bad quality of the CPT reconstruction.

Changing beam direction

Another possible experimental source of errors can be the changing beam direction. The electron-orbit inside the synchrotron storage ring might not be stable during the whole experiment. It is known to sometimes slightly shift. This makes the electron bunches travel through the undulator in a slightly different path, creating the primary source in a slightly different place,

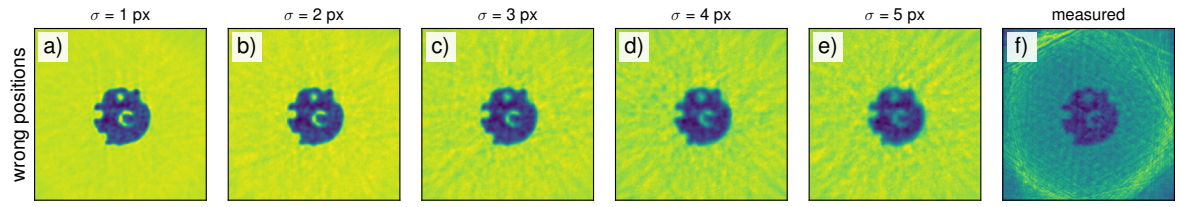

Figure 6.9: (a-e) simulation of the influence of inaccurate scanning positions on the CPT reconstruction of an otherwise perfect data set compared against (f) the CPT reconstruction of the real data set.

which in return is imaged by the optical beamline components to another position. In short, the beam might hit the sample under slightly different angles during the experiment. If the incident angle of the probing beam on the sample changes, the diffraction pattern on the detector shifts. In the ePIE algorithm the probe including its incident angle and phase is assumed to be constant over all scan points, consequently the varying incident angle of the beam results in additional phase wedge in the reconstructed object. If this phase wedge would be constant for a whole projection, meaning the angle of the incident beam would be constant for the duration of the measurement of a single projection, this wedge could simply be added to the probe. But if the angle changes more frequently, the various phase wedges could only be explained through the object, creating a very wavy, cloud-like background in the phase projection.

To simulate the influence of this on the CPT reconstruction perfect diffraction patterns were simulated as before, but with un-tampered positions. Afterwards the all diffraction patterns were randomly shifted in both dimensions, while the amount of shift and the direction again followed a normal distribution. The resulting data sets were again reconstructed using the CPT algorithm.

Algorithm 8 Simulation of a PXCT dataset with a changing beam angle

1: **procedure** simulation changing beam angle $(V(\vec{\rho}), P(\vec{\rho}), \Delta\vec{\rho}_j)$
2: **choose the strength σ of the angular changes**
$\alpha_{\max} \leftarrow n \times 0.035\,\mu\text{rad}; n \in [1, \ldots, 5]$
3: **for all** rotation angles Θ **do**
4: **calculate the projection** $O_\theta(\vec{\rho})$
5: **for all** measurement positions j under that angle Θ **do**
6: **add a random (normal distributed) phase wedge to** $P(\vec{\rho})$
$\hat{P}(\vec{\rho}) \leftarrow P(\vec{\rho}) + \text{phase wedge } \left(\mathcal{N}(\mu = \vec{0},\, \alpha_{\max}^2)\right)$
7: **simulate the diffraction pattern with the modified probe** $\hat{P}(\vec{\rho})$
$I_j(k) \leftarrow \left|\mathbf{FT}\left(O_\theta(\vec{\rho} - \Delta\vec{\rho}_j)\,\hat{P}(\vec{\rho})\right)\right|^2$
8: **return** $I_j\left(\vec{k}\right)$ and $\Delta\vec{\rho}_j$

The results for normal distributions with standard deviations corresponding to 1 to 5 detector pixel shift are shown in Fig. 6.10. Increasing variation in the incident beam angle creates radial stripes in the tomographic plane along the most prominent edges of the sample. Neither radial stripes were seen in the initial CPT nor a cloud-like background was observed in the 2D ptycho

reconstructions. Therefore, a change in beam direction was excluded as the main reason for the bad quality of the CPT reconstruction.

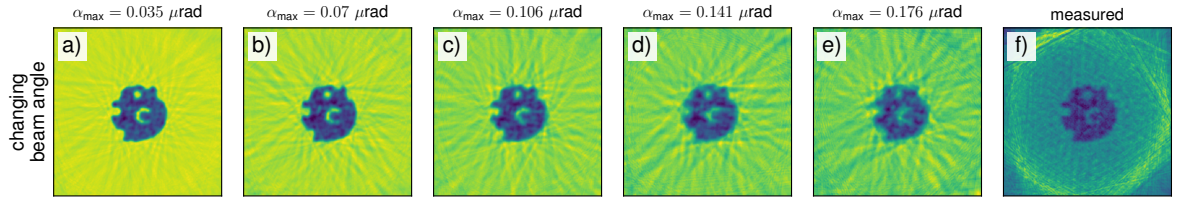

Figure 6.10: (a-e) simulation of the influnce of changing beam angle between exposures on the CPT reconstruction of an otherwise perfect dataset compared against (f) the CPT reconstruction of the real data set.

Incoherent background

When this experiment was performed, not the whole beam path between sample and detector could be evacuated. In fact about $30\,\mathrm{cm}$ just downstream the sample and $5\,\mathrm{cm}$ upstream of the detector of the beam path were through air. Although the effects are small, photons scattered on air molecules might have reached the detector and contributed to the measured diffraction patterns. As these photons are not included in the ptychographic model, this incoherent photon background can be problematic for the ePIE algorithm.

Algorithm 9 Simulation of a PXCT dataset with an incoherent background

1: **procedure** simulation incoherent background $(V(\vec{\rho}), P(\vec{\rho}), \Delta\vec{\rho}_j)$
2: **choose the strength** f_{incor} **of the incoherent background changes**
$f_{\text{incor}} \leftarrow 0.1^n; n \in [3, 2, 1]$
3: **for all** rotation angles Θ **do**
4: **calculate the projection** $O_\theta(\vec{\rho})$
5: **for all** measurement positions j under that angle Θ **do**
6: **simulate the diffraction pattern with the modified probe** $\hat{P}(\vec{\rho})$
$I_j(k) \leftarrow |\mathbf{FT}(O_\theta(\vec{\rho} - \Delta\vec{\rho}_j) P(\vec{\rho}))|^2$
7: **calculate the average diffraction pattern** $I_{\text{mean}}(k)$
$I_{\text{mean}}(k) \leftarrow \sum_j I_j(k) \cdot \left(\sum_j 1\right)^{-1}$
8: **for all** measurement positions j **do**
9: **replace the fraction** f_{incor} **of** $I_j(k)$ **with** $I_{\text{mean}}(k)$
$I_j(k) \leftarrow (1 - f_{\text{incor}}) \cdot I_j(k) + f_{\text{incor}} \cdot I_{\text{mean}}(k)$
10: **return** $I_j\left(\vec{k}\right)$ and $\Delta\vec{\rho}_j$

To simulate the effect of an incoherent background on the CPT reconstruction, I replaced a certain fraction of the simulated intensity in every diffraction pattern with the mean of all simulated diffraction patterns (see algorithm 9). Afterwards the CPT reconstructions were carried out as before. The results for $0.1\,\%$, $1\,\%$ and $10\,\%$ of incoherent background in the diffraction patterns are shown in Fig. 6.11.

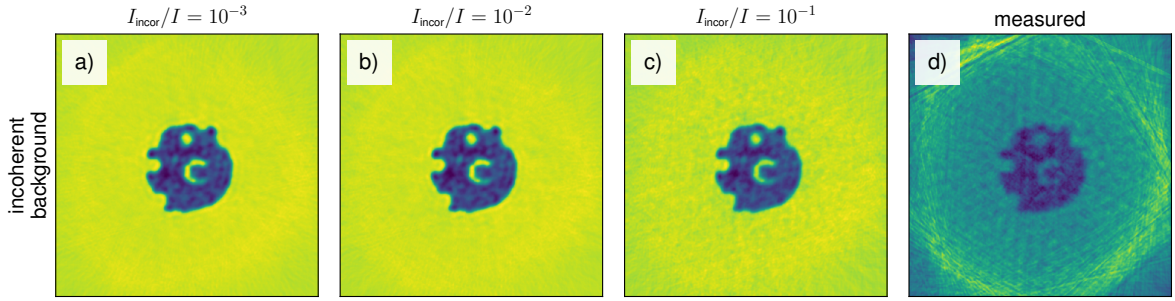

Figure 6.11: (a-c) simulation of the influence of an incoherent background of the measured diffraction pattern on the CPT reconstruction of an otherwise perfect data set compared against (d) the CPT reconstruction of the real data set.

Regarding the phase of the reconstruction, the CPT algorithm seems to be quite robust to an incoherent background. Increasing the fraction of incoherent intensity increases the graininess in the tomographic plane, but with much finer grains as observed in Fig. 6.8. As incoherent fractions above $10\,\%$ are unlikely, and the created artifacts do not match the observed ones, an incoherent background was excluded as the main reason for the bad quality of the CPT reconstruction.

Changing beam intensity

The beam intensity on the sample is known to change over time. Ideally, a transmission diode should be installed upstream of the sample to measure the incoming photon flux and normalize the diffraction patterns. Due to spatial restrictions in the experimental setup, the transmission diode could only be placed upstream the focusing optics. Consequently, small translational changes of the beam leading to intensity changes of the incident beam in the sample plane are not captured by this transmission diode.

To simulate the effect of a fluctuating beam intensity on the CPT reconstruction, each diffraction pattern's total intensity was reduced by a random factor between 1 and a lower limit (see algorithm 10). Afterwards the CPT reconstructions were carried out as before. The results for lower limits of $90\,\%$, $80\,\%$, $70\,\%$, $60\,\%$ and $50\,\%$ intensity reduction are shown in Fig. 6.12.

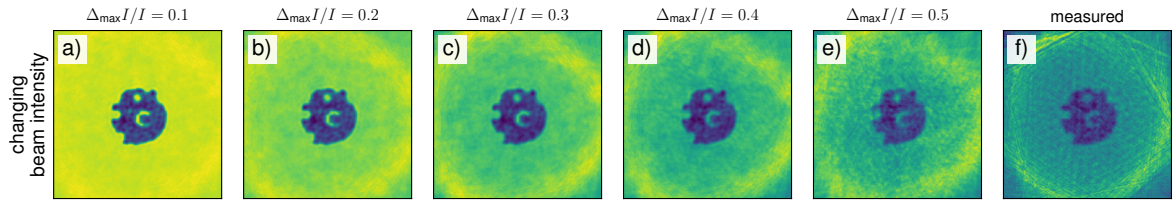

Figure 6.12: (a-e) simulation of the influence of changing beam intensity between exposures on the CPT reconstruction of an otherwise perfect data set compared against (f) the CPT reconstruction of the real data set.

The resulting artifacts resemble what was observed in Fig. 6.8: a bright halo around the

Algorithm 10 Simulation of a PXCT dataset with a changing beam intensity

procedure simulation changing beam intensity ($V(\vec{\rho}), P(\vec{\rho}), \Delta\vec{\rho}_j$)
  choose the strength f_{max} **of the intensity variations**
  $f_{\text{max}} \leftarrow n; n \in [0.1, \ldots, 0.5]$
  for all rotation angles Θ **do**
    calculate the projection $O_\theta(\vec{\rho})$
    for all measurement positions j under that angle Θ **do**
      simulate the diffraction pattern with the modified probe $\hat{P}(\vec{\rho})$
      $I_j(k) \leftarrow \left|\mathbf{FT}\left(O_\theta(\vec{\rho} - \Delta\vec{\rho}_j)\, P(\vec{\rho})\right)\right|^2$
  calculate the average diffraction pattern $I_{\text{mean}}(k)$
  $I_{\text{mean}}(k) \leftarrow \sum_j I_j(k) \cdot \left(\sum_j 1\right)^{-1}$
  for all measurement positions j **do**
    randomly choose a factor f **from the interval** $[0, f_{\text{max}}]$
    remove the fraction f **of** $I_j(k)$
    $I_j(k) \leftarrow (1 - f) \cdot I(k)$
  return $I_j\left(\vec{k}\right)$ and $\Delta\vec{\rho}_j$

zeolite particle emerges and the background becomes grainy. Even tough variations down to $50\,\%$ are rather extreme and do not reflect the actual amount in intensity variations of a few percent, the created artifacts match with the ones previously observed when reconstructing the experimental data. Therefor the change in beam intensity on the sample in combination with a missing normalization is the most promising candidate to explain the problems of the CPT reconstruction.

6.5.3 Second implementation

In the second implementation of the CPT algorithm, an extension known from the ePIE algorithm was applied in order to handle varying intensity of the incoming beam. The algorithm calculates the exit wavefront in the usual way from the estimated object $O(\vec{\rho})$ and the estimated probe $P(\vec{\rho})$:

$$\Psi_j(\vec{\rho}) \leftarrow O(\vec{\rho} - \Delta\vec{\rho}_j)\, P(\vec{\rho})\,. \tag{6.1}$$

Afterwards, the propagation to the far-field is still done using the Fourier transform:

$$\psi_j\left(\vec{k}\right) \leftarrow \mathcal{FT}\left[\Psi_j(\vec{\rho})\right]. \tag{6.2}$$

Different to the standard implementation of the ePIE algorithm, the brightness of the estimated $\psi_j\left(\vec{k}\right)$ diffraction pattern and the measured $\sqrt{I_j}\left(\vec{k}\right)$ are compared:

$$f_j = \frac{\int \sqrt{I_j}\left(\vec{k}\right)\left|\psi_j\left(\vec{k}\right)\right| \mathrm{d}\vec{k}}{\int \left|\psi_j\left(\vec{k}\right)\right|^2 \mathrm{d}\vec{k}}. \tag{6.3}$$

The factor f_j desribes how much brighter or darker $\psi_j\left(\vec{k}\right)$ would have to be, so that it matches the measured diffraction pattern [101]. This factor f_j is then used in the update step of the ePIE algorithm in the following way (compare with algorithm 1 step 10):

$$O\left(\vec{\rho}-\Delta\vec{\rho}_j\right) \leftarrow O\left(\vec{\rho}-\Delta\vec{\rho}_j\right) + \beta\frac{P_j^*\left(\vec{\rho}\right)}{\left|P_j\left(\vec{\rho}\right)\right|^2_{\max}}\left(\hat{\Psi}_j\left(\vec{\rho}\right) - f_j\cdot\Psi_j\left(\vec{\rho}\right)\right) \tag{6.4}$$

and

$$P\left(\vec{\rho}\right) \leftarrow P\left(\vec{\rho}\right) + \beta\frac{O_j^*\left(\vec{\rho}-\Delta\vec{\rho}_j\right)}{\left|O_j\left(\vec{\rho}-\Delta\vec{\rho}_j\right)\right|^2_{\max}}\left(\hat{\Psi}_j\left(\vec{\rho}\right) - f_j\cdot\Psi_j\left(\vec{\rho}\right)\right). \tag{6.5}$$

Scaling the estimated exit wavefront $\Psi_j\left(\vec{\rho}\right)$ by f_j deceives the algorithm into not having to correct for absolute brightness at this measurement position j, as the brightness of the simulated exit wavefront and the measured diffraction pattern already match.

Implementing the ePIE update step in this way makes the algorithm independent from the information about the total intensity at each scan position, which is exactly found source of error in the measured data set. Relative intensity variations in the illuminated area are still being reconstructed as the intensity of the exit wavefront was just scaled. As a ptychographic data set is recorded with considerable overlap in the illuminated areas, the relative absorption of the sample can still be reconstructed correctly to all but a scaling factor.

Using the improved update step inside the ePIE algorithm the data set was reconstructed again, both with the PXCT and the CPT algorithm. Slices through the resulting volumes are shown in Fig. 6.13. The quality of the CPT reconstruction improved altogether (compare to Fig. 6.13). The graininess in the background was drastically reduced as well as the vertical phase wedge through the volume. The reconstructed amplitude shows a cloud-like background, but by no means the strong stripe artifacts as before. The podium can be clearly identified. In the phase volume it is reconstructed even further down as in the PXCT reconstruction, where it is not covered by all projections due to mechanical shifts.

In conclusion, the changes to the ePIE update step improved the reconstruction quality of the CPT algorithm. As this algorithm was previously only tested on model data, the problem of missing normalization and its effects on the reconstruction result were heretofore unknown.

6.6 Resolution comparison

To compare the results of both reconstruction algorithms quantitatively, the achieved resolution of both algorithms was estimated using three methods:

- fitting the error function on multiple line profiles across edges
- calculating the Fourier shell correlation
- calculating the spatial signal to noise ratio

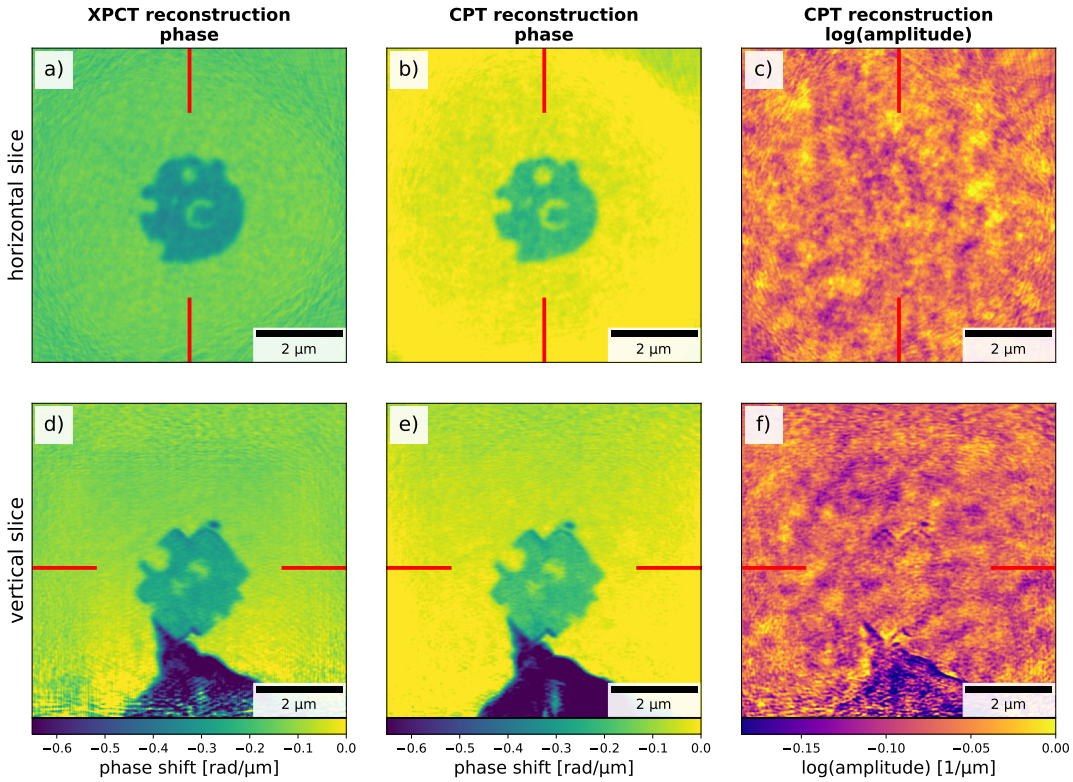

Figure 6.13: Slices though the PXCT reconstructed phase of the reduced data set (a and d) in comparison to the phase (b and e) and optical density (c and f) of the CPT reconstruction with the improved ePIE update step of the same data set.

6.6.1 Edge fits on line profiles

Multiple line profiles across edges in the two reconstructed volumes were extracted. The line profiles were chosen along the four major directions inside the tomographic plane. Each line profile was chosen in a position that allowed for at least 600 nm of air in one direction and 600 nm of sample material in the other direction, to allow for a proper baseline for the fitted error function at both ends.

The profiles were then fitted with an error function. From these fits, the edge widths were extracted as the distance between the 10 % and 90 % level of the edge. The widths for the PXCT reconstructed volume ranged between 139 nm and 183 nm, while the widths for the CPT reconstructed volume ranged between 123 nm and 148 nm (see Fig. 6.14). For all profiles, the width of the CPT reconstruction was at least 16.3 nm (approximately one pixel) smaller than the one for the PXCT reconstruction.

6.6.2 Fourier shell correlation

To not only evaluate local resolution, the averaged global resolution was also estimated using Fourier shell correlation. Therefore, the data set was split into two complementary halves, by assigning for each projection the diffraction patterns alternately to one or the other half. Both halves were then reconstructed once using the PXCT algorithm and once using the CPT

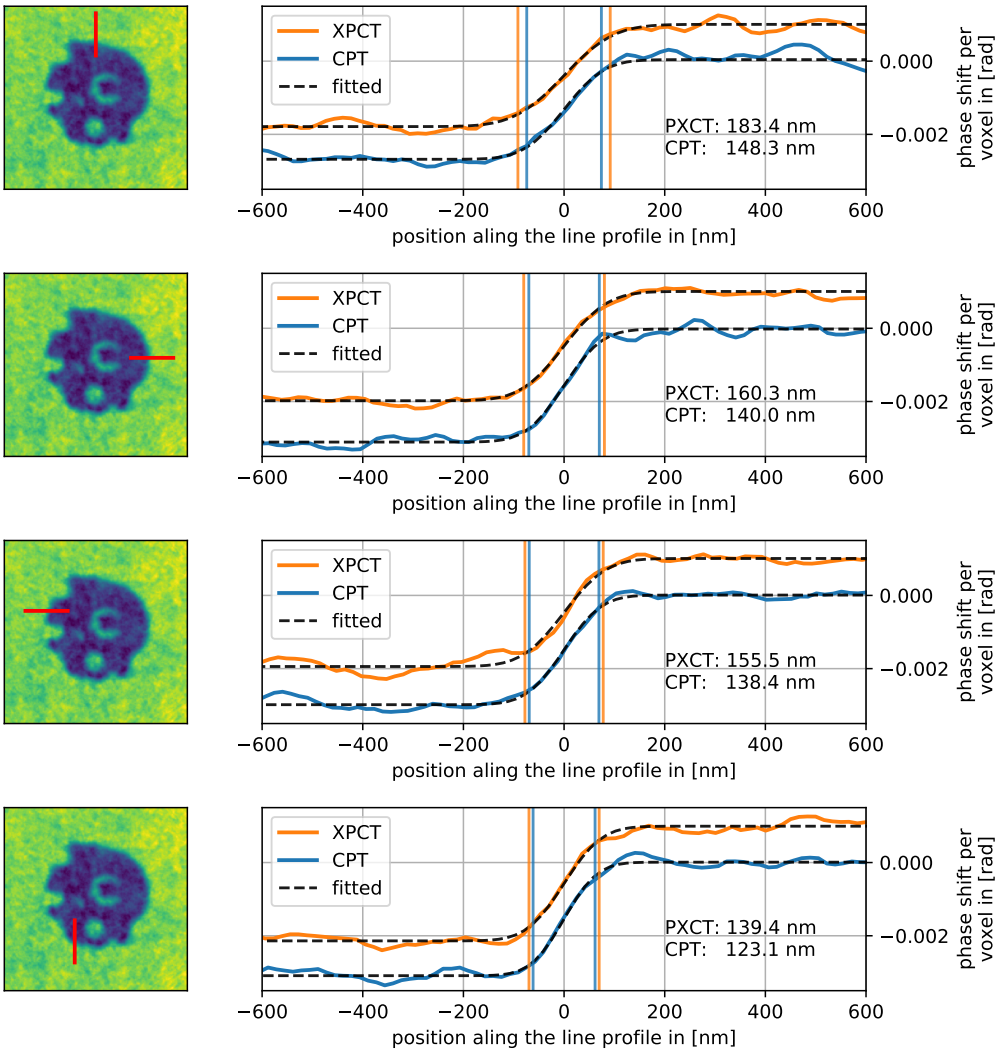

Figure 6.14: Fitting of line profiles across four edges in the PXCT and CPT reconstructions of the macroporous zeolite particle. Left: reconstructed slice (in the CPT reconstruction) with the position of the lines; Right: line profiles for the PXCT and CPT reconstructions together with respective error-function fits. The width of the edge is determined as the interval between the 10% and 90% level of the fits. In all cases the CPT reconstruction has a slightly sharper edge profile.

algorithm.

The two volumes from the PXCT reconstructions and the two volumes from the CPT reconstructions then served as input to calculate the Fourier shell correlations. As halved were used, the half-bit threshhold criterion was used to estimate the achieved resolution [64]. For the PXCT reconstructions a resolution of $72.5\,\mathrm{nm}$ was estimated, while the estimated resolution for the CPT reconstructions was $65.3\,\mathrm{nm}$ (see Fig. 6.15).

Separating the dataset into two halves effectively increased the scanning step size by a factor of 1.41 and reduces the overlap between neighboring probes. But as the original step size of $400\,\mathrm{nm}$ is conservative for a beam size of $1800\,\mathrm{nm}$, this increase in step size should not have affacted the ability of the ePIE algorithm to recosntruct each projection.

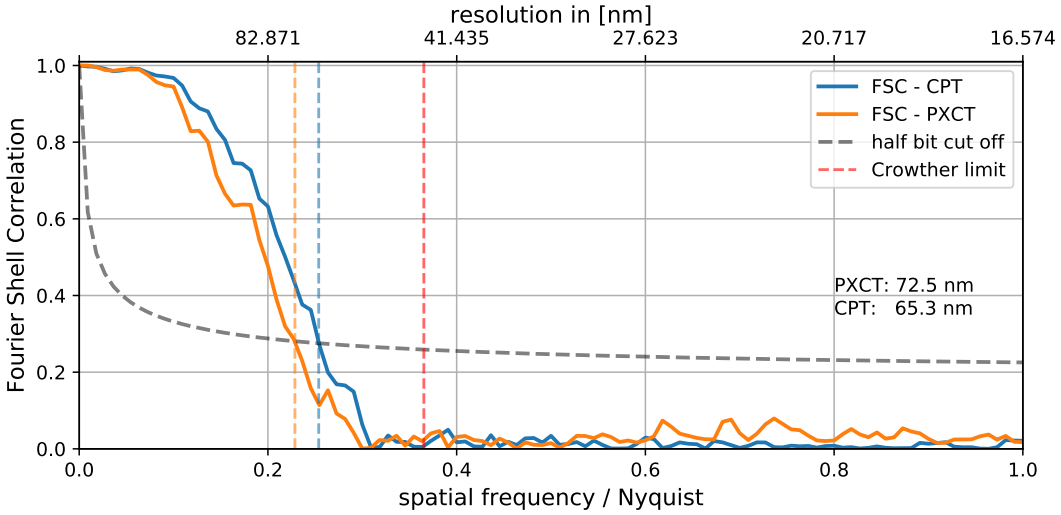

Figure 6.15: Resolution estimation by FSC for the PXCT reconstructions and the CPT reconstructions.

6.6.3 Spatial signal to noise

Using the Fourier shell correlations calculated above, the spatial signal to noise ratios [65] were calculated as:

$$SSNR\,(k) = 2\,\frac{FSC\,(k)}{1 - FSC\,(k)} \tag{6.6}$$

Using $SSNR = 1$ as the threshold criteria, where the noise outweighs the signal, a resolution of $76.5\,\mathrm{nm}$ for the PXCT reconstructions and a resolution of $66.9\,\mathrm{nm}$ for the CPT reconstructions were estimated (see Fig. 6.16). The threshold of $SSNR = 1$ corresponds to a threshold for the Fourier ring correlation of $FRC = 1/3$, which is the limit of the one-bit criteria. D the spectral signal to noise ratio (SSNR) is a more stringent criteria than the half-bit criteria used with the FSC and results in a slightly worse resolution.

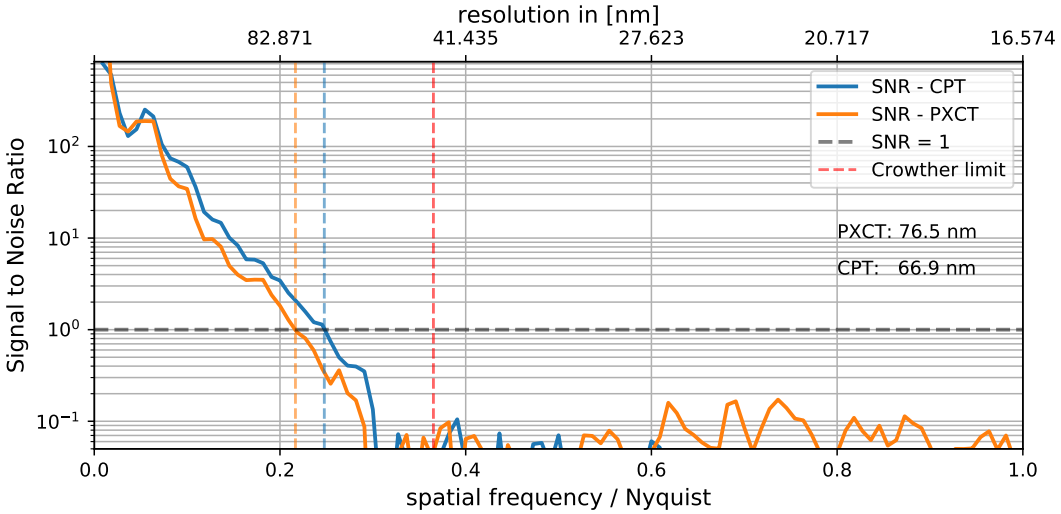

Figure 6.16: Resolution estimation by SSNR for the PXCT reconstruction and the CPT reconstruction.

Although the absolute values for the achieved resolution differ from method to method, the

volumes reconstructed using the CPT algorithm result in the better resolution is all cases. The average improvement is approximately the edge length of one pixel / voxel. This might be the result of the inherent self-alignment during the CPT iterations, as the algorithm strives for tomographic consistency over all projection angles.

6.7 Reduced sampling

For model data it was shown in [91] that the overlap needed for a successful ptychographic reconstruction can be reduced when performing a CPT reconstruction, as the overlap is given in the tomographic plane. This was verified by removing diffraction patterns from the data set and running the same CPT reconstruction as before. Fig. 6.17 shows the reconstructions if only every n-th diffraction pattern ($n = 1, \ldots, 5$) in the horizontal direction is used for the CPT reconstruction.

Even in the case of only using every fifth diffraction pattern in the horizontal direction, and no longer having overlap between neighboring probing beams in the horizontal, the zeolite particle is still reconstructed. With the reduction of the number of diffraction patterns used, the reconstructions become more and more noisy. This is directly related to the effectively reduced dose applied to obtain the tomogram.

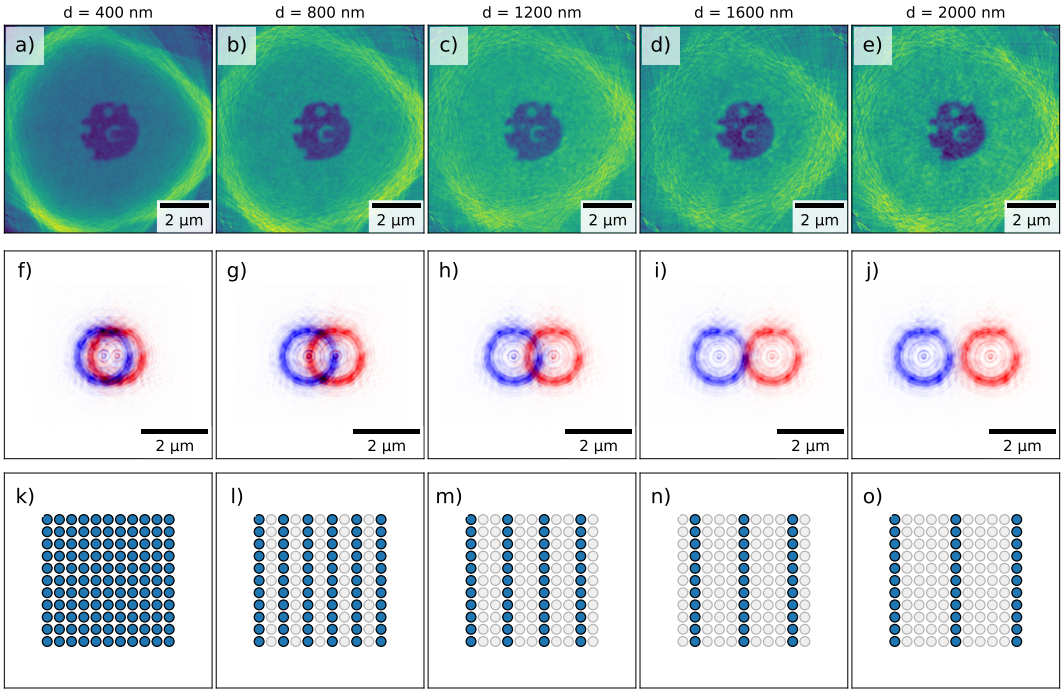

Figure 6.17: Reconstructions of the dataset using $N = 100$ iterations of the CPT algorithm. a) to e) show the result when only using every nth diffraction pattern in the horizontal direction ($n = 1, \ldots, 5$), effectively increasing the horizontal step size from $400\,\mathrm{nm}$ to $2000\,\mathrm{nm}$. f) to j) show the overlap of the probing beam intensities of two neighboring horizontal positions for each case. k) to o) show the positions of the used (blue) and discarded (gray) diffraction patterns inside the 11×11 scan grid.

Increasing the horizontal step size, decreases the time needed to record a single projec-

tion. Applying this measurement scheme, allows to record projections at more angles in the same amount of time, effectively allowing for achieving higher resolutions due to the decreased Crowther limit. Increasing the horizontal step size beyond the point of overlap between neighboring probes would impose the usage of the CPT algorithm, as the single projections could no longer be reconstructed on their own using the ePIE algorithm.

The sampling in the vertical direction still has to be choosen according to the overlap constrains discussed in chapter 5, because loosing the vertical overlap cannot be substituted with overlap between different projections in the tomographic plane.

6.8 Conclusion

It was shown that the recorded data set could be reconstructed using both the conventional PXCT algorithm as well as the new CPT algorithm. To our knowledge, the later was the first ever application of the CPT (as presented in [91]) to experimental data, and even tough the data set had to be reduced to accomplish a reconstruction in a reasonable time, the CPT has proven that it improves the reconstruction compared to the conventional method. Moreover the ability to still reconstruct a sparse data set, which would have the conventional method fail, was confirmed.

For this first tests of the new method, the alignment of the initial PXCT reconstruction was necessary to even start the CPT reconstruction. This might be avoided with improved mechanical accuracy and stability of the scanning stages in the future. The time needed to reconstruct even the reduced data set was about seven days, which has to be improved for future experiments. In a fraction of the time needed for the CPT reconstruction, the inital PXCT reconstruction was performed on a complete data set with multiple extra-features in the ePIE algorithm. Future implementations require optimized code and sufficient hardware in order to cope with the large amount of data. The PXCT reconstruction was performed using highly optimized code run on multiple GPUs in parallel, while the code for the CPT was the first ever running implementation of this algorithm using experimental data and being run on a single multi-core CPU. Multiple aspects of the algorithm could be adapted for parallel computing, such as solving of the two-dimensional ptychographical problem or the iteration over all projection angles. Even with this first, non-optimized implementation of the CPT algorithm, the reconstruction of 290 million (660^3) complex variables was done within seven days on a single computer utilizing only CPUs.

Independent of the reconstruction algorithm chosen, the reconstructed volume were evaluated qualitatively and quantitatively. Voxel values could be used to distinguish sample from sample holder and were in good agreement with the literature values. The inner macro-pore structure of the hierarchical zeolite particle was resolved and can be further analyzed.

Chapter 7

InN/GaN micro rod

The next experiment will not focus on the possibility of a coupled ptychographic tomographic reconstruction but will only use the conventional ptychographic X-ray computed tomography (PXCT) method and the possibility of elemental contrast and simultaneous multi-modal measurements.

7.1 Motivation of the experiment

Core-shell structured micro-rods increase the active surface area dramatically compared to planar systems. This is advantageous for optoelectronic or sensory applications such as LEDs or solar cells, just to name a few. The shell of these micro-rods is often layered, while the thickness and exact composition of these layers strongly influence the overall performance.

The micro-rods presented in this chapter are made from InGaN/GaN layers and have been observed to show a red shift of the emitted light along the rods vertical axis while performing spatially resolved cathodoluminescence (CL) measurements using an scanning electron microscopy (SEM) [102]. This would have a negative impact if the micro-rods were to be used as a light emitting element, as they would not emit the same wavelength over their whole surface, but also in the inverse use-case as optical sensors, as the sensitivity for certain incoming wavelengths is varying over the surface. The reason for this spatial differences in red shift could be a thickness and/or a concentration gradient in the center shell of the micro-rod. The micro-rods measure $\approx 2\,\mu\mathrm{m}$ in diameter and several micro-meter in height, making them unsuitable samples for transmission electron microscopy (TEM) measurements as a whole. As the layer of interest, the first shell covering the core, is again covered by a second layer, surface sensitive methods such as using an SEM are also unfit to determine the first layers thickness and composition. Milling open the micro-rods using a focused ion-beam (FIB) can reveal the first layer, but as the sample is mostly made from Ga itself the Ga ion beam would most likely contaminate the cut surface. Moreover it is a destructive technique making subsequent experiments requiring an unaltered sample impossible. Indirect non-destructive methods such as measuring the exact position of Bragg peaks or measuring reflectivity rocking curves can be used to estimate the

composition of the interesting shell(s) at each facet [102]. But these methods always average over illuminated volume and are therefore limited to the size of the used probing beam.

Ptychographic X-ray computed tomography (PXCT) allows to measure the layer thickness directly without destroying the sample and with an resolution surpassing the size of the probing beam. Performing multiple PXCT measurements at different photon beam energies near an absorption edge also allows conclusions on the samples elemental or even chemical composition [103]. The simultaneous usage of an X-ray fluorescence (XRF) detector provides an additional channel of information on the samples elemental composition without prolonging the measurement duration.

7.2 Sample preparation

The samples used in the presented experiment were grown by Jana Hartman at the Technische Universität Braunschweig. The micro-rods presented in this work consists of:

- a n-doped GaN core
- three very thin ($\leq 10\,\mathrm{nm}$) GaN layers acting as spacer and quantum barrier (QB)
- a thick layer of a mixture of InN and GaN (normally acting as quantum well (QW))
- three very thin GaN layers acting as spacer and QB
- three layers of p-doped GaN (doping increases from the center of the rod to the outside)

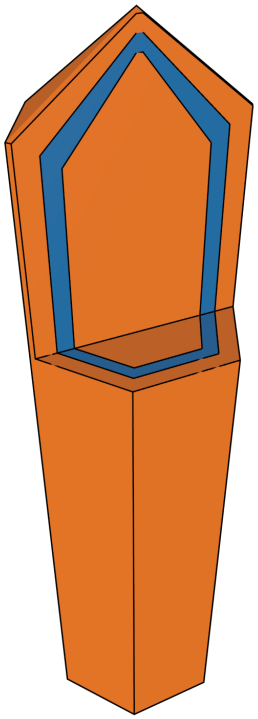

Figure 7.1: Schematic representation of GaN (orange) and InN/GaN (blue) in the micro-rod sample.

As the doping of the GaN core and the outer most GaN layers is well below one atom in thousand, it can not be resolved by PXCT. Therefor the core, the spacer, the quantum barriers and the outer most layers will all look like pure GaN and the sample will appear to have three distinctive features: the core, the first shell containing the InN and GaN mixture and the outermost shell (see Fig. 7.1). The interesting layer is the first shell made from In/GaN as it determines the wires opto-electronic properties. Since this experiment serves as a demonstration, we prolonged the growth time sixfold, to have a thicker In/GaN layer and a better contrast. The exact resulting thickness and the exact ratio of InN to GaN are unknown and are the subject of this experiment.

As many of these rods are grown on a flat substrate next to each other, it was necessary to extract a single one without destroying or contaminating it prior to the PXCT experiment. A FIB was used to mill out a single micro-rod and to mount it on top of a sample pin. As the micro-rod and the FIB both consists of (mostly) Ga atomes / ions, there is a danger of contaminating the

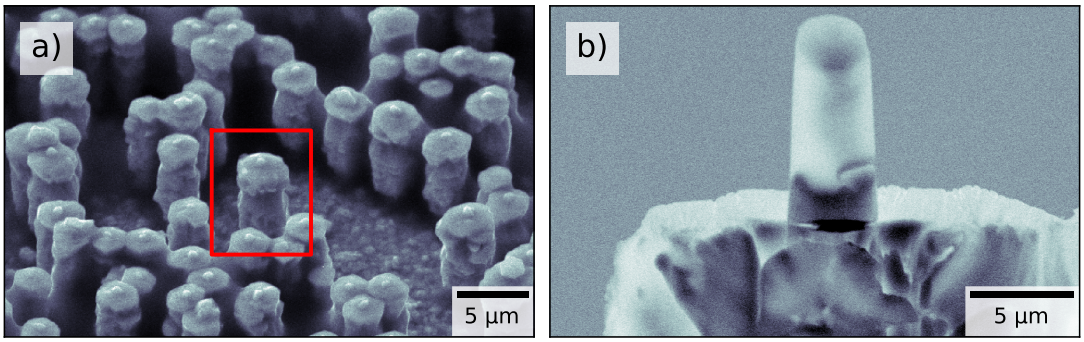

Figure 7.2: SEM images of the glue covered forest of micro-rods (a) and the final prepared sample inside the cylinder of glue on top of the Ti sample pin (b).

micro-rod with residue Ga ions from the FIB. To this end the forest of micro-rods was covered with an organic glue prior to the FIB milling (see Fig. 7.2a). This way scattered rogue Ga ions are caught in the glue before reaching the actual micro rod. The milled out glue-covered micro-rod was placed on top of a Ti sample pin. Afterwards the milled surfaces were cleaned using the FIB operating at a very low current. The preparation of the sample were carried out by Michael Niehle at the Paul-Drude-Institut für Festkörperelektronik in Berlin. The finally prepared sample is shown in Fig. 7.2b.

7.3 Measurement

As in the previous chapter the experiment was performed at the hard X-ray nanoprobe end-station of beamline P06 of the PETRA III synchrotron radiation source (Hamburg, Germany). The indium content and the thickness of the first shell are the subjects of the experiment it is best to perform resonant PXCT measurements across one absorption edge of indium. But this was not an option, as the absorption edges of indium are situated around $\approx 3.9\,\mathrm{keV}$ and $\approx 27.9\,\mathrm{keV}$. The lower energies are not feasible, as the strong absorption and scattering in air for X-rays below $5\,\mathrm{keV}$ makes it necessary to place the complete experimental setup in-vacuum. The high energies around $\approx 27.9\,\mathrm{keV}$ are also unsuitable as the total amount of usable coherent photon flux would be reduced enormously. Additionally the quantum efficiency in the detector would be reduced, while the scattering inside the detector module would drastically increase.

Therefore it was decided to instead perform the PXCT measurements around the Ga-K edge ($10.367\,\mathrm{keV}$). The measured refractive index of Ga will be affected most by measurements around this edge. Everything not changing (as much) must be something else. And as the only other measurable element inside the micro-rod is In, the concentration of InN/GaN should be measurable in this way. Measuring on ($10.37\,\mathrm{keV}$) and above ($10.47\,\mathrm{keV}$) the absorption edge allows to use the recorded Ga–XRF maps as an indicator for the sample alignment in the field of view (FOV). Measuring below the edge was waived to maximize the number of recorded angles at the other two energies.

The sample on its titanium holder was placed inside the Ptychographic nano-analytical mi-

croscope at PETRA III (PtyNAMi) [41]. A double crystal monochromator (DCM) (Si-111) in combination with a pair of mirrors was used to monochromatize the X-ray beam. A pair of horizontal and vertical nano-focussing lens sets was used to focus the X-ray beam on the sample. This time the sample was placed in the focus ($173\,\mathrm{nm}$ horizontal full width at half maximum (FWHM) and $189\,\mathrm{nm}$ vertical at $10.47\,\mathrm{keV}$) of these lenses to have the smallest possible beam profile for the intended XRF measurements. The photon counting pixel detector (EIGER X 4M, DECTRIS, Switzerland) was placed $2.12\,\mathrm{m}$ downstream the sample. The silicon-drift detector (Vortex-EM, HITACHI High-Technologies Science [104]) for measuring the XRF signal was placed in about $10\,\mathrm{mm}$ distance from the sample perpendicular to the beam axis. The placement in direction of the polarization of the X-ray beam is not a coincidence, but was chosen to reduce the amount of in-elastically scattered photons recorded by the XRF detector. Once more an interferometer based tracking system was used to measure the sample positions during the experiment. A scheme of the experimental setup is shown in Fig. 7.3.

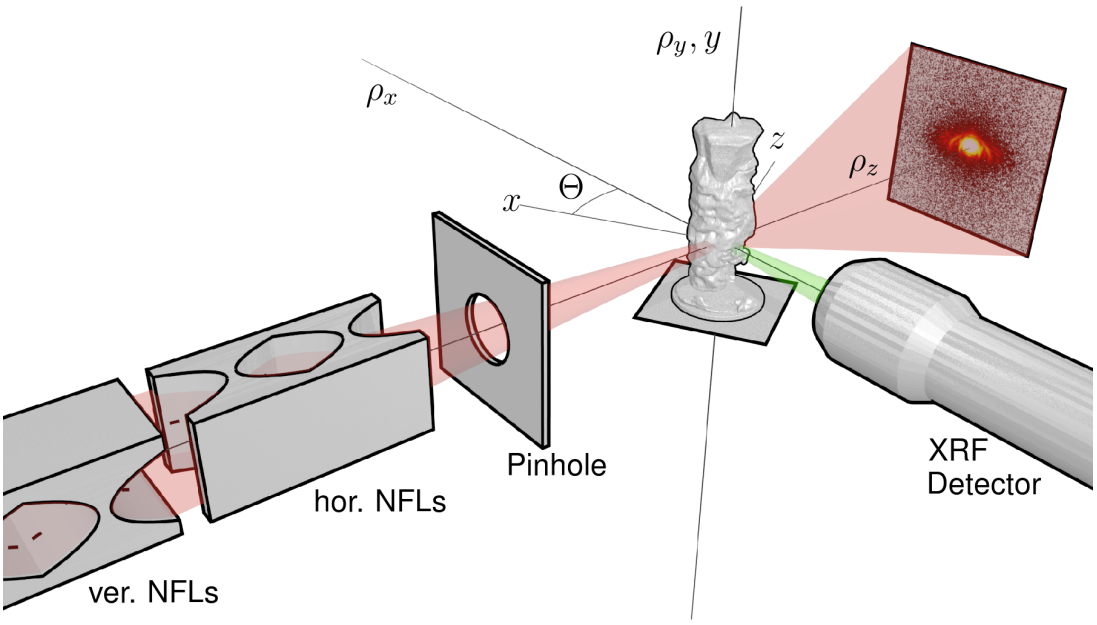

Figure 7.3: Scheme of the experimental setup used to measure the micro-rod sample. A probing beam (red) is focused by two sets of nano-focusing lenses. A pinhole is used to clean up the beam before it hits the sample placed in the focus of the lenses. The photon counting pixel detector is placed downstream behind the sample to record the diffraction patterns for ptychography while the silicon drift detector for XRF is placed perpendicular to the beam in the polarization plane of the X-ray beam.

The first data set was recorded at $10.37\,\mathrm{keV}$. Again two opposing projections were recorded to estimate the achievable resolution via Fourier ring correlation (FRC). The resulting resolution of $\approx 40\,\mathrm{nm}$ and the sample diameter of $\approx 4\,\mu\mathrm{m}$ (with glue) would require 160 unique angles to be recorded according to the Crowther limit. To allow for some improvement in overall resolution with more sophisticated reconstruction parameters it was decided to record 180 projection angles at both energies. To cover the whole sample and some air to the left, right and top of the sample a FOV of $6\,\mu\mathrm{m}$ (horizontal)$\times 9.6\,\mu\mathrm{m}$ (vertical) was chosen. As the overlap-requirement for neighboring positions had to be fulfilled in order to be able to reconstruct the ptychographic

data, small scanning steps of $50\,\mathrm{nm}$ were made in both scanning directions, resulting in $23\,353$ scanning positions and therefor diffraction patterns per angle.

To record 180 projections at two energies with $23\,353$ diffraction patterns each in four days required very short exposure times. Measuring in the usual ‚move, stop, settle, expose and repeat' scheme utilized in the previous experiment would create too much overhead. Therefor a continuous measurement scheme was used: The motor scanning the sample in the vertical direction was not stopped for each exposure, but instead was driven continuously while the diffraction patterns of one line were recored. This reduced the overhead dramatically and allowed to use exposure times of $20\,\mathrm{ms}$.

Once the PXCT data set at $10.37\,\mathrm{keV}$ was recorded, the photon energy was changed to $10.47\,\mathrm{keV}$ and the experiment was repeated with neither entering the experimental hutch nor interfering with the sample in between measurements. Overall $\approx 80\,\mathrm{h}$ were needed to record both data sets with $181 \times 23\,353 = 4\,226\,893$ diffraction patterns and as many XRF spectra each. All measurement parameters are summarized in table 7.1.

Table 7.1: Experimental parameters of the PXCT measurement done on the InGaN micro rod, which started on the 26th of October in 2016.

Parameter	
scan area ($h \times v$)	$6\,\mu\mathrm{m} \times 9.6\,\mu\mathrm{m}$
dwell time per scan point	$20\,\mathrm{ms}$
number of points ($h \times v$)	$193 \times 121 = 23\,353$
step size	$50\,\mathrm{nm}$
angular step size	$1°$
angular steps	181
angular range	$180°$
photon energies	$10.37\,\mathrm{keV}$ & $10.47\,\mathrm{keV}$
beam size (FWHM $h \times v$) at $10.37\,\mathrm{keV}$	$135\,\mathrm{nm} \times 168\,\mathrm{nm}$
beam size (FWHM $h \times v$) at $10.47\,\mathrm{keV}$	$175\,\mathrm{nm} \times 184\,\mathrm{nm}$
photon flux	$2.9 \cdot 10^7$ photons/s
sample-detector distance	$2.12\,\mathrm{m}$
detector pixel size	$75\,\mu\mathrm{m}$
overall measurement duration	$2 \times 40\,\mathrm{h}$

7.4 Ptychographic reconstructions

Four million diffraction patterns per data set are too much for a coupled ptychographic tomography (CPT) reconstruction using the current implementation of algorithm 5. To deal with this amount of data each projection was reconstructed on its own. The ptychographic reconstruction were done using the graphics processing unit (GPU)-optimized software *ptycho* utilizing the extended ptychographical iterative engine (ePIE) algorithm (see algorithm 1). All diffraction

patterns were cropped to a size of 256×256 pixel, resulting in a pixel size of $13.20\,\mathrm{nm}$ for the measurements done at $10.37\,\mathrm{keV}$ and $13.07\,\mathrm{nm}$ for the measurements done at $10.47\,\mathrm{keV}$. As described in 6.4.1 the software *ptycho* has multiple extra-features on top of the basic ePIE algorithm. For the reconstruction of each projection, only the (brute force) position correction was used to refine the scan positions $\Delta\vec{\rho}_j$. Using the other features described in 6.4.1 was waived as it would have increased the computational effort enormously. The position correction was used because of the used fly-scanning scheme and small probe size, making exact positions even more important for a successful reconstruction. Running 500 iterations took an average of $96\,\mathrm{min}$ for the reconstruction of a single projection. In total $580\,\mathrm{h}$ of GPU compute time were needed to reconstruct all projections recorded at both photon energies.

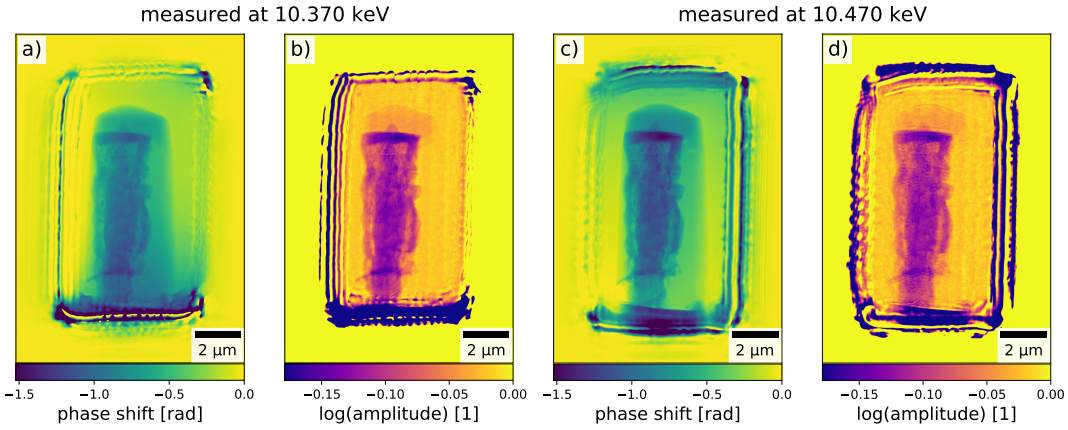

Figure 7.4: Two dimensional ptychographic reconstructions of the sample recorded under the same projection angle $\Theta = 0$ and at two different photon beam energies: (a and b) recorded at $10.37\,\mathrm{keV}$; (c and d) recorded at $10.47\,\mathrm{keV}$.

The reconstructed projections of the sample at $\Theta = 0°$ are shown in Fig. 7.4. The intensity profile of the corresponding reconstructed probing wave fields are shown in Fig. 7.5. It can be seen that the beam size changed entirely when the photon energy was changed. And it changed differently in the horizontal and vertical direction. This is expected and the reason is the usage of a pair of horizontally and vertically focusing nano focusing lenses (NFLs). As the two lens sets have to be placed in different distances from the sample, their focal lengths also have to account for that. When changing the photon beam energy their focal lengths change. And they change differently for each NFLs. The beam caustics and the position of the sample along the beam axis for both measurements are shown in Fig. 7.6. It shows how the sample is at the focus position for the measurement at $10.37\,\mathrm{keV}$ but slightly upstream of the focus for the measurement at $10.47\,\mathrm{keV}$ as the focal length of both lens sets has slightly increased. Important is that in both cases the beam size is larger than the step size in both directions, allowing for sufficient overlap and therefore redundancy in the ptychographic data sets for a successful reconstruction.

Comparing the reconstructed probes for measurements at the same energy but different projection angles Θ revealed that the beam shape did not change over the duration of one PXCT measurement at one photon energy. The 181 reconstructed probing wave fields $P_\Theta(\vec{\rho})$ differ

merely in a global lateral shift, which is an inherent freedom of the ePIE algorithm (especially with small probes). Therefor the data sets itself would qualify for a CPT reconstruction using only one shared probe for all projection angles. But as already discussed, the size of these data sets renders this possibility currently unfeasible due to the enormous computational effort.

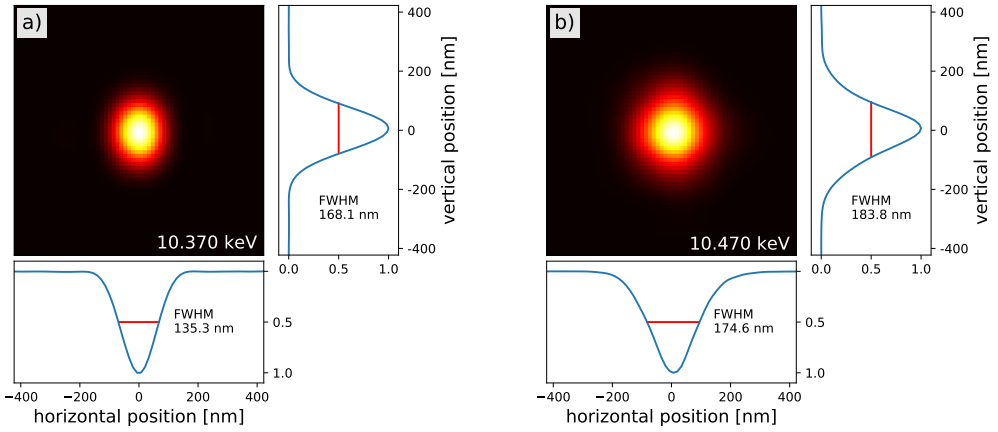

Figure 7.5: Reconstructed beam intensity profiles at the sample position and extracted beam widths for both recorded photon energies: (a) beam profile at $10.37\,\mathrm{keV}$; (b) beam profile at $10.47\,\mathrm{keV}$

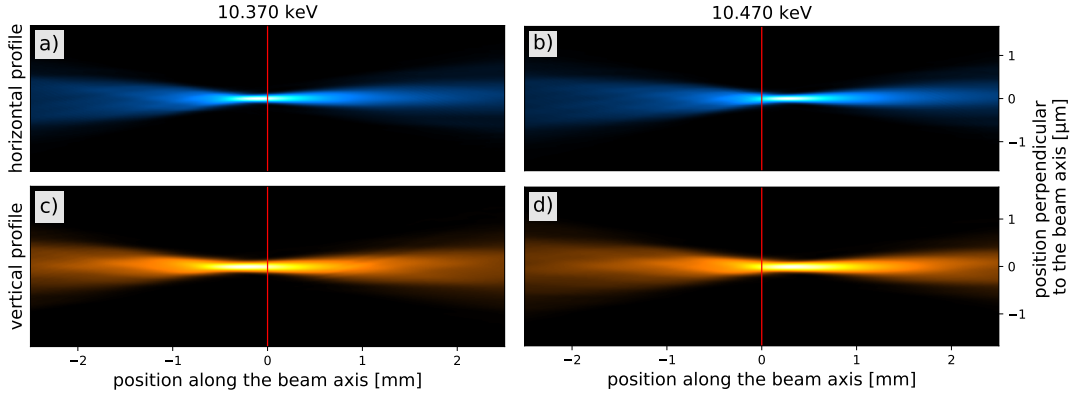

Figure 7.6: Propagated beam profiles along the optical axes for both recorded photon energies: (a and c): horizontal and vertical beam profile at $10.37\,\mathrm{keV}$; (b and d): horizontal and vertical beam profile at $10.47\,\mathrm{keV}$. Brighter colors indicate a higher beam intensity. The red lines indicate the position of the sample along the beam axis during the measurement of the PXCT data sets.

7.5 XRF fitting and map creation

X-ray fluorescence is the emission of characteristic secondary X-rays from excited atoms [105, 106]. In this case, the probing X-ray beam excites atoms inside the illuminated volume by expelling electrons from the inner orbitals. Electrons falling down from higher orbitals have to emit the energy difference between the orbitals as electromagnetic radiation in an arbitrary direction. As the energy levels of the atoms are element specific, the energy of the emitted photons is also element specific and also allows to draw conclusions on which orbitals the

electrons jumped. By measuring the spectrum of the XRF photons emitted by the sample, these specific energies can be assigned elements present in the sample. Here, I am using the Siegbahn notation for the characteristic photon energies. The latin letters K and L of the line denotes to which level the electron fell down to, while the Greek indices α and β differente the strongest and second strongest XRF line of each element.

The elemental information hidden inside the simultaneously measured XRF spectra has to be made into projection images as well before a tomographic reconstruction can be performed. The first step for doing this is to fit the peaks of the expected elements in all recorded spectra. To this end I first added up all recorded spectra measured at the same incident beam energy, resulting in one sum spectrum for the measurement at $10.37\,\mathrm{keV}$ and one sum spectrum for the measurement at $10.47\,\mathrm{keV}$. I then used the characteristic peaks in those spectra to calibrate the channels of the recorded spectra to actual photon energies using a quadratic fit:

$$E_{\text{photon}} = A + B * x_{\text{channel}} + C * x^2_{\text{channel}} \tag{7.1}$$

Both sum spectra resulted in the same fitting parameters ($A = -1.42 \cdot 10^{-2}, B = 9.77 \cdot 10^{-3}, C = 1.84 \cdot 10^{-8}$). Henceforth the energy calibration was trusted and used for the upcoming XRF fitting. As all measured spectra should be treated exactly the same way, I created and tested a config file for the software *pymca* [107] using the two sum spectra. This config file fitted the following XRF lines:

Ga	K_α, K_β, L_1	Si	K_α, K_β
In	L	V	K_α, K_β
Ar	K_α, K_β	Ni	K_α
Ti	K_α, K_β	C	K_α
Cr	K_α, K_β	Zn	K_α
Fe	K_α, K_β	W	L_3

These fitting-parameters where then used for all recorded spectra measured at both incident beam energies, resulting in fit coefficients for each fitted element at each measured position. These fitted coefficients are linear to the absolute number of atoms of the specific element, just with an unknown scaling factor. To quantify these fitted coefficients, one would have to measure calibrated reference foils as well to obtain these scaling factors. This was not needed in this experiment, as only the relative concentration of InN to GaN was investigated. Hence noe reference foils were measured.

Now that the relative quantity of each specific element at each exposure position is known, this information needs to be made into projection images. As the scanning pattern was a grid, it would be the easiest to create a pixel map with each pixel being a single exposure and the pixel size being the step size of the scanning grid. The previous ptychographic reconstruction of each projection allows to do something even better. The used refined ePIE algorithm refined the measurement position, as well as reconstructed the probing wave field on a much finer grid as the used scanning step size.

Therefor another approach was chosen: For every projection angle I started with an empty pixel map with the same extent and pixel size as the ptychographically reconstructed object. Using the refined positions from the ePIE algorithm and the center of mass of the reconstructed probing wave field, I placed each fitted XRF coefficient (see Fig. 7.7a) exactly where the beam hit the sample at this exposure (see Fig. 7.7c). After placing the 23 353 fitted XRF coefficients on the projection map, I interpolated the empty pixels in between linearly. All pixels outside the convex hull of the measured positions where set to zero (see Fig. 7.7d). This was repeated for every fitted element at every projection angle Θ for both measurements at the two incident photon energies. Due to the very short exposure times, there is a significant amount of noise on these maps. Therefore I convoluted each map with a Gaussian kernel of $13\,\mathrm{nm}$ FWHM (approx. one pixel) to smooth all maps a bit without reducing the resolution too much. A schematic overview of the whole process is shown in Fig. 7.7.

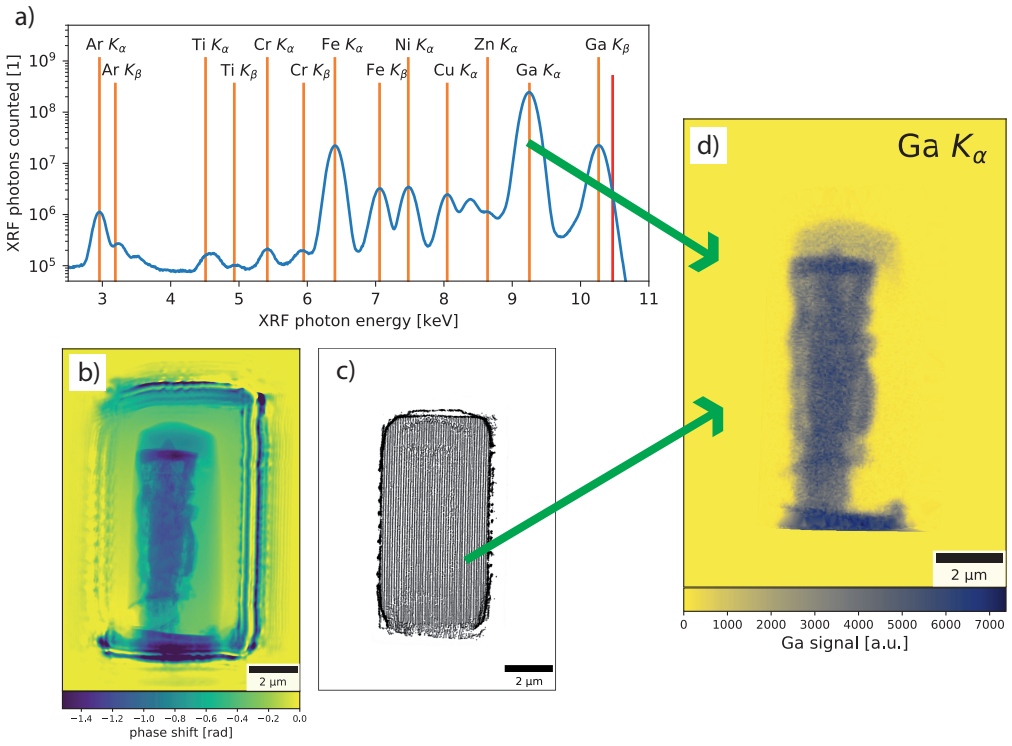

Figure 7.7: Workflow for the creation of the XRF maps: (a) fitting of all measured XRF spectra using *pymca*; (b) using the ptychographic reconstructions pixel grid and (c) its refined positions to create the XRF map (d)

The resulting XRF maps inherently align perfectly with their respective ptychographic reconstructions. Henceforth, all alignment steps can be done using the ptychographic reconstructions and the resulting shifts can be applied to all XRF maps respectively.

7.6 Alignment of projections

Before the tomographic reconstructions could be performed, all projections had to be aligned to another. For the data set recorded at $10.37\,\mathrm{keV}$ this was done the same way as already explained

in 6.4.2. The phase images of the ptychographically reconstructed objects were cropped to the FOV of the beam, which turned out to be more difficult as in 6.4.2. Because the measurements where done with a smaller probe size, the total amount of reconstructed air to the side and top of the sample is significantly smaller. Therefor more care had to be taken to not crop into the object itself, as this would create artifacts in the tomographic reconstruction (in the literature this is known as the problem of *truncated* sinograms [86, 108]). Additionally the motor used for scanning the sample through the beam had shown mechanical errors. Every time it stepped in the vertical direction, the movement was not only vertical, but also slightly horizontal. This parasitic movement was present in all recorded projections and resulted in the FOV resembling a parallelogram which defining angle changed depending on the rotation angle Θ of the sample. Luckily the sample positions were measured by an independent interferometric system. Nonetheless the edges of the FOV are tilted for most angles, making part of the FOV not usable for a tomographic reconstruction.

The resulting cropped phase images were then freed of phase wedges and offsets by taking the air to the left, right and top of the sample as a zero-reference. Afterwards the actual alignment was done as in 6.4.2: vertical alignment using the derivative of the horizontal integrals and horizontal alignment using the center of mass of the vertical integrals were alternated until a stable solution was found (see Fig. 7.8). The resulting total shifts were then applied to the logarithm of the amplitude images, as well as to all XRF maps from measurements at the same energy.

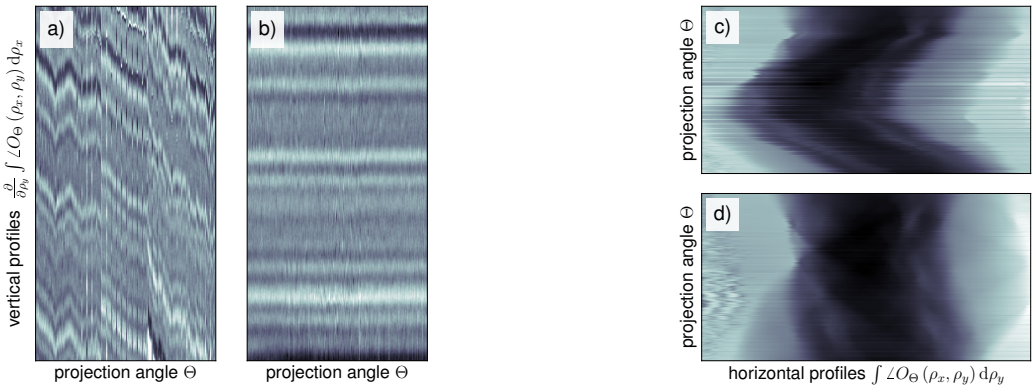

Figure 7.8: Exemplary alignment of the 2D ptychographic reconstruction of the data set measured at $10.370\,\mathrm{keV}$. Left: unaligned (a) and aligned (b) vertical profiles of all recorded projections; Right: unaligned (c) and aligned (d) horizontal profiles of all recorded projections

The ptychographically reconstructed phase images of measurements at $10.47\,\mathrm{keV}$ were interpolated to the pixel size of the maps measured at $10.37\,\mathrm{keV}$. Then they were cropped and freed from phase wedges and offsets as well. Afterwards each phase projection recorded at $10.47\,\mathrm{keV}$ was aligned using the corresponding projection from the same angle measured at $10.37\,\mathrm{keV}$ as a reference. This enforced an alignment between measurements at different energies. The algorithm of the reconstructed amplitude images from the $10.47\,\mathrm{keV}$ measurement and all XRF maps measured at the same energy were as well interpolated , cropped and then

aligned using the same shift values as the phase images.

7.7 Tomographic reconstruction

At this point all projections (phase, logarithm of amplitude and all XRF maps) have the same pixel size of $13.20\,\mathrm{nm}$, the same cropping and are aligned to one and another and to the same shared rotation axis. Therefor the tomographic reconstruction can be performed the same way for all channels of information. I choose to use the simultaneous algebraic reconstruction technique (SART) algorithm to reconstruct all volumes, but in general any other tomography algorithm could have been used. This resulted in the following reconstructed volumes:

- one volume for the phase shift of the sample
- one volume for the absorption (logarithm of the amplitude) of the sample
- one volume for the XRF photon yield for every fitted element

. . . for each of the two measured phothon energies

Just focusing on the phase shift, the absorption and the Ga–XRF yield, results in a 7 dimensional data set: three spatial dimensions, one energy dimension and one dimension for each of the reconstructed contrasts. Visualizing seven dimensions on a two-dimensional piece of paper is rather difficult.

In Fig. 7.10 spatial two-dimensional slices through the six-dimensional data set (only values at $10.470\,\mathrm{keV}$) are shown in the three main contrasts: phase shift, absorption and Ga–XRF yield. It can be seen that the same slices in different contrasts show the exact same FOV and the same sample. The GaN core and outermost shell of the micro rod can be seen in all three contrasts, while the glue surrounding the sample can best be seen in the phase shift, but not at all in the absorption. Just above the flat top of the micro rod a region of glue can be seen, which is slightly more phase shifting than the rest of the glue further down (see Fig. 7.9). This region also shows a bit of absorption and some Ga–XRF yield, but not as much as the micro rod. During the FIB milling this region of glue was exposed to the focused Ga-ion beam. Later only the sides of the sample were cleaned using a FIB with a reduced current. It has to be assumed that this *hat* is organic glue with Ga atoms embedded into it, which would explain the increased phase shift and Ga–XRF yield.

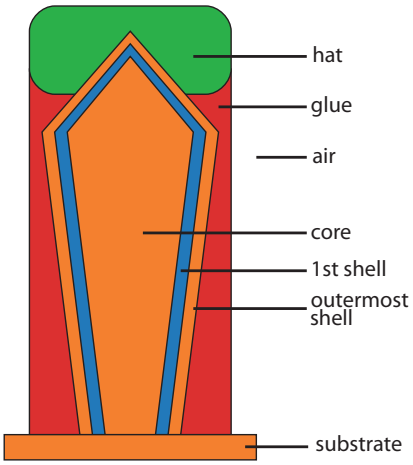

Figure 7.9: Naming scheme for the features visible in the reconstructions.

It can also be seen that the center layer, which should be a mixture of GaN and InN is clearly distinguishable against the GaN core and the outermost GaN layer of the micro rod. Surprising is that is appears to have a smaller phase shift and less absorption than the GaN reference. As indium has a higher atomic number Z than galium and therefore more electrons,

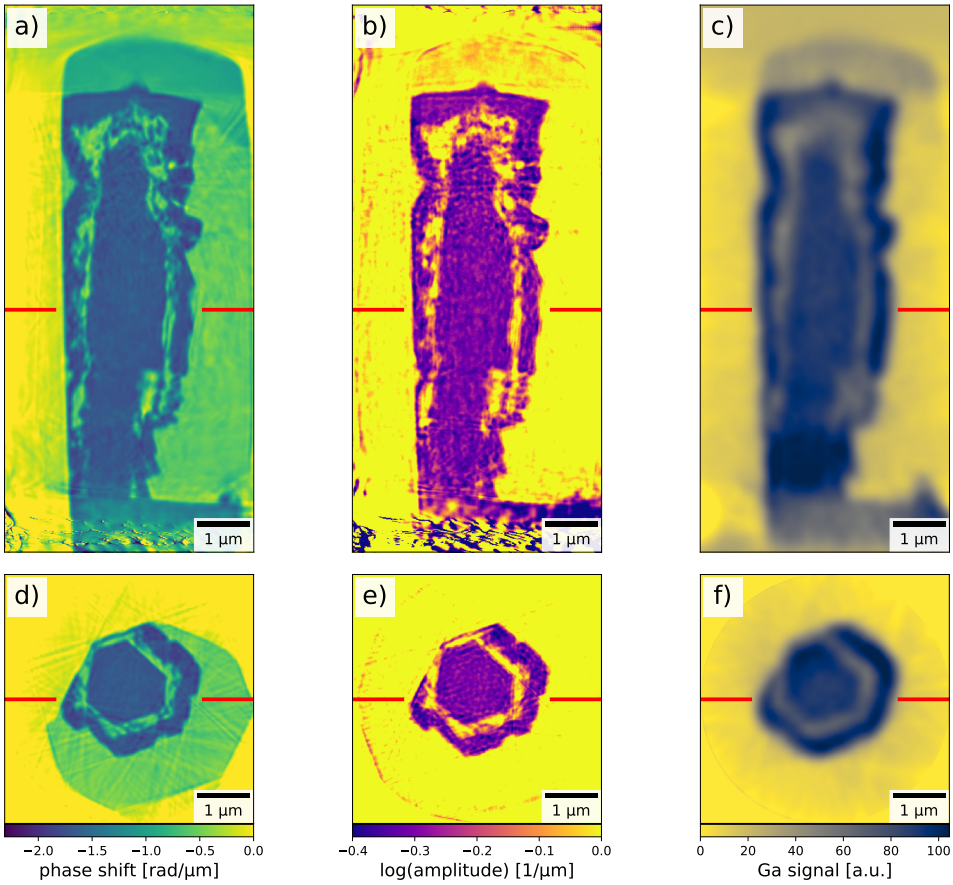

Figure 7.10: Slices through the reconstructed volumes showing three different channels of information of the dataset recorded at $10.470\,\mathrm{keV}$: (a and d) vertical and horizontal slice throught the reconstructed phase shift; (b and e) vertical and horizontal slice throught the reconstructed absorption; (c and f) vertical and horizontal slice throught the reconstructed Ga XRF signal.

one would expect to have more phase shift than for GaN. Actually it seem that the center layer has the exact same phase shift, the same absorption and a slightly higher Ga–XRF yield as the glue surrounding the micro rod. This unexpected reconstruction of the InN/GaN layer will be investigated in more detail.

7.8 Evaluation

To properly explore the whereabouts of the InN/GaN layer, the measurements at the two photon energies on and above the Ga absorption edge need to be compared. And to make sure I am looking in the right place for the missing InN, I will first verify that what I reconstructed are quantitatively correct values.

7.8.1 Quantitative values

In 6.4.4, I calculated the effective electron density and compared it to literature values for known compounds. Here I calculated the real part δ and imaginary part β of the refractive index aver-

aged over the volume of the voxel by dividing the reconstructed phase shift and the logarithm of the reconstructed amplitude by the wave number k, the edge length of the voxel d_{vx} and minus one.

$$\delta\left(\vec{\rho}\right) = \frac{\arg V\left(\vec{\rho}\right)}{-k \cdot d_{\mathrm{vx}}} \quad ; \quad \beta\left(\vec{\rho}\right) = \frac{\log\left|V\left(\vec{\rho}\right)\right|}{-k \cdot d_{\mathrm{vx}}} \tag{7.2}$$

In Fig. 7.11 a, I plotted the histogram over the phase shift of each voxel in the reconstructed volume and for each photon energy measured at. In both cases four distinct peaks can be seen: (in this order from right to left) one for air, one for the glue, one for the hat and one for the core and outermost shell material. I fitted a set of 4 Gaussians to this histogram, while leaving the center, the height and the width of each Gaussian as a free fit-parameter. From the center of the peak representing the core and outermost shell material I calculated δ according to equation 7.2 and using the width of the peak for calculating an error. The two values for the calculated δ at the two photon energies measured at are shown in Fig. 7.11 b as red points. Additionally I plotted the literature value for pure InN (orange dotted) and pure GaN (blue dotted) [109]. The solid blue line I calculated from an extended X-ray absorption fine structure (EXAFS) spectrum recorded on GaN using the Kramers-Kronig relation (see chapter 2.5) using the software *KKcalc* [110]. The EXAFS spectrum of GaN was kindly provided by Maria Katsikini (Aristotle University of Thessalonik) [111]. It can be seen that the red points match the blue GaN reference very well. Moreover it can be seen that the δ for InN is expected at even higher values, which would place it even further to the left in Fig. 7.11 a.

I performed the equivalent analysis using the absorption term of the reconstructed volume. In Fig. 7.11 c I plotted the histogram over the logarithm of the amplitude of each voxel in the reconstructed volume and for each photon energy measured at. Two main peaks can be seen: (to the right) one for air with a side bump for the hat and (to the left) one peak for the core and outermost shell material. Again I fitted the center, height and width of the peaks using Gaussians and calculated β values for the peaks representing the core and outermost shell material with equation 7.2. In Fig. 7.11 d I plotted the resulting values against the literature reference for InN (orange dotted) and for GaN (blue dotted). I also included the provided EXAFS spectrum (blue solid). Again the extracted values (red) match the reference for GaN (blue) extremely well. For this reason I am very confident, that the voxels with values in these fitted peaks are pure GaN, or at least pure relative to the calculated error bars. Also we know that both the core and the outer most shell are both doped with different atoms, but with minute amounts. The expected literature values for GaN were confirm for both δ and β. Therefor one can also assume that the other voxel values are not artifacts, but real quantitative values as well. It also allows us to directly search for InN.

7.8.2 Resonant measurements

The previous analysis only evaluated the histogram over all voxel in reconstructed volumes. It did not check if those voxels, which show a phase shift or absorption close to GaN at $10.370\,\mathrm{keV}$

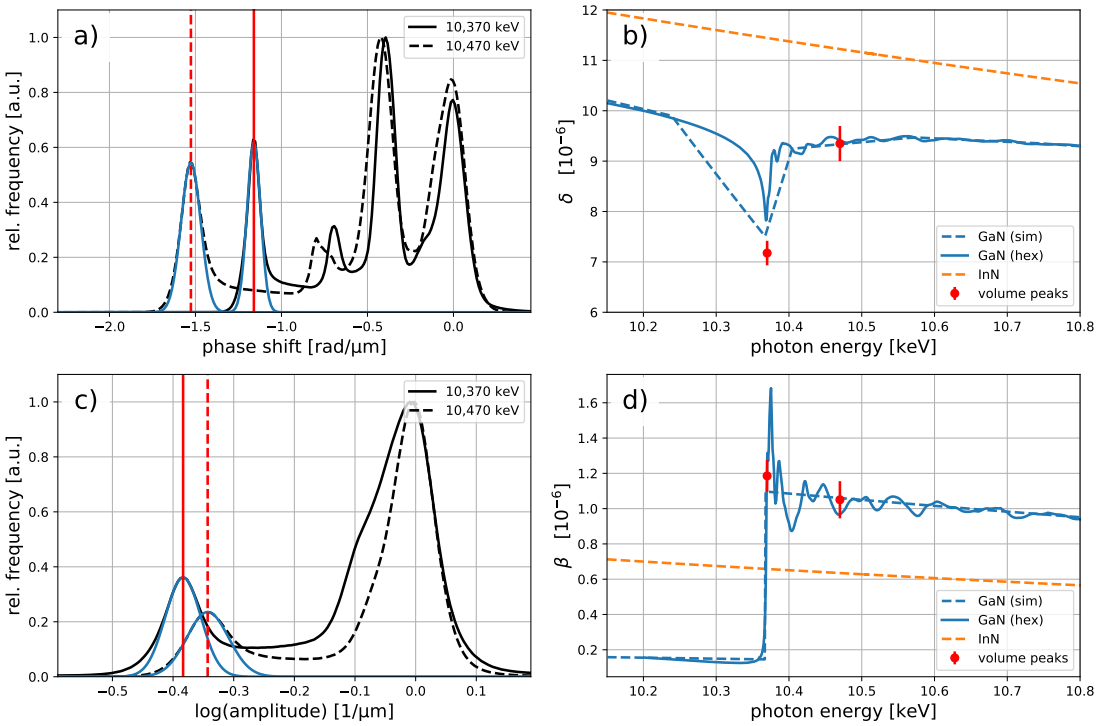

Figure 7.11: (a) histograms over the reconstructed phase shift per voxel for the measurements at both photons energies with the Gaussian fits of the left most peaks (blue) and their centers (red). (b) the theoretical $\delta\,(E)$ for InN (orange) and GaN (blue) overlayed with the extracted values from (a) (red). (c) histograms over the reconstructed absorption per voxel for the measurements at both photons energies with the Gaussian fits of the left most peaks (blue) and their centers (red). (d) the theoretical $\beta\,(E)$ for InN (orange) and GaN (blue) overlayed with the extracted values from (c) (red).

at the very same voxels that show values close to GaN at $10.470\,\mathrm{keV}$ as well. For this reason, I calculated the two-dimensional histogram comparing the phase shift for every voxel measured at the two photon energies (see Fig. 7.12 a) and another two-dimensional histogram comparing the logarithm of the reconstructed amplitude for every voxel measured at the two photon energies (see Fig. 7.12 b). It can be seen that only very localized spots can be seen in these two-dimensional histograms, meaning that the voxel value determined from the reconstruction from the first measurement at the first photon energy correlates with the voxel value reconstructed for the measurement at the second photon energy. The absence of vertical and horizontal stripes shows that the compared volumes are aligned correctly to each other. One of the localized spots is always at the origin $(0, 0)$ and represents all voxels that show air. No hot spots can be found towards the positive direction of the axes beyond the origin, which agrees with the physical model, that the electrons in the atoms shell negatively phase shift the probing photon beam and absorb intensity instead of increasing it. All spots representing regions expected to contain Ga (the core, the outermost shell and the hat), show a deviation from the diagonal, which represents no change between measurements. These deviations are due to resonant measurement at the Ga–edge. The phase shift at $10.470\,\mathrm{keV}$ is stronger (more negative), therefor these peaks containing Ga atoms can be found below the diagonal . The absorption at $10.370\,\mathrm{keV}$ is slightly stronger, therefor the corresponding peaks can be found just above the diagonal.

As all expected resonant effects could be observed and the voxel values represent literature

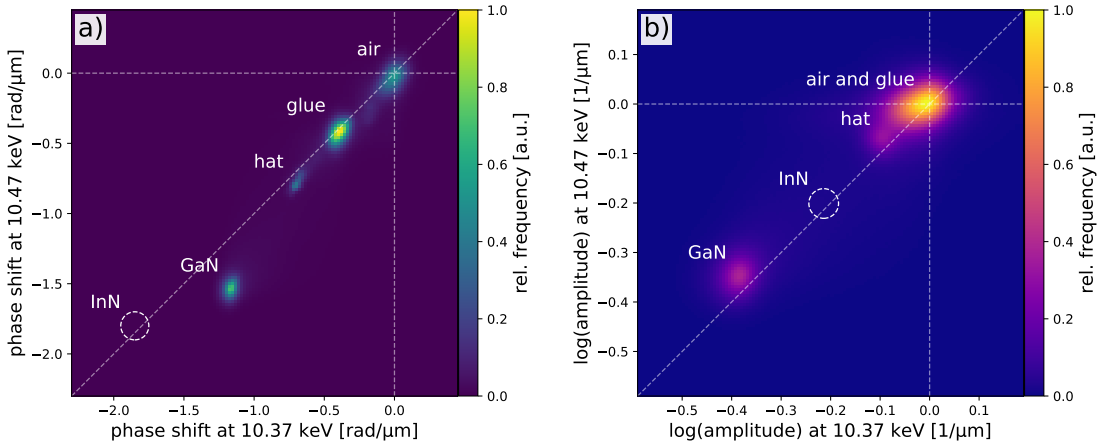

Figure 7.12: Two-dimensional histograms showing the (a) phase shift and (b) absorption in every voxel reconstructed at the two different photon energies. Marked with a white dotted circle are the regions where pure InN is expected to be found.

values, I marked the expected position of pure InN with a white dotted circle in Fig. 7.12. No pure InN is expected to be found in the sample, but mixtures of GaN and InN. Voxels of such a mixture should be found in between the spot marked with GaN and the white dotted circle in Fig. 7.12. No streaks from the GaN spot towards the InN location can be observed. One of two things could be the reason for that:

- there are no voxels containing a mixture of GaN and InN in the reconstructed volume
- the relative amounts of InN in these voxel is so small that it can not be resolved due to the spread of the GaN spot itself

None of the two possibilities can be confirmed or falsified. I can only give an lower border for the resolution limit of the InN concentration:

The measured FWHM spread of the phase shift GaN peak was measured to be $0.1346\,\mathrm{rad\,\mu m^{-1}}$. The distance between pure GaN and pure InN was measured to be $0.7524\,\mathrm{rad\,\mu m^{-1}}$. Assuming that the phase shift changes linear with the relative composition of InN and GaN, I calculated that InN contents of $\leq 17.9\,\%$ can not be detected. This is lower detection limit is rather high, but not improbable. Higher amounts of InN content have been measured on similar samples before [102]. In fact the relative amounts of InN in this specific sample should surpass this lower limit as it was specifically grown as a test sample to evaluate the limits of this evaluation method. Having the center layer showing so clearly in all three channels of information, but not measuring any InN in the XRF spectra and seeing the absolute amount phase shift decrease instead of increase compared to GaN indicates that there once was a center layer, but it somehow vanished and was replaced by the organic glue. The absence of Ga in this center layer supports this hypothesis. If the amount of In would just be below the detection limit, the center layer should also just show as GaN.

As the layer containing the In vanished, its In content can not be determined. But the core and the outer most layer are still there, allowing to measure the thickness of the void, which replaced the center layer. Hence one of the two possible reasons for the observed red shift of these micro-rods can still be examined.

7.8.3 Thickness of the center shell

To measure the thickness of the center shell, horizontal slices of the reconstructed phase shift volume, measured at $10.470\,\mathrm{keV}$, were extracted at multiple positions along the micro rods height in $500\,\mathrm{nm}$ steps. The very tip of the rod was excluded due to its usual shape and different crystallographic growth direction. For each of the six facets the surfaces GaN core - center shell and center shell - outer most GaN shell were fitted using two parallel lines. The distance between these two lines was measured and used as the layer thickness for that facet at that height.

Fig. 7.13 shows the results of the layer thickness measurements for all six facets. It can be seen that the measured thicknesses for individual facets fluctuate, but the overall trend of increasing thickness with height above the substrate can be seen in all facets. This effect was observed on similar samples before [102] and is a result from the molecular vapor deposition method used to grow this shell. The average shell thickness increases from $\approx 110\,\mathrm{nm}$ just $0.5\,\mu\mathrm{m}$ above the substrate to $\approx 360\,\mathrm{nm}$ at $5.5\,\mu\mathrm{m}$ height. This is also extremely large for such samples, as usual thicknesses are in the range of $10\,\mathrm{nm}$ to $20\,\mathrm{nm}$, but this sample was specifically designed to have an extremely thick center shell.

The measurement was complicated by floating GaN residue in the center shell (see Fig. 7.13a facet 3) and two facets having been cut by the FIB milling (see Fig. 7.13a facets 5 and 6). Additionally the irregular frown core made it difficult to define the edge GaN core - center shell at some heights.

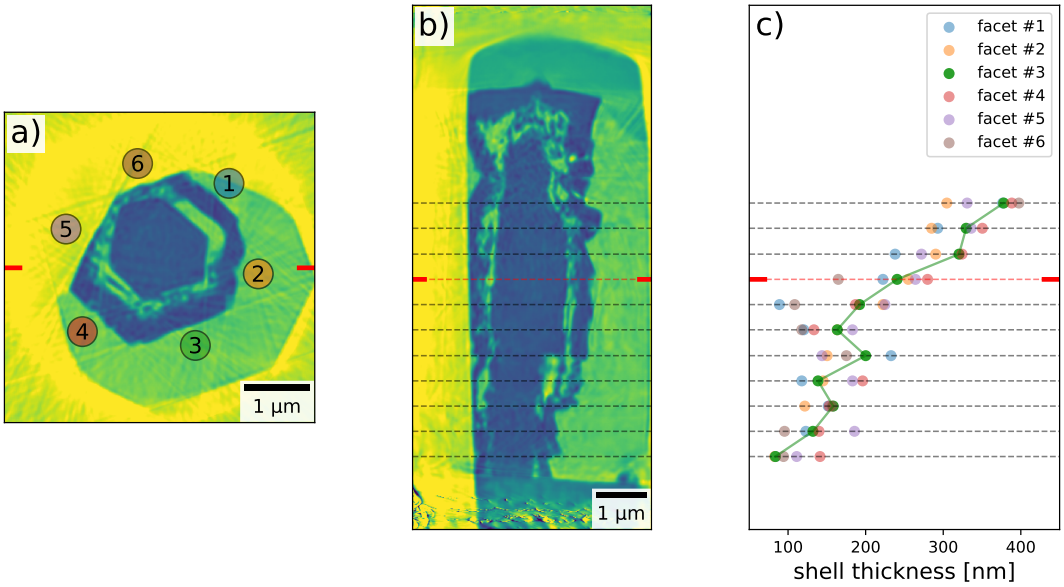

Figure 7.13: Measurement of the thicknesses of the center shell: a) numbering of the six facets; b) heights along the rod at which the thickness were measured; c) measured thickness at different heights for all facets, with the exemplary trend of facet 3 (green) highlighted.

It has to be stressed, that these measurements were done on the void left by the initially grown InN/GaN mixture. The process, which led to the disappearance of the center shell, might have influenced the distance between the core and the outer most shell. As the outer most shell

did not brake apart and the center shell was replaced by organic glue, it can be assumed that this influence was minimal.

7.8.4 Resolution

To estimate the achieved resolution of the ptychographic reconstructions I split the two data sets into halves each and reconstructed each half by itself. The two pairs of reconstructed volumes I used as input for the Fourier shell correlation (FSC). The results are shown in Fig. 7.14. For both data sets the estimated resolution is $37\,\mathrm{nm}$, which is smaller than the Crowther limit (see chapter 4.3) of $41\,\mathrm{nm}$. Therefor it is the more conservative choice to use the Crowther limit as an estimate for the achieved resolution.

It could be argued, that a perfectly cubic sample only needs two projections to be described perfectly and a perfectly hexagonal micro rod only needs three projections to be measured correctly. But these projections would have to be measured at the correct angles and non other than the perfect angles. As the samples shape is irregular and the best assumption is to assume nothing about the sample, the $41\,\mathrm{nm}$ seem the better estimate of the resolution. Moreover artifacts from the tomographic reconstruction of an angular under-sampled data set could have created these high spatial frequency features, which pushed the FRC up beyond the Crowther limit.

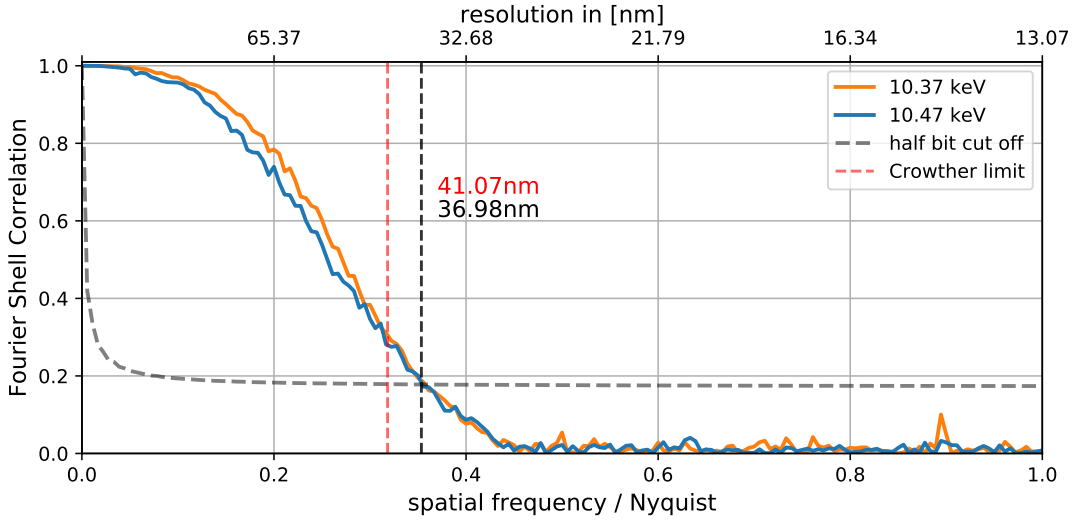

Figure 7.14: Resolution estimation by FSC for the ptchographicly reconstructed volumes of the two datasets measured at $10.370\,\mathrm{keV}$ and $10.470\,\mathrm{keV}$.

Estimating the resolution of the XRF data can be done by looking at the reconstructed beam sizes at each energy. For the measurement at $10.370\,\mathrm{keV}$ beam size was $135.3\,\mathrm{nm}$ in the horizontal and $168.1\,\mathrm{nm}$ in the vertical direction and followed a Gaussian beam shape. Adding $13\,\mathrm{nm}$ for the added smoothing during the creation of the XRF maps results in $\sqrt{135.3^2 + 13^2} = 135.9\,\mathrm{nm}$ (h) $\times 168.6\,\mathrm{nm}$ (v). As $135.9\,\mathrm{nm}$ is larger than the Crother limit of $41\,\mathrm{nm}$ and the XRF volumes are inherently aligned to the ptychographicly reconstructed volumes, it can be assumed

that the resolution inside the tomographic plane (horizontal) is $135.9\,\mathrm{nm}$, while the resolution perpendicular to the tomographic plane (vertical) the resolution is $168.6\,\mathrm{nm}$. Using the same argument for the beam size reconstructed from the data set measured at $10.470\,\mathrm{keV}$ one ends up with a resolution of $175.1\,\mathrm{nm}$ inside the tomographic plane tomographic plane and $184.3\,\mathrm{nm}$ perpendicular to the tomographic plane. Looking back at Fig. 7.10c and f, this seems plausible, as the center shell is just barely resolved.

7.9 Conclusion

It was shown that the data sets recorded at two different photon energies could both be reconstructed using the conventional PXCT algorithm despite their huge size. The reconstructed projections could be scaled to the same size and aligned to each other, making the tomographicly reconstructed volumes inherently aligned to each other. The additional channel of information, the simultaneously measured XRF spectra could be fitted and the maps created could also be made in a way to be inherently aligned with the reconstructed PXCT volumes, by utilizing the refined positions from the ePIE algorithm and the reconstructed probes. All channels of information: phase shift, absorption and XRF yield at both measured photon energies create one multi-dimensional data set of volumes.

The relative mixture of InN and GaN in the center shell of the rod could not be reconstructed as it was surprisingly absent. It was proven that something unexpected happened to this center shell, as it was replaced by glue. Currently the working hypothesis is that the organic glue dissolved the less stable (In,Ga)N shell layer trough holes in the outer most GaN shell layer and then filled the void inside [112].

The thickness of the absent layer could only be measured by measuring the thickness of the remaining glue filled cavity. The thickness could be measured for each facet individually. The expected trend of increasing thickness with height along the rod was verified.

Multiple problems with the experiment have been identified. To improve the current measurement one should:

- Make sure the sample contains In by aiming for more realistic growing parameters.
- Use another glue that does not dissolve the interesting shell.
- Do not cut into the sample during FIB milling.
- Measure around the absorption of the element you are interested in.
- Use a Kirkpatrick-Baez mirror system to have an (nearly) unchanged focus when changing the photon energy.
- Record a third volume below the absorption edge.
- Have the sample and XRF detector inside a vacuum chamber.
- Increase the stability of the sample mount to void the need for the position correction in the ePIE algorithm.

Besides these possible improvements, the strengths of these simultaneous multi-modal res-

onant measurements have been shown. Measuring at even more energies above the absorption edge would even allow for chemical contrast [48], for example between different oxidation states of the same element. The amount of data to handle is huge, but at upcoming Diffraction Limited Storage Rings DLSRs such measurements will be performed routinely. The increase of the coherent flux by two to three orders of magnitude will void the current reason to separate PXCT and XRF tomographic measurements: the increased incoherent flux for the XRF measurements.

7. Micro rod

Chapter 8

Copper nano cubes

8.1 Motivation of the experiment

Nano-structured materials based on copper can be used in photo- and electro-catalysis or as gas sensors [113, 114]. Cubic Cu based particles with sizes below $100\,\mathrm{nm}$ have shown an increased efficiency in the electrocatalytic reduction of various hydrocarbons compared to their bulk counterparts [114, 115]. Here I want to present the example of the formation of Cu_2O and Cu cubes in solution [113, 116]. The synthesis in solution allows to form these nano-cubes on various supports. Extending the time for the synthesis results in complete coverage of the support with Cu_2O cubes which are eventually reduced to a metallic Cu film. The thickness of the resulting film always correlates to the size of the initial Cu_2O cubes and does not surpass $100\,\mathrm{nm}$. This could ultimately be utilized for ultra thin and flexible electronics.

Understanding why the film thickness does not increase with extended synthesis duration requires to know when and how the initial Cu_2O cubes form and when they get reduced to metallic Cu. This requires to measure them as the synthesis happens. X-rays are the perfect probe for such in-situ experiments due to their ability to penetrate the vessel containing the solution in which the Cu_2O cubes are formed. Reducing the absolute synthesis volume below $1\,\mathrm{ml}$ would strongly affect the kinetics of the reaction, making the obtained results not comparable to larger scales. Therefor electron microscopy is not suitable as the electrons penetration length is too short for larger volumes if liquid. Experiments in the visible range can and have been performed, but only result in information averaged over the area of the beam profile. To see the transformation of individual particles as the synthesis progresses, I will use X-ray ptychography. Doing this resonantly at the copper K-edge would allow to distinguish the different copper oxidation states. But the resonant aspect of the such an experiment will not be presented here.

8.2 Sample preparation

The experiment presented here was part of an experiment prior to an actual in-situ measurement. A strip Kapton foil was placed inside the solution before the synthesis was started and

removed at a certain time during the synthesis. The Kapton foil then contained a snapshot of the synthesis, which could be analyzed ex-situ via scanning electron microscopy (SEM) and X-ray ptychographic measurements.

The synthesis of the particles was carried out by Lukas Grote at Center for Hybrid Nanostructures (CHyN) of the University of Hamburg. Copper acetylacetonate was mixed with benzyl alcohol, before the cleaned piece of Kapton was placed inside the solution [117]. The solution was then heated to $180\,^{\circ}\mathrm{C}$ and kept at this temperatures for $60\,\mathrm{min}$. The Kapton foil was removed, cleaned by rising with ethanol and dried. Fig. 8.1 shows this process schematically.

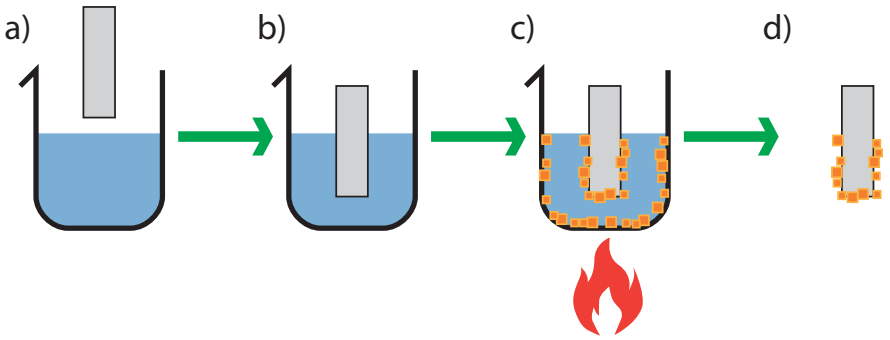

Figure 8.1: Schematic of the sample synthesis: a) a beaker is filled with copper acetylacetonate and benzyl alcohol while a clean piece of Kapton (grey) is prepared; b) the Kapton foil is placed upright in the liquid; c) heating to $180\,^{\circ}\mathrm{C}$ starts the growth of Cu nano cubes, which deposit on all surfaces; d) the Kapton foil is removed from the beaker,rinsed with ethanol and dried leaving Cu nano cubes on both sides of the Kapton foil.

The Kapton foil used in the presented experiment ended up being covered on both sides with Cu_2O cubes that haven't yet reduced to a single metallic Cu film. Fig. 8.2 shows SEM images of the two sides of a similar sample, revealing the heterogeneous coverage of the two imaged regions. The differences in coverage with nano-cubes are not limited to the front and back of the kapton foil, but also to regions on the same side of the Kapton. Moreover particles with a non-cube shape can be seen. Some are cubes that fused with other cubes, while others are even more irregularly shaped.

8.3 Measurement

The X-ray ptychographic measurment was carried out at hard X-ray nanoprobe beamline P06 of the PETRA III synchrotron radiation source [118, 119]. The Kapton foil was glued on a silicon plate with a round cut out of $10\,\mathrm{mm}$ diameter. The sample was mounted inside the PtyNAMI [41] setup with the X-ray beam hitting the surface of the kapton foil under $90°$. The X-ray beam from the undulator was monochromatized to $9.1\,\mathrm{keV}$ using a double crystal monochromator (DCM). Higher harmonics were suppressed using a pair of mirrors downstream the DCM. A Fresnel zone plate (FZP) (diameter $D_{\mathrm{FZP}} = 125\,\mu\mathrm{m}$; outermost zone width $70\,\mathrm{nm}$) was used to focus the beam. The sample was placed about $750\,\mu\mathrm{m}$ upstream of the focus, as the presented scan was intended as an overview scan and the increased beam profile on the sample

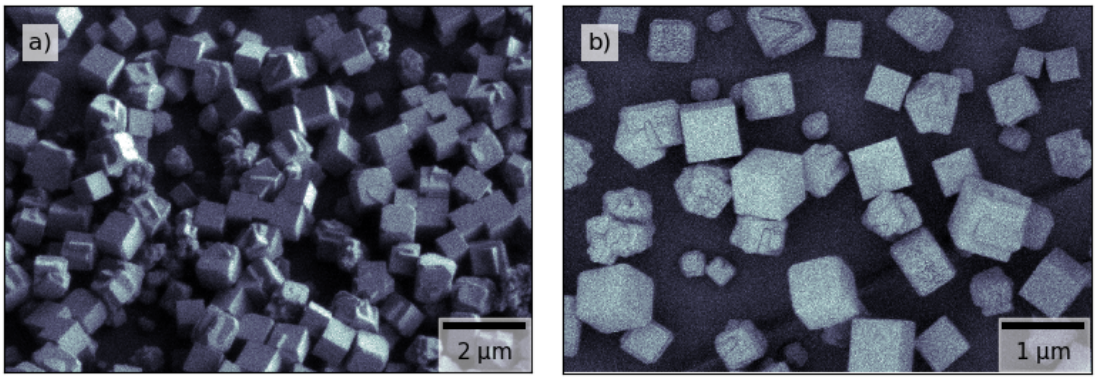

Figure 8.2: SEM images of a sample similar to the one used in the X-ray ptychographic imaging experiment: a) secondary electron image of titled sample at $1\,\mathrm{keV}$ electron beam energy; b) mixed secondary and back scattered electron beam image of the at $300\,\mathrm{eV}$ electron beam energy showing some irregularly shaped particles.

allowed for larger steps and therefor a larger field of view (FOV). Fig. 8.3 shows a schematic overview of the experimental setup.

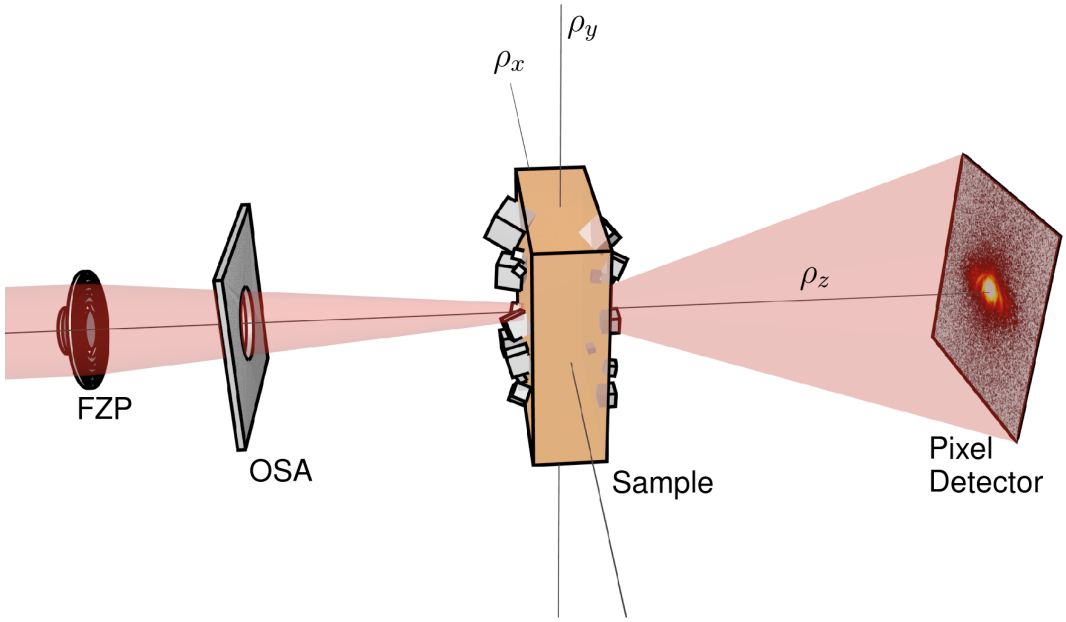

Figure 8.3: Scheme of the experimental setup showing the order of the central stop, the FZP, the OSA, the Kapton foil with copper nano cubes on both sides and the detector in the beam (red).

As the nano-cubes covered all of two surfaces of the kapton no alignment on a specific sample region was necessary. A region of interest of $10\,\mu\mathrm{m} \times 10\,\mu\mathrm{m}$ was scanned in a rectangular grid with a $500\,\mathrm{nm}$ step size resulting in $21 \times 21 = 441$ exposure positions. At each position one diffraction pattern was recorded by a photon counting pixel detector (EIGER X 4M, DECTRIS, Switzerland) positioned $4.16\,\mathrm{m}$ downstream of the sample. Each diffraction pattern was exposed for $5\,\mathrm{s}$. A flight tube under vacuum was placed to between the sample and the detector to reduce scattering on air molecules. The relative sample positions were measured using an interferometer based sample tracking system. The thickness of the Kaption foil was measured

post-experiment to be about $100\,\mu m$. All measurment parameters are summarized in table 8.1.

Table 8.1: Experimental parameters of the ptychographic measurement done on the copper nano-cubes on the 1st of October in 2017.

Parameter	
scan area ($h \times v$)	$10\,\mu m \times 10\,\mu m$
dwell time per scan point	$5\,s$
number of points ($h \times v$)	$21 \times 21 = 441$
step size	$500\,nm$
beam size on the sample (FWHM)	$1150\,nm$
FZP diamter	$125\,\mu m$
FZP outermost zone width	$70\,nm$
FZP focal length	$64.2\,mm$
photon energy	$9.1\,keV$
photon flux	$5. \cdot 10^8$ photons/s
sample-detector distance	$4.16\,m$
detector pixel size	$75\,\mu m$
overall measurement duration	$47\,min$

8.4 Single-slice ptychography

The sample was not rotated during the measurement. Only a single projection was recorded. First I will try to reconstruct the measured data set using the conventional (single-slice) extended ptychographical iterative engine (ePIE) algorithm [53]. Afterwards I will examine if the thin sample approximation [53, 61] (see 3.2.1) is applicable in this case.

8.4.1 Reconstruction

All 441 diffraction patterns were cropped to a size of 512×512 pixel, resulting in a pixel size of $14.76\,nm$ in the reconstructions. The ptychographic reconstructions were perfomed using the graphics processing unit (GPU)-optimized software *ptycho* utilizing the ePIE algorithm. After 200 iterations of the standard ePIE algorithm (see algorithm 1) the following 800 iterations were performed with an simultaneous parallel update over all exposure positions. It took about $5\,min$ to perform these 1000 iterations. The phase and logarithm of the amplitude of the reconstructed object are shown in Fig. 8.4 as well as the reconstructed complex valued probe.

In the reconstructed phase single cubes can be seen as well as clumped up agglomerations of several cubic particles. A wavy background can be seen in the phase image. This could be a result of:

- a non-uniform thickness of the Kapton foil (maybe due to the heating progress)
- residue from the drying process

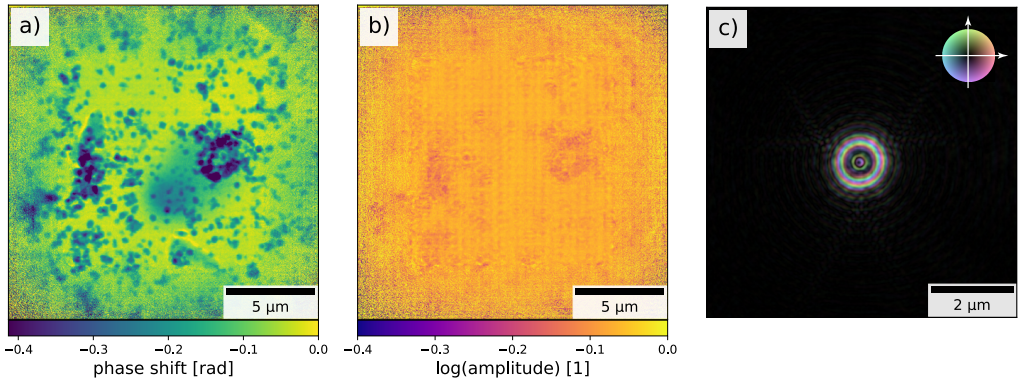

Figure 8.4: Ptychographic single-slice reconstruction of the recorded data set: a) the reconstructed phase shift of the object; b) the logarithm of the reconstructed object amplitude and c) the reconstructed complex-valued probing wavefield, where the brightnes encodes the amplitude and the color encoded the phase.

- a reconstruction artifact due to an angular change of the probing beam

The regions imaged by SEM have not shown any contamination with any material with high atomic number elements on the surface. A difference in phase shift of $0.2\,\mathrm{rad}$ as seen in Fig. 8.4a would be explained by $1.2\,\mu\mathrm{m}$ of Kapton. The possibility of an angular change of the probing beam can not be excluded, especially as the exposure time of $5\,\mathrm{s}$ was rather long for such a measurement, stretching the duration of the whole measurement to $47\,\mathrm{min}$.

The absorption image shows mostly the larger agglomerations of particles and suffers from artifacts due to the grid scan pattern and the small relative overlap of $43\,\%$ between neighboring exposure positions. The estimated transmission of $100\,\mathrm{nm}$ of metallic Cu is $97.6\,\%$ and $97.8\,\%$ for Cu_2O. Due to this low absorption and the strong artifacts, all further evaluations will be performed on the phase of the reconstructed object.

8.4.2 Depth of focus

To validate the result of the single-slice reconstruction, I will check if the thin sample approximation is valid for this measurement. The first criterion often used is the depth of focus (DOF) of the probing X-ray beam. Is the sample thinner as the DOF, the beam profile does not change significantly while propagating through the sample and the thin sample approximation is applicable. The DOF of the used FZP can be calculated as:

$$DOF = \frac{\lambda}{(NA)^2} = \frac{4\,\lambda\,f_{\mathrm{FZP}}^2}{D_{\mathrm{FZP}}^2} = 143.8\,\mu\mathrm{m}, \tag{8.1}$$

where λ is the wavelength of the probing X-ray beam, $f_{\mathrm{FZP}} = 64.2\,\mathrm{mm}$ is the focal length and $D_{\mathrm{FZP}} = 125\,\mu\mathrm{m}$ is the diameter of the used FZP. The thickness of the Kapton foil ($100\,\mu\mathrm{m}$) is thinner than the DOF of the probing X-ray beam. Using this criterion the thin sample approximation is valid.

But in the presented experiment, the photon counting pixel detector is placed at the position

of an objective lens in a conventional microscope. The ePIE algorithm performs the inverse Fourier transform to reconstruct the image instead of a lens. Therefor the DOF of the imaging lens, the photon counting pixel detector, has be considered when evaluating the depth resolution capabilities of the imaging setup. The distance between sample and detector can be understood as the focal length $f_{\mathrm{DET}} = 4.16\,\mathrm{m}$ of the detector, while the size of the cropped diffraction patterns can be understood as the diameter $D_{\mathrm{DET}} = 512 \cdot 75\,\mu\mathrm{m} = 38.4\,\mathrm{mm}$ of the imaging lens. Using these values the DOF of the detector can be calculated to:

$$DOF_{\mathrm{DET}} = \frac{\lambda}{(NA_{\mathrm{DET}})^2} = \frac{4\,\lambda\,f_{\mathrm{DET}}^2}{D_{\mathrm{DET}}^2} = 6.4\,\mu\mathrm{m}. \tag{8.2}$$

This is the theoretical depth resolution limit of the detector at this distance, with this cropping and measuring at this wavelength. $6.4\,\mu\mathrm{m}$ are considerably smaller than the thickness of the Kapton foil. According to this critera the thin sample approximation is not valid and the reconstruction using a single-slice algorithm is not appropriate. But the $6.4\,\mu\mathrm{m}$ are the lower limit, for when there is significant signal up to the highest measured q–values on the detector. Therefor it has to be checked up to which q–values there is significant signal on the detector. Otherwise just placing a larger detector at the same position would allow for even better depth resolution. As the largest q–value with significant signal-to-noise ratio (SNR) correlates to the achievable resolution in the reconstruction, I estimated the achieved resolution.

8.4.3 Resolution achieved

To estimate the resolution averaged over the whole FOV I divided the data set into two halves and reconstructed each half separately using the steps described in 8.4.1. Using the two resulting reconstructed objects as input for the Fourier ring correlation (FRC) [64, 66], I calculated the achieved resolution to be $49.3\,\mathrm{nm}$ (see Fig. 8.5).

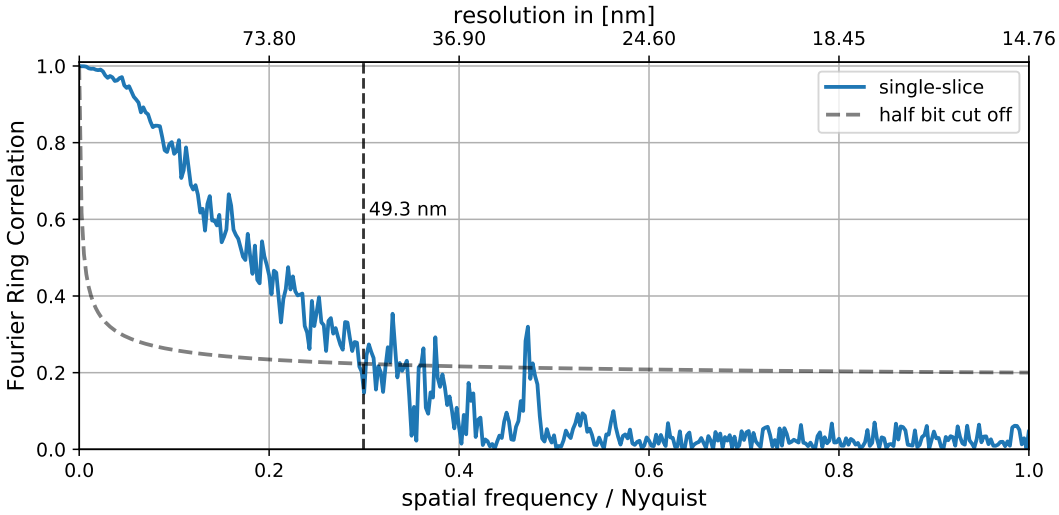

Figure 8.5: Resolution estimation by FRC for the ptychographic single-slice reconstruction.

Using the relation:

$$\Delta r = \frac{\lambda \cdot f_{\text{DET}}}{\hat{D}_{\text{DET}}} \tag{8.3}$$

between the achieved resolution δr, the distance between sample and detector f_{DET} and the corresponding needed detector diameter $\hat{D}_{\text{DET}}$ equation 8.2 can be written as:

$$DOF_{\text{DET}} = \frac{4\,\Delta r^2}{\lambda}. \tag{8.4}$$

In [55] an additional factor of 1.3 was introduced as an refinement for equation 8.4:

$$DOF_{\text{DET}} = 1.3 \cdot \frac{4\,\Delta r^2}{\lambda} = 5.2 \cdot \frac{\Delta r^2}{\lambda}. \tag{8.5}$$

Using this equation the DOF of the imaging lens, the detector, was estimated to $92.8\,\mu\text{m}$. This is surprisingly close to the $100\,\mu\text{m}$ thickness of the Kapton foil and would suggest that the presented measurement is a border line case where the thin sample approximation might just be still applicable. It is more plausible to look at the argument the other way round: The thin sample approximation is not applicable here and by reconstructing the data set using a single-slice approach regardless the resolution of the reconstruction is limited to a value that agrees with the thin sample approximation.

8.4.4 Results

The recorded data set could be reconstructed using the single-slice ePIE algorithm without problems. The sample fulfills the thin sample approximation when comparing it to the DOF of the probing X-ray beam. When comparing against the theoretical maximal depth resolution capabilities of the experimental setup with the detector acting as the imaging lens, the sample is 15 times too thick to be approximated as a thin sample. As these two criteria contradict a third criterion was tested: the achieved depth resolution was estimated via the achieved in-plane resolution of the reconstructed object. According to this third criterion, the sample is just on the edge of being thin enough to be modeled as a thin sample. I assumed that the sample is too thick for the thin sample to be applicable. The fact, that we reconstructed it using the ePIE algorithm, which is based on the thin sample approximation, limited the achieved resolution to a point where it just barely agrees with the underlying thin sample approximation. Therefor I concluded that a multi-slice reconstruction [54, 95, 120–122] had to be performed to circumvent the problem of the samples thickness.

8.5 Multi-slice ptychography

In the multi-slice model the optically thick sample is modeled by multiple optically thin sample slices placed apart from each other and free propagation of the beam in between the slices (see

chapter 5.3). For this sample two slices should suffice to model it, as all structures are either on the front side or the back of the Kapton foil. The inside of the Kapton foil can be expected to be homogeneous and no other structures were placed in the of the vicinity of the sample.

8.5.1 Reconstruction

The first slice was modeled in the same position as the slice of the single-slice reconstruction, $4.16\,\mathrm{m}$ upstream of the detector. The second slice was modeled $100\,\mu\mathrm{m}$ downstream the first slice and therefor a tiny bit closer to the detector. Fig. 8.6 shows the position of the two modeled slices along the beam profile and the DOF of the probing X-ray beam in comparison.

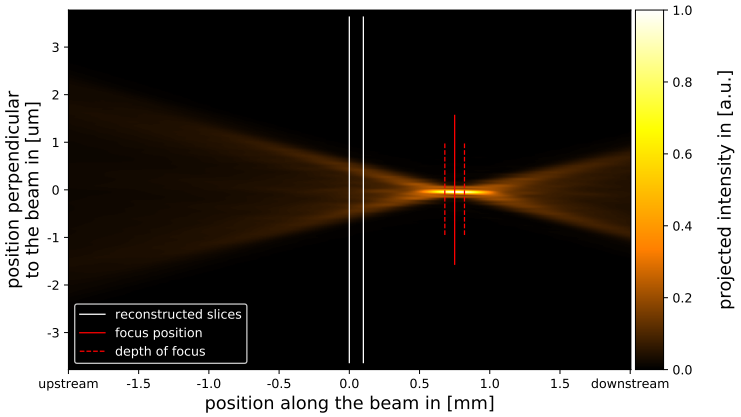

Figure 8.6: Propagated beam profile around the focus position showing the reconstructed beam intensity caustic. Marked in white: the two slice positions used for the multi-slice ptychographic reconstruction. Marked in red: the focus position (solid) and the depth of the focus (dotted).

The same cropping of 512×512 pixel was used for the multi-slice reconstruction, resulting in the same pixel size of $14.76\,\mathrm{nm}$ in the reconstructions. Again the GPU-optimized software *ptycho* [98] was used to reconstruct the data set. For the first 100 iterations only the upstream slice was used and updated, making these 100 iterations identical to the first 100 iterations of the reconstruction shown in 8.4.1, reconstructing the same object at the same slice position. From iteration 101 to 1000 the second downstream slice was used and updated as well as described in the three-dimensional ptychographical iterative engine (3PIE) algorithm [54] (see algorithm 6) with a Fresnel propagation between the two slices. As there 3PIE algorithm has to perform two additional multiplications and propagations per measurement position and iteration compared to the ePIE algorithm, it is a bit slower. The overall time needed for the reconstruction was about $15\,\mathrm{min}$. Introducing even more slices to model the sample would have increased the computational effort and subsequently the reconstruction time even more.

The reconstructed object slices and complex-valued probing wavefield (at the position of the upstream slice) are shown in Fig. 8.7. The phase images show the clearly reconstructed nano-cubes. Each nano-cube is clearly reconstructed either in the upstream slice or in the downstream slice. No nano-cube is found in both slices. The density of coverage with particles is different between the two reconstructed slices and between different regions in the same slice. This was

already expected from the SEM images of a similar sample (see Fig. 8.2). The reconstructed absorption images show strong stripe artifacts along the fast-scanned direction. Moreover these artifacts are inversed in the two slices, making their sum more or less homogeneous. This might be an artifact due angular changes of the incident beam during the measurement. The reconstructed complex-valued probing wave field matches the one from the single-slice reconstruction.

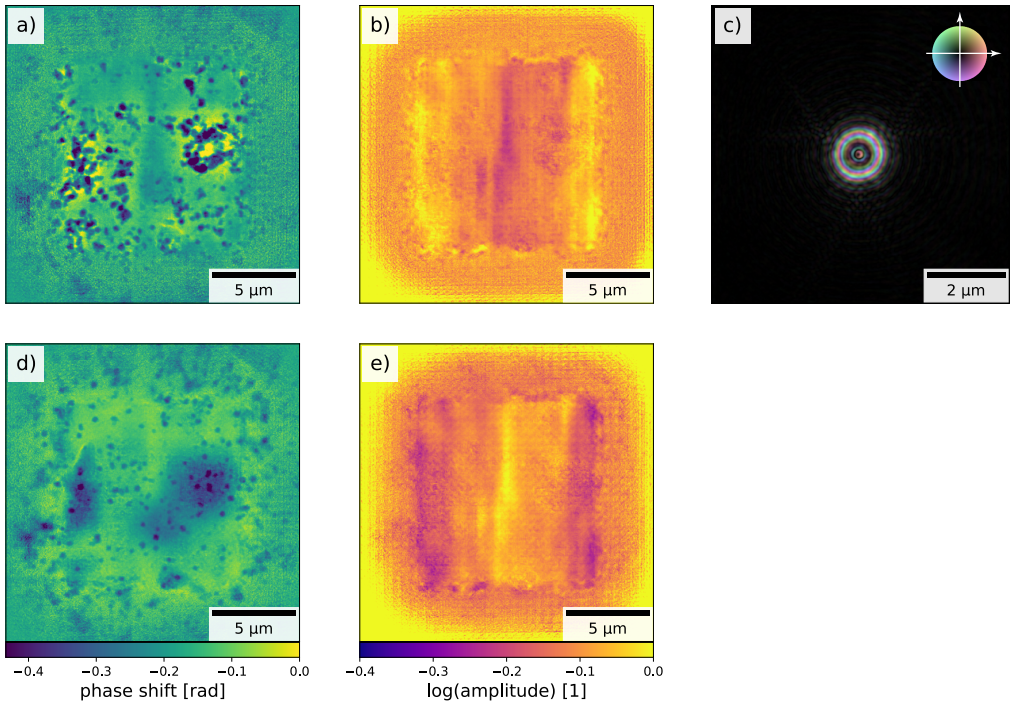

Figure 8.7: Ptychographic multi-slice reconstructions of the recorded data set: a) reconstructed phase shift of the upstream object slice; b) logarithm of the reconstructed amplitude of the upstream object slice; c) reconstructed complex-valued probing wave field at the upstream slice position; d) reconstructed phase shift of the downstream object slice closer to the focus and e) logarithm of the reconstructed amplitude of the downstream object slice.

8.5.2 Consistency of separation

To verify the separation of the nano-cubes between the upstream slice and the downstream slice, I repeated the reconstruction. But for the second reconstruction I initialized the downstream slice and only the downstream slice for the first 100 iterations and used and updated the upstream slice on top of that for the following 900 iterations. Everything else was kept the same. Now the result from the single-slice reconstructed started to develop in the downstream slice first and the particles from the upstream slice had to migrate from there to their slice. Again the reconstruction took about 15 min.

The resulting slices of the two multi-slice reconstructions are shown in Fig. 8.8c-d and f-g for comparison. In Fig. 8.8b and in Fig. 8.8e I displayed the two reconstructed slices as an colored overlay for an easier comparison against each other and the result of the single-slice

reconstruction (see Fig. 8.8a).

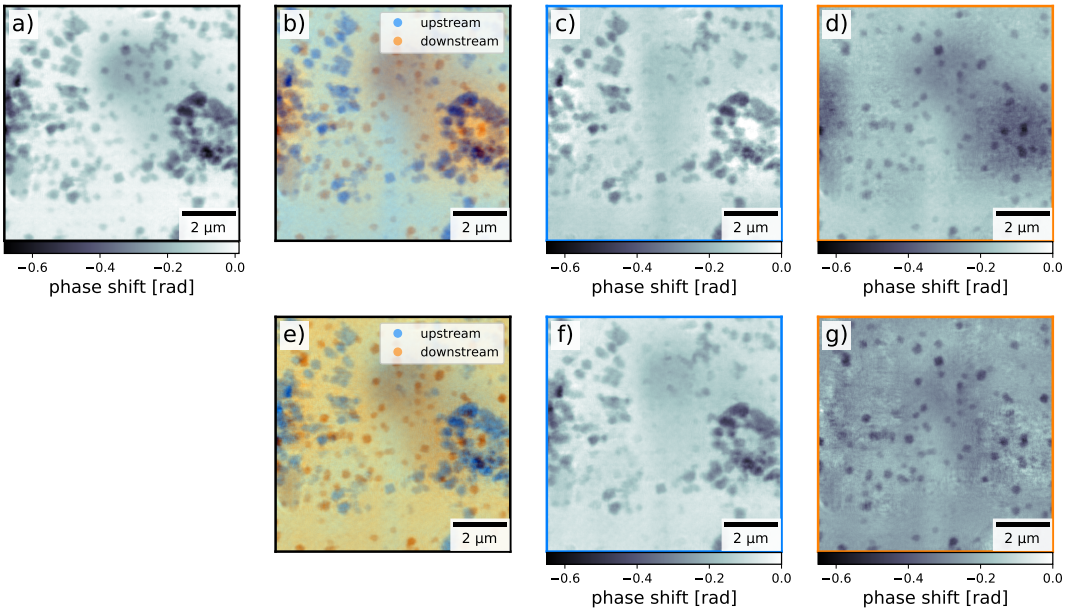

Figure 8.8: Comparison of the reconstructed object using single-slice ptychography (a) and the overlay of the object slices reconstructed using multi-slice ptychography (b and e). (b) shows the reconstruction where the downstream slice was initialized first and (e) shows the reconstruction where the upstream slice was initialized first. The two slices shown as an overlay in b) are shown separately in c) and d). The two slices shown as an overlay in e) are shown separately in f) and g).

It can be seen that each particle reconstructed with the single-slice algorithm is also reconstructed with the multi-slice algorithm. The separation of the particles into the upstream slice or the downstream slice is consistent between both multi-slice reconstructions. In fact the same slices from the two multi-slice reconstructions differ mostly only in a phase-offset and a larger background cloud-like, long-ranged artifact, which could very well be a result of the previously mentioned angular changes of the incident beam during the measurment [123]. As the initial slice was changed between the two reconstructions, the algorithm had to explain the angular changes in the incident beam by creating this cloud-like artifact in the initial slice. Once the second slice was added to the reconstruction, the algorithm could try to counter the created artifact by artifacts in the other slice. Therefor these artifacts created in both slices exchanged places in the two multi-slice reconstructions. That is why two larger darker spots can be seen to the top-right in of the downstream slice in Fig. 8.8d and in the upstream slice in Fig. 8.8f. To visualize this, I plotted the differnce of the two reconstructed upstream slices in Fig. 8.9a and the difference of the two reconstructed downstream slices in Fig. 8.9b. Adding up these differences results in a flat image (Fig. 8.9c) and proves that these artifacts indeed just switched the slice in which they were reconstructed in depending on which object slices was initalized first.

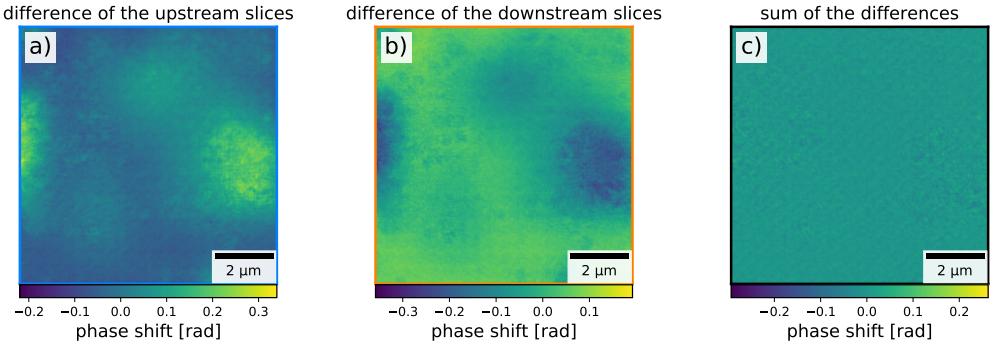

Figure 8.9: Difference of the two reconstructed phase objects in the upstream slice (a) and the downstream slice (b) and the sum of these two differences (c).

8.5.3 Resolution achieved

To estimate the resolution achieved with the multi-slice reconstruction, I again used the FRC. But I calculated the FRC of the upstream slices and the downstream slices separately and plotted them in Fig.8.10. Because each reconstruction was performed using the full dataset, I used the one-bit criterion as a threshold, resulting in an estimated resolution of 36 nm in both cases. As the stack of the two reconstructed slices also describes a volume, with admittedly very cuboid voxles, one could have also performed a Fourier shell correlation (FSC) on these volumes to also average about the resolution achieved along the beam axis. Since this is an extreme special case (the size of the transverse FOV is way smaller than the longitudinal separation of the slices), I have discarded this, as it would not have provided any additional useful information. For multi-slice reconstructions with more and closer spaced slices, using the FSC is a valid option.

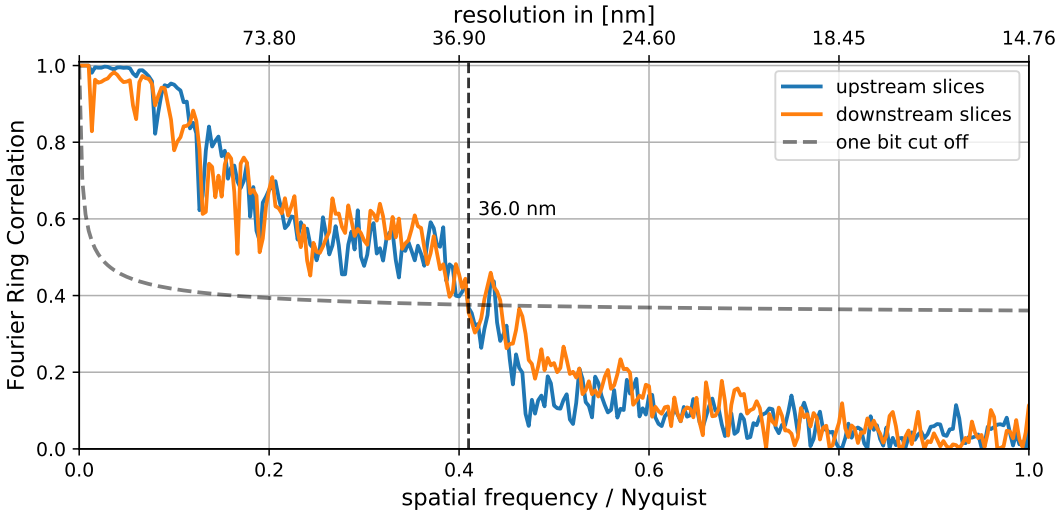

Figure 8.10: Resolution estimation by FRC for the ptychographic multi-slice reconstructions with inverted initialization order of the two slices: FRC of the reconstructed upstream object slices (blue) and FRC of the reconstructed downstream object slices (orange), result in the same resolution estimate of 36 nm.

8.5.4 Results

Performing a multi-slice reconstruction using the 3PIEalgorithm allowed to separate the particles into those that are on the upstream facing surface of the Kapton foil and those on the downstream facing surface of the Kapton foil. The separation was robust to changing the initialization order of the two slices in the reconstruction. Reconstruction artifacts on the other hand switches slices when exchanging the initialization order. The estimated achieved resolution of $36\,\mathrm{nm}$ in the two reconstructed slices surpassed the resolution of $49.3\,\mathrm{nm}$ estimated from the single-slice reconstruction.

8.6 Conclusion and outlook

In X-ray ptychographic experiments the third spatial dimension can be extracted without the need for the rotation of the sample as in an tomography scheme. The resolution of this third spatial dimension along the beam might differ strongly from the resolution achieved in the plane perpendicular to the X-ray beam. The size of the detector and the largest scattering vector $\vec{q}$ with sufficient SNR are factors that determine what this resolution can be. But even collecting all scattered intensity in a 2π solid angle behind the sample would result in a pixel size of $\lambda/2$ in the plane transverse to the probing beam, and a longitudinal resolution of λ. To be able to achieve a homogeneous resolution in all three spatial dimensions the whole 4π solid angle would have to be recorded. Therefor tomography based methods are still the better option for samples were homogeneous 3D information is important. But the combination of multi-slice techniques and tomography based methods promise the most benefits :

- a solution for the limitation of the thin sample approximation and
- the ability to record fewer angular projections (fewer than the Crowther limit would dictate) and therefor shorten the experiments duration.

As for this example the multi-slice reconstruction using the 3PIE algorithm was the optimal choice, due to the structure of the sample. For a real in-situ experiment the container walls would be even further apart than the $100\,\mu\mathrm{m}$ thickness of the Kapton foil. Resonant measurements could be performed as well to distinguish between Cu_2O and metallic Cu.

Chapter 9

Summary and outlook

Three experiments with the goal of reconstructing the sample with an additional third spatial dimension have been presented in this work. The currently most utilized method, ptychographic X-ray computed tomography (PXCT), is based on recording the sample under multiple rotation angles, reconstructing each projection on its own and using the reconstructed two-dimensional projections as input for any tomographic reconstruction algorithm. This straight-forward extension from a known two-dimensional experiment and reconstruction into the third spatial dimension relies on this separation of the three-dimensional data set into multiple independent two-dimensional data sets. Each of them has do reconstruct on its own and therefor the sampling for each projection has to be sufficient. In 6.5 I presented how a coupled algorithm can be used to reconstruct the very same data set, but utilizing the redundancy between projections. This coupled ptychographic tomography (CPT) algorithm reconstructed the same sample but with an improved estimated resolution. Moreover I have shown how the sampling of each projection could be reduced to a point where the PXCT algorithm would fail, while the CPT algorithm still faithfully reconstructs the sample. This was predicted in [91], but here it was the first time experimental was used to validate this presumption. Henceforth X-ray ptychographic tomography experiments could be performed with an reduced sampling at each projection angle, dramatically reducing the time for the overall experiment. However, these advantages come with a cost: the increased computational effort. As long as beamtime is more sparse than computing time, CPT is the way to go.

In chapter 7 I presented how an PXCT experiment can be performed in a way to obtain additional channels of information on top of the volumetric representation of the samples index of refraction. Firstly, using a small probing beam for the ptychographic measurement made it simultaneously a proper scanning transmission X-ray microscopy (STXM) experiment, which relies on the probing beam being as small as possible. The usage of an additional X-ray fluorescence (XRF)-detector allowed to create XRF maps which are inherently aligned to the ptychographicly reconstructed projection images and can therefor be reconstructed tomographically in the exact same way. This additional channel contains information about the three-dimensional spatial distribution of elements in the sample. Furthermore I performed the PXCT measurement

at two photon energies: on the Ga-K and just above the Ga-K. Such a resonant measurement also allows elemental information on the one element on which absorption edge the measurement was done. Measuring at even more energies around an absorption edge would allow to distinguish between different chemical states, such as oxidation states, of this element. The biggest drawback for this additional information is again the increased amount of time needed for the whole measurement. I demonstrated how the measurement is performed, the recorded data is treated and how it is finally analyzed. The reconstructed volumes contained quantitative and qualitative information on the spatial distribution of elements in the sample.

Both the PXCT and the CPT algorithm both rely on the thin sample approximation. Consequently both methods are limited in the thickness of the samples they can reconstruct with a certain probing beam and without loosing resolution. In 8.5 I presented how the three-dimensional ptychographical iterative engine (3PIE) algorithm surpasses the problem of thick samples, by modeling them as multiple thin samples separated by free propagation space between these slices. Using the exemplary sample of Cu nano-cubes on both sides of a Kapton foil, I demonstrated that a single-slice reconstruction of an optically thick sample doesn't fail but does not achieve the same resolution in its reconstruction as a more suited multi-slice reconstruction does. Utilizing the 3PIE algorithm in either the PXCT or the CPT algorithm would remove the limitation to thin samples. Moreover the additional longitudinal information reduces the number of angles which are needed to reduce a certain resolution in the tomographic plane, effectively breaking the Crowther limit. This has been shown by creating projections to angles which haven't been measured using the parallax shift of reconstructed slices [124] or by tomographic reconstruction algorithms which utilize this additional depth information [125]. Using the later to replace the simultaneous algebraic reconstruction technique (SART) algorithm in the CPT implementation presented in 5.2.2 and also exchanging the extended ptychographical iterative engine (ePIE) algorithm for the 3PIE algorithm would result in an improved CPT which can deal with such thick samples [126, 127].

As with all methods, one always asks how to go bigger, better and faster. How to measure bigger samples was just explained. But scanning larger regions of interest in two dimensions scales linearly with the number of steps needed to cover that area and therefor the time needed to scan that area. And the number of needed projections scales linear with the thickness of the sample. Because of that the time needed to measure a certain sample scales linearly with the volume of the sample if all other parameters are kept the same. Consequently going bigger goes hand in hand with going slower. The possible reduction in sampling presented in 6.7 is one possible way of going faster. The obvious way of speeding up the measurement process is to expose for shorter times and to reduce the dead time by using fly-scanning schemes [128–131] as done in 7.3. Unfortunately reducing the exposure time also reduces the number of recorded photons on the detector during one exposure, assuming all other parameters were kept the same. As the resolution of the ptychographic reconstruction is limited by the highest q-value at which sufficient signal-to-noise ratio (SNR) has been measured, going faster by reducing exposure times would mean sacrificing achievable resolution. Hence it all comes down to having more

flux; more coherent flux.

Fourth generation synchroton sources promise exactly that. MAX-IV, ESRF-EBS, SIRIUS, APUS-U, SPring8-II and PETRA-IV [132–137] expect to offer a fully coherent beam which would benefit coherent methods such as ptychographic tomography. With the promised gain of 100 to 1000 in coherent flux one could naively measure 100 to 1000 times faster as on third generation sources. Measuring 1000 times faster would allow to measure a 1000 times bigger sample volume in the same time. But all this only holds true if the sample is not damaged by the increased photon density during the measurement. When measuring a radiation sensitive sample, the gain from a higher coherent flux might be naught. And even with a radiation hard sample, the challenges shift. One of the PXCT data sets for one energy presented in 7.3 was recorded in $40\,\mathrm{h}$ and accumulated to $8\,\mathrm{TByte}$ [112] after cropping. Scaling this up by a factor of 1000 would result in $8\,\mathrm{TByte}$ being recorded in $2.5\,\mathrm{min}$ transforming the challenge to be a computing problem. My suggestion is to not use all of the additional flux to go faster, but also some of it to measure better. For example measuring only 10 faster would result in each diffraction pattern having 100 times more photons. Assuming an inverse-cubic law for the strength of the scattered intensity would result in approximately three times better resolution compared to current measurements, which would push the achievable resolution well below the $10\,\mathrm{nm}$ mark and therefor closer to the range of methods utilizing electrons as a probe. But also this improvement would come with a challenge: an engineering challenge. The experimental setups would need to be stable down to the few nano-meter range. Finally the increased flux would improve the signal recorded by all simultaneously performed STXM based methods such as XRF, X-ray beam induced current (XBIC) [138, 139] and X-ray beam induced voltage (XBIV) measurements.

In brief the key take away messages of this work towards the future of three-dimensional ptychographic imaging at synchrotrons are:

- Use coupled algorithms such as the presented CPT algorithm to utilize every bit of redundancy in the recorded data. This should allow for higher resolution in the reconstructions and a relaxed sampling criterion.
- Especially at fourth-generation sources: use a small probing beam and as many simultaneous STXM based methods as possible / needed, as the reconstructed multi-dimensional volume is inherently aligned and enables various examinations of the sample with just one beam time.
- Measure resonant at multiple energies around absorption edges for additional elemental or even chemical information.
- If your sample is too thick, utilize multi-slice algorithms to circumvent the worsening of the achieved resolution due to the violation of the thin sample approximation.

Bibliography

[1] Pete Vukusic, Benny Hallam, and Joe Noyes. Brilliant whiteness in ultrathin beetle scales. *Science*, 315(5810):348, 2007.

[2] Benny T. Hallam, Anthony G. Hiorns, and Peter Vukusic. Developing optical efficiency through optimized coating structure: biomimetic inspiration from white beetles. *Appl. Opt.*, 48(17):3243–3249, Jun 2009.

[3] Stephanie L. Burg, Adam Washington, David M. Coles, Antonino Bianco, Daragh McLoughlin, Oleksandr O. Mykhaylyk, Julie Villanova, Andrew J. C. Dennison, Christopher J. Hill, Pete Vukusic, Scott Doak, Simon J. Martin, Mark Hutchings, Steven R. Parnell, Cvetelin Vasilev, Nigel Clarke, Anthony J. Ryan, Will Furnass, Mike Croucher, Robert M. Dalgliesh, Sylvain Prevost, Rajeev Dattani, Andrew Parker, Richard A. L. Jones, J. Patrick A. Fairclough, and Andrew J. Parnell. Liquid-liquid phase separation morphologies in ultra-white beetle scales and a synthetic equivalent. *Communications Chemistry*, 2(1):100, August 2019.

[4] Dakota E. McCoy, Teresa Feo, Todd Alan Harvey, and Richard O. Prum. Structural absorption by barbule microstructures of super black bird of paradise feathers. *Nature Communications*, 9(1):1, January 2018.

[5] Dakota E. McCoy, Victoria E. McCoy, Nikolaj K. Mandsberg, Anna V. Shneidman, Joanna Aizenberg, Richard O. Prum, and David Haig. Structurally assisted super black in colourful peacock spiders. *Proceedings of the Royal Society B: Biological Sciences*, 286(1902):20190589, May 2019.

[6] Pete Vukusic and J. Roy Sambles. Photonic structures in biology. *Nature*, 424(6950):852–855, August 2003.

[7] Shuichi Kinoshita and Shinya Yoshioka. Structural colors in nature: The role of regularity and irregularity in the structure. *ChemPhysChem*, 6(8):1442–1459, 2005.

[8] Radwanul Hasan Siddique, Guillaume Gomard, and Hendrik Hölscher. The role of random nanostructures for the omnidirectional anti-reflection properties of the glasswing butterfly. *Nature Communications*, 6:6909, April 2015.

[9] Jeremy J. Jackson, Alex A. Puretzky, Karren L. More, Christopher M. Rouleau, Gyula Eres, and David B. Geohegan. Pulsed growth of vertically aligned nanotube arrays with variable density. *ACS Nano*, 4(12):7573–7581, December 2010.

[10] Surrey NanoSystems. Vantablack s-vis. (Accessed September 10, 2019).

[11] Matti S. Toivonen, Olimpia D. Onelli, Gianni Jacucci, Ville Lovikka, Orlando J. Rojas, Olli Ikkala, and Silvia Vignolini. Anomalous-diffusion-assisted brightness in white cellulose nanofibril membranes. *Advanced Materials*, 30(16):1704050, 2018.

[12] James H. Pikul, Sezer Özerinç, Burigede Liu, Runyu Zhang, Paul V. Braun, Vikram S. Deshpande, and William P. King. High strength metallic wood from nanostructured nickel inverse opal materials. *Scientific Reports*, 9(1):719, January 2019.

[13] Huaiyuan Wang, Jingyan Zhao, Youzhuang Zhu, Yang Meng, and Yanji Zhu. The fabrication, nano/micro-structure, heat- and wear-resistance of the superhydrophobic pps/ptfe composite coatings. *Journal of Colloid and Interface Science*, 402:253 – 258, 2013.

[14] Wilhelm Schwieger, Albert Gonche Machoke, Tobias Weissenberger, Amer Inayat, Thangaraj Selvam, Michael Klumpp, and Alexandra Inayat. Hierarchy concepts: classification and preparation strategies for zeolite containing materials with hierarchical porosity. *Chem. Soc. Rev.*, 45:3353–3376, 2016.

[15] George Kourousias, Benedetto Bozzini, Michael W. M. Jones, Grant A. Van Riessen, Simone Dal Zilio, Fulvio Billè, Maya Kiskinova, and Alessandra Gianoncelli. Monitoring dynamic electrochemical processes with in situ ptychography. *Applied Nanoscience*, 8(4):627–636, Apr 2018.

[16] Juan G. Lozano, Gerardo T. Martinez, Liyu Jin, Peter D. Nellist, and Peter G. Bruce. Low-dose aberration-free imaging of li-rich cathode materials at various states of charge using electron ptychography. *Nano Lett.*, 18(11):6850–6855, November 2018.

[17] Henrik F. Dam, Thomas R. Andersen, Emil B. L. Pedersen, Karl T. S. Thydén, Martin Helgesen, Jon E. Carlé, Peter S. Jørgensen, Juliane Reinhardt, Roar R. Søndergaard, Mikkel Jørgensen, Eva Bundgaard, Frederik C. Krebs, and Jens W. Andreasen. Enabling flexible polymer tandem solar cells by 3d ptychographic imaging. *Advanced Energy Materials*, 5(1):1400736, 2015.

[18] Young-Sang Yu, Maryam Farmand, Chunjoong Kim, Yijin Liu, Clare P. Grey, Fiona C. Strobridge, Tolek Tyliszczak, Rich Celestre, Peter Denes, John Joseph, Harinarayan Krishnan, Filipe R. N. C. Maia, A. L. David Kilcoyne, Stefano Marchesini, Talita Perciano Costa Leite, Tony Warwick, Howard Padmore, Jordi Cabana, and David A. Shapiro. Three-dimensional localization of nanoscale battery reactions using soft x-ray tomography. *Nature Communications*, 9(1):921–, 2018.

[19] Ariel Lipson, Stephen G Lipson, and Henry Lipson. *Optical physics*. Cambridge University Press, 2010.

[20] Franz Pfeiffer. X-ray ptychography. *Nature Photonics*, 12:9–17, 2018.

[21] A. Schropp, R. Hoppe, J. Patommel, D. Samberg, F. Seiboth, S. Stephan, G. Wellenreuther, G. Falkenberg, and C. G. Schroer. Hard x-ray scanning microscopy with coherent radiation: Beyond the resolution of conventional x-ray microscopes. *Appl. Phys. Lett.*, 100:253112, 2012.

[22] Juliane Reinhardt, Robert Hoppe, Georg Hofmann, Christian D. Damsgaard, Jens Patommel, Christoph Baumbach, Sina Baier, Amelie Rochet, Jan-Dierk Grunwaldt, Gerald Falkenberg, and Christian G. Schroer. Beamstop-based low-background ptychography to image weakly scattering objects. *Ultramicroscopy*, 173:52–57, 2017.

[23] Sandra Stephan. *High-Resolution 3D Ptychography*. PhD thesis, Technische Universität Dresden, 2013.

[24] Marco Stockmar, Maxime Hubert, Martin Dierolf, Bjoern Enders, Richard Clare, Sebastian Allner, Andreas Fehringer, Irene Zanette, Julie Villanova, Jérôme Laurencin, Peter Cloetens, Franz Pfeiffer, and Pierre Thibault. X-ray nanotomography using near-field ptychography. *Opt. Express*, 23(10):12720–12731, May 2015.

[25] Mirko Holler, Manuel Guizar-Sicairos, Esther H. R. Tsai, Roberto Dinapoli, Elisabeth Müller, Oliver Bunk, Jörg Raabe, and Gabriel Aeppli. High-resolution non-destructive three-dimensional imaging of integrated circuits. *Nature*, 543:402–, March 2017.

[26] Julio C. da Silva, Jan Haubrich, Guillermo Requena, Maxime Hubert, Alexandra Pacureanu, Leonid Bloch, Yang Yang, and Peter Cloetens. High energy near- and far-field ptychographic tomography at the ESRF. *Proc.SPIE*, 10391:10391 – 10391 – 7, 2017.

[27] D. Batey, S. Cipiccia, X. Shi, S. Williams, K. Wanelik, A. Wilson, S. Pérez-Tamarit, P. Cimavilla, M. A. Ródriguez-Pérez, C. Rau, and et al. Coherence branch at I13, dls: The multiscale, multimodal, ptycho-tomographic end station. *Microscopy and Microanalysis*, 24(S2):40–41, 2018.

[28] Simone Sala, Darren J. Batey, Anupama Prakash, Sharif Ahmed, Christoph Rau, and Pierre Thibault. Ptychographic x-ray computed tomography at a high-brilliance x-ray source. *Opt. Express*, 27(2):533–542, Jan 2019.

[29] Tiago Ramos, Bastian Ellegård Grønager, Martin Skovgaard Andersen, and Jens Wenzel Andreasen. Direct three-dimensional tomographic reconstruction and phase retrieval of far-field coherent diffraction patterns. *Phys. Rev. A*, 99:023801, Feb 2019.

[30] Eugene Hecht and A Zajac. *Optics*. Addison Wesley, New York, 2002.

[31] David Attwood. *Soft X-Rays and Extreme Ultraviolet Radiation: Principles and Applications*. Cambridge University Press, New York, NY, USA, 1st edition, 2007.

[32] J. Als-Nielsen and D. McMorrow. *Elements of Modern X-Ray Physics*. John Wiley & Sons, 2011.

[33] Philip Willmott. *An introduction to synchrotron radiation*. Wiley, 2011.

[34] Eberhard J Jaeschke, Shaukat Khan, Jochen R Schneider, and Jerome B Hastings. *Synchrotron Light Sources and Free-Electron Lasers: Accelerator Physics, Instrumentation and Science Applications*. Springer, 2016.

[35] James Clerk Maxwell. *A dynamical theory of the electromagnetic field*, volume 155. Royal Society, January 1865.

[36] H. S. Green and E. Wolf. A scalar representation of electromagnetic fields. *Proceedings of the Physical Society. Section A*, 66(12):1129–1137, dec 1953.

[37] Christian Huygens. Traité de la lumiere. *Oeuvres completes XIX*, 1737, 1912.

[38] Joseph W Goodman. *Introduction to Fourier optics*, chapter 4. Fresnel and Fraunhofer Diffraction. Roberts and Company Publishers, 2005.

[39] Frank Seiboth. *Refractive Hard X-Ray Nanofocusing at Storage Ring and X-Ray Free-Electron Laser Sources*. PhD thesis, Universität Hamburg, Von-Melle-Park 3, 20146 Hamburg, 2016.

[40] J. Als-Nielsen and D. McMorrow. *Elements of Modern X-Ray Physics*, chapter 1. X-rays and their interaction with matter, pages 15–28. John Wiley & Sons, 2011.

[41] Christian G. Schroer, Martin Seyrich, Maik Kahnt, Stephan Botta, Ralph Döhrmann, Gerald Falkenberg, Jan Garrevoet, Mikhail Lyubomirskiy, Maria Scholz, Andreas Schropp, and Felix Wittwer. PtyNAMi: Ptychographic nano-analytical microscope at PETRA III — interferometrically tracking positions for 3D x-ray scanning microscopy using a ball-lens retroreflector. *Proc. SPIE*, 10389:103890E, 2017.

[42] R. de L. Kronig. On the theory of dispersion of x-rays. *J. Opt. Soc. Am.*, 12(6):547–557, Jun 1926.

[43] Hendrik Anthony Kramers. La diffusion de la lumiere par les atomes. In *Atti Cong. Intern. Fisica (Transactions of Volta Centenary Congress) Como*, volume 2, pages 545–557, 1927.

[44] David Attwood. *Soft X-Rays and Extreme Ultraviolet Radiation: Principles and Applications*, chapter Chapter 3: Wave propagation and refractive index at EUV and soft X-ray wavelengths. Cambridge University Press, New York, NY, USA, 1st edition, 2007.

[45] Edward Bedrosian. A product theorem for hilbert transforms. *RAND Corporation*, RM-3439-PR, 1962.

[46] Ben Yu-Kuang Hu. Kramers–kronig in two lines. *Am. J. Phys*, 57(9):821, 1989.

[47] Craig F Bohren. What did kramers and kronig do and how did they do it? *European Journal of Physics*, 31(3):573–577, mar 2010.

[48] Juliane Reinhardt. *Resonant Hard X-ray Ptychography for High-Sensitivity Imaging with Chemical Contrast*. PhD thesis, Universität Hamburg, Von-Melle-Park 3, 20146 Hamburg, 2017.

[49] R. Hegerl and W. Hoppe. Dynamische theorie der kristallstrukturanalyse durch elektronenbeugung im inhomogenen primärstrahlwellenfeld. *Berichte der Bunsengesellschaft für physikalische Chemie*, 74(11):1148–1154, 1970.

[50] Frank Avery Haight. Handbook of the poisson distribution. *Wiley*, 1967.

[51] C. E. Shannon. A mathematical theory of communication. *The Bell System Technical Journal*, 27(3):379–423, July 1948.

[52] Oliver Bunk, Martin Dierolf, Søren Kynde, Ian Johnson, Othmar Marti, and Franz Pfeiffer. Influence of the overlap parameter on the convergence of the ptychographical iterative engine. *Ultramicroscopy*, 108(5):481 – 487, 2008.

[53] Andrew M. Maiden and John M. Rodenburg. An improved ptychographical phase retrieval algorithm for diffractive imaging. *Ultramicroscopy*, 109(10):1256 – 1262, 2009.

[54] A. M. Maiden, M. J. Humphry, and J. M. Rodenburg. Ptychographic transmission microscopy in three dimensions using a multi-slice approach. *J. Opt. Soc. Am. A*, 29(8):1606–1614, Aug 2012.

[55] Esther H. R. Tsai, Ivan Usov, Ana Diaz, Andreas Menzel, and Manuel Guizar-Sicairos. X-ray ptychography with extended depth of field. *Opt. Express*, 24(25):29089–29108, Dec 2016.

[56] Darren J. Batey, Daniel Claus, and John M. Rodenburg. Information multiplexing in ptychography. *Ultramicroscopy*, 138:13 – 21, 2014.

[57] Jesse N. Clark, Xiaojing Huang, Ross J. Harder, and Ian K. Robinson. Dynamic imaging using ptychography. *Phys. Rev. Lett.*, 112:113901, Mar 2014.

[58] Xiaowen Shi, Nicolas Burdet, Darren Batey, and Ian Robinson. Multi-modal ptychography: Recent developments and applications. *Applied Sciences*, 8(7), 2018.

[59] F. Wittwer, R. Hoppe, F. Seiboth, J. Reinhardt, M. Scholz, and C. G. Schroer. Ptychography with a virtually enlarged illumination. *Microscopy and Microanalysis*, 24(S2):46?47, 2018.

[60] C. Bernert, R. Hoppe, F. Wittwer, Th. Woike, and C. G. Schroer. Ptychographic analysis of the photorefractive effect in linbo3:fe. *Opt. Express*, 25(25):31640–31650, Dec 2017.

[61] Pierre Thibault, Martin Dierolf, Andreas Menzel, Oliver Bunk, Christian David, and Franz Pfeiffer. High-resolution scanning x-ray diffraction microscopy. *Science*, 321(5887):379–382, 2008.

[62] Pierre Thibault, Martin Dierolf, Oliver Bunk, Andreas Menzel, and Franz Pfeiffer. Probe retrieval in ptychographic coherent diffractive imaging. *Ultramicroscopy*, 109(4):338 – 343, 2009.

[63] Steven W Smith et al. The scientist and engineer's guide to digital signal processing. *California Technical Publishing*, 1997.

[64] Marin van Heel and Michael Schatz. Fourier shell correlation threshold criteria. *Journal of Structural Biology*, 151(3):250 – 262, 2005.

[65] Pawel A. Penczek. Chapter three - resolution measures in molecular electron microscopy. In Grant J. Jensen, editor, *Cryo-EM, Part B: 3-D Reconstruction*, volume 482 of *Methods in Enzymology*, pages 73 – 100. Academic Press, 2010.

[66] Niccolò Banterle, Khanh Huy Bui, Edward A. Lemke, and Martin Beck. Fourier ring correlation as a resolution criterion for super-resolution microscopy. *Journal of Structural Biology*, 183(3):363 – 367, 2013.

[67] J Radon. Über die bestimmung von funktionen durch ihre integralwerte längs gewisser mannigfaltigkeiten. *Verh. Säch. Akad. Wiss. Leipzig*, 295:262–277, 1917.

[68] Y.S. Kwoh, I.S. Reed, and T.-K. Truong. A generalized omega-filter for 3-d reconstruction. *Nuclear Science, IEEE Transactions on*, 24(5):1990–1998, June 1977.

[69] A.H. Andersen and A.C. Kak. Simultaneous algebraic reconstruction technique (sart): A superior implementation of the art algorithm. *Ultrasonic Imaging*, 6(1):81 – 94, 1984.

[70] A.C. Kak, M. Slaney, IEEE Engineering in Medicine, and Biology Society. *Principles of Computerized Tomographic Imaging*, chapter 7.4 SART (Simultaneous Algebraic Reconstruction Technique). IEEE Engineering in Medicine and Biology Society, 1988.

[71] M. Jiang and G. Wang. Convergence of the simultaneous algebraic reconstruction technique (sart). *IEEE Transactions on Image Processing*, 12(8):957–961, Aug 2003.

[72] Richard Gordon, Robert Bender, and Gabor T. Herman. Algebraic Reconstruction Techniques (ART) for three-dimensional electron microscopy and x-ray photography. *Journal of Theoretical Biology*, 29(3):471 – 481, 1970.

[73] A.C. Kak, M. Slaney, IEEE Engineering in Medicine, and Biology Society. *Principles of Computerized Tomographic Imaging*, chapter 7.2 ART (Algebraic Reconstruction Techniques). IEEE Engineering in Medicine and Biology Society, 1988.

[74] A.C. Kak, M. Slaney, IEEE Engineering in Medicine, and Biology Society. *Principles of Computerized Tomographic Imaging*, chapter 7.3 SIRT (Simultaneous Iterative Reconstructive Technique). IEEE Engineering in Medicine and Biology Society, 1988.

[75] S. L. Marple. Computing the discrete-time 'analytic' signal via fft. *Conference Record of the Thirty-First Asilomar Conference on Signals, Systems and Computers (Cat. No.97CB36136)*, 2:1322–1325 vol.2, 1997.

[76] Peter Gilbert. Iterative methods for the three-dimensional reconstruction of an object from projections. *Journal of Theoretical Biology*, 36(1):105 – 117, 1972.

[77] Cristian Badea and Richard Gordon. Experiments with the nonlinear and chaotic behaviour of the multiplicative algebraic reconstruction technique (MART) algorithm for computed tomography. *Physics in Medicine & Biology*, 49(8):1455, 2004.

[78] M. Soleimani and T. Pengpen. Introduction: a brief overview of iterative algorithms in x-ray computed tomography. *Philosophical transactions. Series A, Mathematical, physical, and engineering sciences*, 373(2043):20140399, June 2015.

[79] T. Gerzen and D. Minkwitz. Simultaneous multiplicative column-normalized method (smart) for 3-d ionosphere tomography in comparison to other algebraic methods. *Annales Geophysicae*, 34(1):97–115, 2016.

[80] A. P. Dempster, N. M. Laird, and D. B. Rubin. Maximum likelihood from incomplete data via the em algorithm. *Journal of the Royal Statistical Society: Series B (Methodological)*, 39(1):1–22, 1977.

[81] H. M. Hudson and R. S. Larkin. Accelerated image reconstruction using ordered subsets of projection data. *IEEE Transactions on Medical Imaging*, 13(4):601–609, Dec 1994.

[82] Ji-Ho Chang, J. M. M. Anderson, and J. R. Votaw. Regularized image reconstruction algorithms for positron emission tomography. *IEEE Transactions on Medical Imaging*, 23(9):1165–1175, Sep. 2004.

[83] Betsy A. Dowd, Graham H. Campbell, Robert B. Marr, Vivek V. Nagarkar, Sameer V. Tipnis, Lisa Axe, and D. Peter Siddons. Developments in synchrotron x-ray computed microtomography at the national synchrotron light source, 1999.

[84] Mark L. Rivers. tomorecon: High-speed tomography reconstruction on workstations using multi-threading, 2012.

[85] Anthony Richard Crowther, D. J. DeRosier, and Klug Aaron. The reconstruction of a three-dimensional structure from projections and its application to electron microscopy. *Proceedings of the Royal Society of London. A. Mathematical and Physical Sciences*, 317(1530):319–340, June 1970.

[86] R. Chityala, K. R. Hoffmann, S. Rudin, and D. R. Bednarek. Artifact reduction in truncated ct using sinogram completion. *Proceedings of SPIE–the International Society for Optical Engineering*, 5747(3):2110–2117, February 2005.

[87] M Defrise, f. Noo, R. Clackdoyle, and H. Kudo. Truncated hilbert transform and image reconstruction from limited tomographic data. *Inverse Problems*, 22(3):1037, 2006.

[88] J. C. da Silva, M. Guizar-Sicairos, M. Holler, A. Diaz, J. A. van Bokhoven, O. Bunk, and A. Menzel. Quantitative region-of-interest tomography using variable field of view. *Opt. Express*, 26(13):16752–16768, Jun 2018.

[89] G. Zeng. *Medical Image Reconstruction: A Conceptual Tutorial*, chapter 5.4.3 3D Radon Inversion Formula. Higher Education Press, 2010.

[90] Manuel Guizar-Sicairos, Ana Diaz, Mirko Holler, Miriam S. Lucas, Andreas Menzel, Roger A. Wepf, and Oliver Bunk. Phase tomography from x-ray coherent diffractive imaging projections. *Opt. Express*, 19(22):21345–21357, Oct 2011.

[91] Doğa Gürsoy. Direct coupling of tomography and ptychography. *Opt. Lett.*, 42(16):3169–3172, Aug 2017.

[92] A.C. Kak, M. Slaney, IEEE Engineering in Medicine, and Biology Society. *Principles of Computerized Tomographic Imaging*. IEEE Engineering in Medicine and Biology Society, 1988.

[93] Selin Aslan, Viktor Nikitin, Daniel J. Ching, Tekin Bicer, Sven Leyffer, and Doğa Gürsoy. Joint ptycho-tomography reconstruction through alternating direction method of multipliers. *Opt. Express*, 27(6):9128–9143, Mar 2019.

[94] JM Rodenburg. Ptychography–early history and 3d scattering effects. In *Short-Wavelength Imaging and Spectroscopy*, pages 867809–867809. International Society for Optics and Photonics, 2012.

[95] T. M. Godden, R. Suman, M. J. Humphry, J. M. Rodenburg, and A. M. Maiden. Ptychographic microscope for three-dimensional imaging. *Opt. Express*, 22(10):12513–12523, May 2014.

[96] Albert G. Machoke, Ana M. Beltrán, Alexandra Inayat, Benjamin Winter, Tobias Weissenberger, Nadine Kruse, Robert Güttel, Erdmann Spiecker, and Wilhelm Schwieger. Micro/macroporous system: Mfi-type zeolite crystals with embedded macropores. *Advanced Materials*, 27(6):1066–1070, 2015.

[97] Tobias Weissenberger, Bastian Reiprich, Albert G. F. Machoke, Katharina Klühspies, Jürgen Bauer, Ralf Dotzel, John L. Casci, and Wilhelm Schwieger. Hierarchical mfi type zeolites with intracrystalline macropores: the effect of the macropore size on the deactivation behaviour in the mto reaction. *Catal. Sci. Technol.*, 9:3259–3269, 2019.

[98] Robert Hoppe. *Anpassung und Optimierung des ptychographischen Modells für die quantitative Mikroskopie mit kohärenter Röntgenstrahlung und sichtbarem Laserlicht*. PhD thesis, Universität Hamburg, Von-Melle-Park 3, 20146 Hamburg, 2019.

[99] Doğa Gürsoy, Francesco De Carlo, Xianghui Xiao, and Chris Jacobsen. TomoPy: a framework for the analysis of synchrotron tomographic data. *Journal of Synchrotron Radiation*, 21(5):1188–1193, June 2014.

[100] Tobias Weissenberger, Rainer Leonhardt, Benjamin Apeleo Zubiri, Martina Pitínová-Štekrová, Thomas L. Sheppard, Bastian Reiprich, Jürgen Bauer, Ralf Dotzel, Maik Kahnt, Andreas Schropp, Christian G. Schroer, Jan-Dierk Grunwaldt, John Casci, Jiří Čejka, Erdmann Spiecker, and Wilhelm Schwieger. Synthesis and characterisation of hierarchically structured titanium silicalite-1 zeolites with large intracrystalline macropores. *Chemistry - A European Journal*, 0(ja), 2019.

[101] P Thibault and M Guizar-Sicairos. Maximum-likelihood refinement for coherent diffractive imaging. *New Journal of Physics*, 14(6):063004, 2012.

[102] Thilo Krause, Michael Hanke, Lars Nicolai, Zongzhe Cheng, Michael Niehle, Achim Trampert, Maik Kahnt, Gerald Falkenberg, Christian G. Schroer, Jana Hartmann, Hao Zhou, Hergo-Heinrich Wehmann, and Andreas Waag. Structure and composition of isolated core-shell $(\mathrm{In,Ga})\mathrm{N}/\mathrm{GaN}$ rods based on nanofocus x-ray diffraction and scanning transmission electron microscopy. *Phys. Rev. Applied*, 7:024033, Feb 2017.

[103] Robert Hoppe, Juliane Reinhardt, Georg Hofmann, Jens Patommel, Jan-Dierk Grunwaldt, Christian D. Damsgaard, Gerd Wellenreuther, Gerald Falkenberg, and Christian G. Schroer. High-resolution chemical imaging of gold nanoparticles using hard x-ray ptychography. *Appl. Phys. Lett.*, 102(20):203104, 2013.

[104] Hitachi High-Technologies. Vortex-em x-ray detector, (Accessed September 10, 2019).

[105] Gerald R Lachance and Fernand Claisse. *Quantitative X-ray fluorescence analysis*, volume 7. Wiley, 1995.

[106] Burkhard Beckhoff, Birgit Kanngießer, Norbert Langhoff, Reiner Wedell, and Helmut Wolff. *Handbook of practical X-ray fluorescence analysis*. Springer Science & Business Media, 2007.

[107] V.A. Solé, E. Papillon, M. Cotte, Ph. Walter, and J. Susini. A multiplatform code for the analysis of energy-dispersive x-ray fluorescence spectra. *Spectrochimica Acta Part B: Atomic Spectroscopy*, 62(1):63 – 68, 2007.

[108] J Hsieh, E Chao, J Thibault, B Grekowicz, A Horst, S McOlash, and TJ Myers. A novel reconstruction algorithm to extend the ct scan field-of-view. *Medical physics*, 31(9):2385–2391, 2004.

[109] B.L. Henke, E.M. Gullikson, and J.C. Davis. X-ray interactions: Photoabsorption, scattering, transmission, and reflection at e = 50-30,000 ev, z = 1-92. *Atomic Data and Nuclear Data Tables*, 54(2):181 – 342, 1993.

[110] Benjamin Watts. Calculation of the kramers-kronig transform of x-ray spectra by a piecewise laurent polynomial method. *Opt. Express*, 22(19):23628–23639, Sep 2014.

[111] M. Katsikini, H. Rossner, M. Fieber-Erdmann, E. Holub-Krappe, T. D. Moustakas, and E. C. Paloura. Gallium *K*-edge EXAFS measurements on cubic and hexagonal GaN. *Journal of Synchrotron Radiation*, 6(3):561–563, May 1999.

[112] M. Kahnt, G. Falkenberg, J. Garrevoet, J. Hartmann, T. Krause, M. Niehle, M. Scholz, M. Seyrich, A. Trampert, A. Waag, H.-H. Wehmann, F. Wittwer, H. Zhou, M. Hanke, and C. G. Schroer. Simultaneous hard x-ray ptychographic tomography and x-ray fluorescence tomography of isolated hollow core-shell gan rods. *Microscopy and Microanalysis*, 24(S2):32–33, 2018.

[113] Niklaus Kränzlin, Wouter van Beek, Markus Niederberger, and Dorota Koziej. Mechanistic studies as a tool for the design of copper-based heterostructures. *Adv. Mater. Interfaces*, 2(9):1500094–, June 2015.

[114] F. Sloan Roberts, Kendra P. Kuhl, and Anders Nilsson. High selectivity for ethylene from carbon dioxide reduction over copper nanocube electrocatalysts. *Angewandte Chemie International Edition*, 54(17):5179–5182, 2015.

[115] Anna Loiudice, Peter Lobaccaro, Esmail A. Kamali, Timothy Thao, Brandon H. Huang, Joel W. Ager, and Raffaella Buonsanti. Tailoring copper nanocrystals towards c2 products in electrochemical co2 reduction. *Angewandte Chemie International Edition*, 55(19):5789–5792, 2016.

[116] Markus Niederberger, Michael H. Bartl, and Galen D. Stucky. Benzyl alcohol and titanium tetrachloridea versatile reaction system for the nonaqueous and low-temperature

preparation of crystalline and luminescent titania nanoparticles. *Chemistry of Materials*, 14(10):4364–4370, 2002.

[117] Malwina Staniuk, Ofer Hirsch, Niklaus Kränzlin, Rahel Böhlen, Wouter van Beek, Paula M. Abdala, and Dorota Koziej. Puzzling mechanism behind a simple synthesis of cobalt and cobalt oxide nanoparticles: In situ synchrotron x-ray absorption and diffraction studies. *Chem. Mater.*, 26(6):2086–2094, March 2014.

[118] Christian G. Schroer, Pit Boye, Jan M. Feldkamp, Jens Patommel, Dirk Samberg, Andreas Schropp, Andreas Schwab, Sandra Stephan, Gerald Falkenberg, Gerd Wellenreuther, and Nadja Reimers. Hard x-ray nanoprobe at beamline p06 at petra iii. *Nuclear Instruments and Methods in Physics Research Section A: Accelerators, Spectrometers, Detectors and Associated Equipment*, 616(2):93 – 97, 2010. X-Ray Mirror.

[119] C. G. Schroer, C. Baumbach, R. Döhrmann, S. Klare, R. Hoppe, M. Kahnt, J. Patommel, J. Reinhardt, S. Ritter, D. Samberg, M. Scholz, A. Schropp, F. Seiboth, M. Seyrich, F. Wittwer, and G. Falkenberg. Hard x-ray nanoprobe of beamline P06 at PETRA III. *AIP Conference Proceedings*, 1741(1):030007, 2016.

[120] Akihiro Suzuki, Shin Furutaku, Kei Shimomura, Kazuto Yamauchi, Yoshiki Kohmura, Tetsuya Ishikawa, and Yukio Takahashi. High-resolution multislice x-ray ptychography of extended thick objects. *Phys. Rev. Lett.*, 112:053903, Feb 2014.

[121] Hande Öztürk, Hanfei Yan, Yan He, Mingyuan Ge, Zhihua Dong, Meifeng Lin, Evgeny Nazaretski, Ian K. Robinson, Yong S. Chu, and Xiaojing Huang. Multi-slice ptychography with large numerical aperture multilayer laue lenses. *Optica*, 5(5):601–607, May 2018.

[122] Xiaojing Huang, Hanfei Yan, Yan He, Mingyuan Ge, Hande Öztürk, Yao-Lung L. Fang, Sungsoo Ha, Meifeng Lin, Ming Lu, Evgeny Nazaretski, Ian K. Robinson, and Yong S. Chu. Resolving 500 nm axial separation by multi-slice X-ray ptychography. *Acta Crystallographica Section A*, 75(2):336–341, Mar 2019.

[123] E. Lima, A. Diaz, M. Guizar-Sicairos, S. Gorelick, P. Pernot, T. Schleier, and A. Menzel. Cryo-scanning x-ray diffraction microscopy of frozen-hydrated yeast. *Journal of Microscopy*, 249(1):1–7, 2013.

[124] Peng Li and Andrew Maiden. Multi-slice ptychographic tomography. *Scientific Reports*, 8(1):2049–, 2018.

[125] Esther H. R. Tsai, Federica Marone, and Manuel Guizar-Sicairos. Gridrec-ms: an algorithm for multi-slice tomography. *Opt. Lett.*, 44(9):2181–2184, May 2019.

[126] Kei Shimomura, Makoto Hirose, Takaya Higashino, and Yukio Takahashi. Three-dimensional iterative multislice reconstruction for ptychographic x-ray computed tomography. *Opt. Express*, 26(24):31199–31208, Nov 2018.

[127] M. A. Gilles, Y. S. G. Nashed, M. Du, C. Jacobsen, and S. M. Wild. 3D x-ray imaging of continuous objects beyond the depth of focus limit. *Optica*, 5(9):1078–1086, Sep 2018.

[128] Philipp M. Pelz, Manuel Guizar-Sicairos, Pierre Thibault, Ian Johnson, Mirko Holler, and Andreas Menzel. On-the-fly scans for x-ray ptychography. *Appl. Phys. Lett.*, 105(25):251101, December 2014.

[129] Junjing Deng, Youssef S. G. Nashed, Si Chen, Nicholas W. Phillips, Tom Peterka, Rob Ross, Stefan Vogt, Chris Jacobsen, and David J. Vine. Continuous motion scan ptychography: characterization for increased speed in coherent x-ray imaging. *Opt. Express*, 23(5):5438–5451, Mar 2015.

[130] Xiaojing Huang, Kenneth Lauer, Jesse N. Clark, Weihe Xu, Evgeny Nazaretski, Ross Harder, Ian K. Robinson, and Yong S. Chu. Fly-scan ptychography. *Scientific Reports*, 5:9074, March 2015.

[131] Michal Odstrčil, Mirko Holler, and Manuel Guizar-Sicairos. Arbitrary-path fly-scan ptychography. *Opt. Express*, 26(10):12585–12593, May 2018.

[132] Pantaleo Raimondi. ESRF-EBS: The extremely brilliant source project. *Synchr. Rad. News*, 29(6):8–15, 2016.

[133] H. Tanaka, S. Goto, T. Ishikawa, S. Takano, T. Watanabe, and M. Yabashi. SPring-8 Upgrade Project. In *Proc. of International Particle Accelerator Conference (IPAC'16), Busan, Korea, May 8-13, 2016*, number 7 in International Particle Accelerator Conference, pages 2867–2870, Geneva, Switzerland, June 2016. JACoW. doi:10.18429/JACoW-IPAC2016-WEPOW019.

[134] Pedro F. Tavares, Eshraq Al-Dmour, Åke Andersson, Francis Cullinan, Brian N. Jensen, David Olsson, David K. Olsson, Magnus Sjöström, Hamed Tarawneh, Sara Thorin, and Alexey Vorozhtsov. Commissioning and first-year operational results of the MAX IV 3 GeV ring. *J. Synchrotron Rad.*, 25:1291–1316, 2018.

[135] Christian G. Schroer, Ilya Agapov, Werner Brefeld, Reinhard Brinkmann, Yong-Chul Chae, Hung-Chun Chao, Mikael Eriksson, Joachim Keil, Xavier Nuel Gavaldà, Ralf Röhlsberger, Oliver H. Seeck, Michael Sprung, Markus Tischer, Rainer Wanzenberg, and Edgar Weckert. PETRA IV: The ultra-low emittance source project at DESY. *J. Synchrotron Rad.*, 25(5):1277–1290, 2018. DOI: 10.1107/S1600577518008858.

[136] O.A. Schmidt and et al. Beamline Engineering Overview for the APS Upgrade. In *Proc. 10th Mechanical Engineering Design of Synchrotron Radiation Equipment*

and Instrumentation (MEDSI'18), Paris, France, 25-29 June 2018, number 10 in Mechanical Engineering Design of Synchrotron Radiation Equipment and Instrumentation, pages 324–326, Geneva, Switzerland, Dec 2018. JACoW Publishing. https://doi.org/10.18429/JACoW-MEDSI2018-THOPMA02.

[137] L. Liu, T. Neuenschwander R., and D. Rodrigues A. R. Synchrotron radiation sources in brazil. *Philosophical Transactions of the Royal Society A: Mathematical, Physical and Engineering Sciences*, 377(2147):20180235, June 2019.

[138] M. E. Stuckelberger, T. Nietzold, B. M. West, T. Walker, C. Ossig, M. Kahnt, F. Wittwer, J. Deng, J. M. Maser, B. Lai, Z. Cai, V. Rose, A. Ulvestad, M. V. Holt, S. Hruszkewycz, J. J. Dynes, J. Wang, D. Salomon, R. Tucoulou, X. Huang, H. Yan, E. Nazaretski, Y. S. Chu, C. G. Schroer, and M. I. Bertoni. Challenges and opportunities with highly brilliant x-ray sources for multi-modal in-situ and operando characterization of solar cells. *Microscopy and Microanalysis*, 24(S2):434–435, 2018.

[139] Christina Ossig, Tara Nietzold, Bradley West, Mariana Bertoni, Gerald Falkenberg, Christian G. Schroer, and Michael E. Stuckelberger. X-ray beam induced current measurements for multi-modal x-ray microscopy of solar cells. *JoVE*, 150:e60001, 2019.

List of Publications

ORCID 0000-0003-4332-1202

- **2020** F. Seiboth, D. Brückner, M. Kahnt, M. Lyubomirskiy, F. Wittwer, D. Dzhigaev, T. Ullsperger, S. Nolte, F. Koch, C. David, J. Garrevoet, G. Falkenberg and C. G. Schroer,
'Hard X-ray wavefront correction via refractive phase plates made by additive and subtractive fabrication techniques',
Journal of Synchrotron Radiation, doi: 10.1107/s1600577520007900

- **2020** A. Schropp, R. Döhrmann, S. Botta, D. Brückner, M. Kahnt, M. Lyubomirskiy, C. Ossig, M. Scholz, M. Seyrich, M. E. Stuckelberger, P. Wiljes, F. Wittwer, J. Garrevoet, G. Falkenberg, Y. Fam, T. L. Sheppard, J.-D. Grunwaldt and C. G. Schroer,
'PtyNAMi: ptychographic nano-analytical microscope',
Journal of Applied Crystallography, doi: 10.1107/s1600576720008420

- **2020** X. Yang, M. Kahnt, D. Brückner, A. Schropp, Y. Fam, J. Becher, J.-D. Grunwaldt, T. L. Sheppard and C. G. Schroer,
'Tomographic reconstruction with a generative adversarial network',
Journal of Synchrotron Radiation, doi: 10.1107/S1600577520000831

- **2019** N. Sissouno, F. Boßmann, F. Filbir, M. Iwen, M. Kahnt, R. Saab, C. G. Schroer and W. zu Castell,
'A direct solver for the phase retrieval problem in ptychographic imaging', Mathematics and Computers in Simulation,
doi: 10.1016/j.matcom.2019.11.003

- **2019** M. Kahnt, J. Becher, D. Brückner, Y. Fam, T. Sheppard, T. Weissenberger, F. Wittwer, J.-D. Grunwaldt, W. Schwieger and C. G. Schroer,
'Coupled ptychography and tomography algorithm improves reconstruction of experimental data',
Optica, doi: 10.1364/optica.6.001282

- **2019** J. Becher, T. L. Sheppard, Y. Fam, S. Baier, W. Wang, D. Wang, S. Kulkarni, T. F. Keller, M. Lyubomirskiy, D. Brückner, M. Kahnt, S. Schropp, C. G. Schroer and J.-D. Grunwaldt,
'Mapping the Pore Architecture of Structured Catalyst Monoliths from nm to cm Scale with Electron and X-ray Tomography',
The Journal of Physical Chemistry C, doi: 10.1021/acs.jpcc.9b06541

- **2019** F. Seiboth, M. Kahnt, M. Lyubomirskiy, M. Seyrich, F. Wittwer, T. Ullsperger, S.

Nolte, D. Batey, C. Rau and C. G. Schroer,
'Refractive Hard X-ray Vortex Phase Plates',
Optics Letters, doi: 10.1364/ol.44.004622

- **2019** C. G. Schroer, M. Seyrich, A. Schropp, R. Döhrmann, S. Botta, P. Wiljes, D. Brückner, M. Kahnt, W. Wittwer, L. Grote, D. Koziej, J. Garrevoet and G. Falkenberg,
'Ptychographic Nano-Analytical Microscope (PtyNAMi) at PETRA III: signal-to-background optimization for imaging with high sensitivity',
X-Ray Nanoimaging: Instruments and Methods IV, doi: 10.1117/12.2529096

- **2019** T. Weissenberger, R. Leonhardt, B. Apeleo Zubiri, M. Pitínová-Štekrová, T. L. Sheppard, B. Reiprich, JḂauer, R. Dotzel, M. Kahnt, A. Schropp, C. G. Schroer, J.-D. Grunwaldt, J. Casci, J. Čejka, E. Spiecker and W. Schwieger,
'Synthesis and characterisation of hierarchically structured titanium silicalite-1 zeolites with large intracrystalline macropores',
Chemistry A European Journal, doi: 10.1002/chem.201903287

- **2019** Y. Fam, T. L. Sheppard , J. Becher, D. Scherhaufer, H. Lambach, S. Kulkarni, T. F. Keller, A. Wittstock, F. Wittwer, M. Seyrich, D. Brückner, M. Kahnt, X. Yang, A. Schropp, A. Stierle, C. G. Schroer and J.-D. Grundwaldt,
'A versatile nanoreactor for complementary in situ X-ray and electron microscopy studies in catalysis and materials science',
Journal of Synchrotron Radiation, doi: 10.1107/S160057751900660X

- **2019** M. Lyubomirskiy, F. Koch, K. A. Abrashitova, V. O. Bessonov, N. Kokareva, A. Petrov, F. Seiboth, F. Wittwer, M. Kahnt, M. Seyrich, A. A. Fedyanin, C. David, and C. G. Schroer,
'Ptychographic characterization of polymer compound refractive lenses manufactured by additive technology',
Optics Express, doi: 10.1364/OE.27.008639

- **2018** M. E. Stuckelberger, T. Nietzold, B. M. West, T. Walker, C. Ossig, M. Kahnt, F. Wittwer, J. Deng, J. M. Maser, B. Lai, Z. Cai, V. Rose, A. Ulvestad, M. V. Holt, S. Hruszkewycz, J. J. Dynes, J. Wang, D. Salomon, R. Tucoulou, X. Huang, H. Yan, E. Nazaretski, Y. S. Chu, C. G. Schroer and M. I. Bertoni,
'Challenges and Opportunities with Highly Brilliant X-ray Sources for multi-Modal in-Situ and Operando Characterization of Solar Cells',
Microscopy and Microanalysis, doi: 10.1017/S1431927618014423

- **2018** M. Kahnt, G. Falkenberg, J. Garrevoet, J. Hartmann, T. Krause, M. Niehle, M. Scholz, M. Seyrich, A. Trampert, A. Waag, H.-H. Wehmann, F. Wittwer, H. Zhou, M.

Hanke and C. G. Schroer,
'Simultaneous Hard X-ray Ptychographic Tomography and X-ray Fluorescence Tomography of Isolated Hollow Core-Shell GaN Rods',
Microscopy and Microanalysis, doi: 10.1017/S143192761801259X

- **2018** F. Seiboth, F. Wittwer, M. Scholz, M.Kahnt, M. Seyrich, A. Schropp, W. Wagner, C. Rau, J. Garrevoet, G. Falkenberg and C. G. Schroer,
'Nanofocusing with aberration-corrected rotationally parabolic refractive X-ray lenses',
Journal of Synchrotron Radiation, doi: 10.1107/S1600577517015272

- **2017** T. Krause, M. Hanke, L. Nicolai, Z. Cheng, M. Niehle, A. Trampert, M. Kahnt, G. Falkenberg, C. G. Schroer, J. Hartmann, H. Zhou, H.-H. Wehmann and A. Waag,
'Structure and Composition of Isolated Core-Shell $(\mathrm{In,Ga})\mathrm{N}/\mathrm{GaN}$ *Rods Based on Nanofocus X-Ray Diffraction and Scanning Transmission Electron Microscopy'*,
Physical Review Applied, doi: 10.1103/PhysRevApplied.7.024033

- **2017** C.G. Schroer, M. Seyrich, M. Kahnt, S. Botta, R. Döhrmann, G. Falkenberg, J. Garrevoet, M. Lyubomirskiy, M. Scholz, A. Schropp and F. Wittwer,
'PtyNAMi: Ptychographic nano-analytical x-ray microscope at PETRA III',
SPIE Optical Engineering + Applications, doi: 10.1117/12.2273710

- **2016** F. Seiboth, M. Kahnt, M. Scholz, M. Seyrich, F. Wittwer, J. Garrevoet, G. Falkenberg, A. Schropp and C. G. Schroer,
'Quantitative characterization of aberrations in x-ray optics',
SPIE Optical Engineering + Applications, doi: 10.1117/12.2237646

- **2016** C.G. Schroer, C. Baumbach, R. Döhrmann, S. Klare, R. Hoppe, M. Kahnt, J. Patommel, R. Reinhardt, S. Ritter, D. Samberg, M. Scholz, A. Schropp, F. Seiboth, M. Seyrich, F. Wittwer and G. Falkenberg,
'Hard x-ray nanoprobe of beamline P06 at PETRA III',
AIP Conference Proceedings, doi: 10.1063/1.4952830

Acknowledgement

I could not have accomplish the presented work without the actions of others. This section is to express my gratitude to all those who have been with me for the last four years and contributed to the completion of this work directly or indirectly by motivation, patience, helpfulness, distraction or by offering a new perspective.

First, and foremost, I want to thank my supervisor Christian G. Schroer for allowing me to choose and outline the topic of this work myself, for his expertise, for his support and supervision despite his permanently busy schedule. Second, I would like to show my greatest appreciation to Andreas Schropp for acting as second supervisor and offering his insight, vital support and motivation whenever needed. I would like to offer my special thanks to Michael Hanke for accepting to act as examiner for this work, but also for educational discussions during beamtimes. I am indebt to my other examiners for accepting to assess this work at such a short notice.

Close cooperation within the working group helped immensely with writing the present work. Special thanks to Maria, Juliane, Martin and Felix who shared the ups and down of writing a PhD thesis, spending night shifts at the beamline, despair while coding at the office or checking the menu at the CFEL canteen but also having a life far away from the DESY campus. Special thanks to Felix, as he not only shared the office with me, but also the apartment, allowing for a lively discussion on any topic in the kitchen as well as the office. I would like to also thank Saba, Christina and Dennis for brightening numerous rainy days in the office. I have greatly benefited from Mikhail, Johannes, Micheal and Xiaogang and their experience.

I received generous support from the engineering team: Ralph, Stephan and Patrick. I am particularly grateful for the assistance given by the P06 beamline team, Kathryn, Jan and Gerald before, during and after beamtimes. I want to thank everyone that shared a shift at a beamline with me. Such experiments can not be performed alone and I have learned so much in those discussion at the experiment.

Special thanks to Stefanie for unconditional friendship over so many years and allowing me to use her apartment for the final moments of this PhD project. I am grateful to my parents who have always believed in me and put up with me being stressed, busy and sometimes not very talkative.

Last but not least, I want to thank all of those that I have forgot to mention above.

Thank you.

Declaration on oath

Hiermit erkläre ich an Eides statt, dass ich die vorliegende Dissertationsschrift selbst verfasst und keine anderen als die angegebenen Quellen und Hilfsmittel benutzt habe.

I hereby declare, on oath, that I have written the present dissertation by my own and have not used other than the acknowledged resources and aids.

Maik Kahnt
Hamburg, September 12, 2019